Copyright

by

Wen Pan

2022

The Dissertation Committee for Wen Pan Certifies that this is the approved version of the following dissertation:

Reservoir Description via Statistical and Machine-Learning Approaches

Committee:

Carlos Torres-Verdín, Supervisor

Ian J. Duncan, Co-Supervisor

Michael J. Pyrcz, Co-Supervisor

Zoya Heidari

Larry W. Lake

Reservoir Description via Statistical and Machine-Learning Approaches

by

Wen Pan

Dissertation

Presented to the Faculty of the Graduate School of

The University of Texas at Austin

in Partial Fulfillment

of the Requirements

for the Degree of

Doctor of Philosophy

The University of Texas at Austin

August 2022

Dedication

To my family.

Acknowledgements

I would like to thank all people who supported me during the completion of this dissertation. I am extremely grateful that I could have this opportunity to work with my advisor, Dr. Carlos Torres-Verdín, and co-advisors, Dr. Ian Duncan and Dr. Michael Pyrcz. Throughout my Ph.D. study, they had been consistently giving me enormous guidance and support that I would never have expected. Not only did I deepen my understanding of formation evaluation, geology, spatial statistics, and machine learning but also become familiar with procedures for identifying research problems and conducting research to solve the problems. I am thankful for the life lessons I learned from them, which I believe would help me to further improve myself in my future work and life. I would also like to acknowledge all members of my dissertation committee, Dr. Larry Lake and Dr. Zoya Heidari, for helping review my work, and providing inspiring suggestions and comments.

I would like to acknowledge Rey Casanova, Amy Stewart, and Jin Lee for their administrative support. I am also grateful for the technical support I got from my computer specialists, Roger Terzian, Joaquín Ambía-Garrido, Bruce Klappauf, and John Cassibry.

I was happy that I could have the opportunity to work in three different groups and know about many great people. I would like to thank all my colleagues: Honggeun Jo, Javier Santos, Elnara Rustamzade, Tianqi Deng, Mahmood Shakiba, Mohamad Abdo, Haofeng Song, Lei Liu, Qianjun Liu, Frank Male, Bo Ren, Robin Dommisse, Pierre Aerens, Mohammad Albusairi, Mohamed Bennis, Lizhuo Li, Domenico Crisafulli, Cristian Dominguez, Ali Eghbali, Gabriel Gallardo Giozza, David Gonzalez, Jingxuan Liu, Wendi Liu, Tarek Mohamed, Daria Olszowska, Oriyomi Raheem, Misael Morales, Colin Schroeder, You Wang, Ivan Amaro, Midé Mabadeje, Camilo Gelvez, Julian Salazar, Zhonghao Sun, Jose Hernandez, Wilberth, Ayaz, David Medellin, Kyubo, Aymeric, Naif, Joshua, Juan Diego, Eduardo Maldonado, Hyungjoo, Mathilde, Elsa, Adam, Mauro, Vivek, Valeriia, Yanxiang Yu and many others. I also want to thank all my friends for their companion and support.

I would like to thank British Petroleum (BP) for the summer internship opportunities in 2020 and 2021. Special thanks to Obiajulu Isebor, for his mentorship during my internships. I am also grateful for the help I got from Anar Yusifov, Evgenia Polyakova, Kevin Wolf, Jingfeng Zhang, John Nawab, Jing Zhang, Johnston Rodney, Roy Atish, Sarita, Hayden, Glen Gettemy, Ganyuan Xia, Carole Decalf, Robert King, Patrick Connor, Matthew McQueen, Davies Brian, Nirjhor, Ning Yang, Grace Chan, Youssef Elkady. I would also like to thank Shell, Exxon Mobil, Chevron, Schlumberger, ComboCurves, Sinopec, CNPC, and QRI for offering me internship or full-time employment opportunities.

Finally, I would like to thank my parents and family for their unconditional love and support.

The work reported in this dissertation was funded by the University of Texas at Austin's Research Consortium on Formation Evaluation, Digital Reservoir Characterization Technology and Bureau of Economic Geology, jointly sponsored by Aramco, Baker Hughes, BHP Billiton, Exxon Mobil, BP, Shell, ComboCurves, Chevron, CNOOC International, ConocoPhillips, ENI, Equinor ASA, Halliburton, Inpex, Lundin-Norway, Occidental, Oil Search Alaska, Petrobras, Repsol, Schlumberger, Todd Energy, TotalEnergies and Wintershall-DEA.

Reservoir Description via Statistical and Machine-Learning Approaches

Wen Pan, Ph.D.

The University of Texas at Austin, 2022

Supervisor: Carlos Torres-Verdín

Co-Supervisors: Ian J. Duncan and Michael J. Pyrcz

Description of subsurface reservoirs is important for decision-making in the development of hydrocarbon resources. Reservoir description concerns (1) *geophysical interpretation*: prediction of rock properties from geophysical measurements such as borehole and seismic amplitude data, and (2) *reservoir modeling*: modeling of the spatial distribution of rock properties conditioned by geophysical interpretations (*geological modeling*), and simulation of fluid-transport, elastic, mechanical, and electromagnetic phenomena, among others, taking place in a geological model (*reservoir simulation*). Reservoir description based on stochastic reservoir modeling and conditioned by fluid production history enables uncertainty estimation for hydrocarbon reserves and fluid production forecast. Accurate reservoir description assists the management of risk and profit during the exploration and development of hydrocarbon production resources.

As one of the most important components of reservoir description, the interpretation of well logs provides high-resolution estimations of *in situ* rock properties around the wellbore, such as lithology, porosity, fluid saturation, permeability, and elastic moduli. However, conventional petrophysical models are often too simplistic to reproduce the complex relationship between well logs and rock properties, especially permeability. Therefore, data-driven inferential methods, such as machine learning modeling, are needed for more accurate permeability prediction in spatially complex rocks. The accurate

prediction of permeability across multiple wells is even more challenging because of variable borehole environmental conditions (e.g., drilling fluid and borehole size), different logging instruments (e.g., induction vs. lateral resistivity logs), and their vintage (e.g., logging-while-drilling vs. wireline logs). To mitigate biases introduced by both variable borehole environmental conditions and borehole instruments, well-log normalization is commonly implemented prior to performing multi-well interpretation projects. However, conventional well-log normalization methods ignore the correlation among different well logs and require much effort and expertise by the interpreter.

The first objective of this dissertation is to develop a data-driven interpretation workflow that uses machine-learning methods to perform automatic well-log normalization by considering the correlation among different well logs and to accurately estimate permeability from the normalized well logs. The workflow consists of four steps: (1) identifying well-calibrated wells (*type wells*) for the wells that need correction (*test wells*), based on the statistical distance of the associated well logs. (2) Obtaining training data from type wells to train the machine-learning model to minimize the mean-squared error (MSE) of permeability prediction. (3) Performing well-log normalization for the test well logs by minimizing the divergence to the type-well well logs. (4) Predicting the permeability of test wells using normalized well logs.

The new interpretation workflow is applied to predict the permeability of 30 wells in the Seminole San Andres Unit (SSAU). Compared to the permeability prediction model without well-log normalization, the new workflow decreases the mean-squared error (MSE) of permeability prediction by 20-50% and greatly accelerates well-log preprocessing with the automatic well-log normalization step.

Stochastic reservoir models conditioned by petrophysical and geophysical interpretations are important for uncertainty management during reservoir exploration and development. Conventional geostatistical methods, such as Kriging and multiple-point simulation, are commonly used for conditional reservoir modeling. However, it is difficult to use these methods to construct reservoir models that reproduce long-range geological patterns that are important for fluid-transport prediction, such as the continuity of channels in a turbidite channel sedimentary system.

The second objective of this dissertation is to develop a new machine learning method to construct stochastic reservoir models that reproduce important long-range patterns and are conditioned by the interpretation of well logs and seismic amplitude data. This method consists of three steps: (1) calculating training images of a depositional system, such as a turbidite channel or a deepwater lobe system, with rule-based modeling methods. (2) Training a new conditional generative adversarial model, referred to as the stochastic pix2pix model, to generate reservoir model realizations that reproduce patterns in the training images and are conditioned by well logs and seismic amplitude data. (3) Using the trained model to generate conditional reservoir model realizations. However, limitations on computer memory make it difficult for the new method to generate reservoir model realizations with over millions of voxels, such as models with multi-scale architectural elements. To further improve the computational efficiency to generate large and detailed reservoir models, a hierarchical modeling workflow is developed which uses the stochastic pix2pix model to simulate architectural elements from the largest to the smallest scale.

The stochastic pix2pix method is verified by comparing the generated lobe and fluvial channel model realizations to reservoir models constructed with the rule-based modeling method. Comparisons indicate that conditioning data, such as rock facies interpreted from well logs and depositional surfaces identified from seismic amplitude data, are well reproduced in model realizations generated with the new method. Statistical metrics, such as semi-variogram, multiple-point histogram (MPH), compensational stacking index, geometrical probability map, and rock facies histogram were calculated to confirm that model realizations accurately reproduce the patterns observed in the training images. Metrics of performance indicate a good reproduction of patterns, for example, the mean-absolute error of geometrical probability is below 2%, while the MPH difference is below 5%.

The combination of well-log normalization and interpretation workflow with machine learning-based stochastic reservoir modeling enables more accurate formation evaluation and better estimates of uncertainties associated with rock property distributions than possible with standard modeling approaches.

Table of Contents

List of Tables

List of Figures

Chapter 1: Introduction

Reservoir description involves the interpretation of geophysical data and the construction of numerical models for a hydrocarbon reservoir. Interpretation of geophysical data, such as well logs and seismic amplitude, provides 1) high-resolution rock property estimation at well locations and low-resolution rock property prediction around the reservoir, and 2) information about the geological setting, depositional patterns, and geometries of depositional elements. To integrate the interpretation results at different scales, geostatistical methods are applied to interpolate rock properties between wells and build subsurface uncertainty models that honor the field data and reproduce the depositional patterns informed by the interpretation of geophysical data. An accurate description of subsurface reservoirs and quantification of the associated uncertainties are important for the estimation of reserves and hydrocarbon production forecast, which assist risk management and decision making regarding the development of an oil field. To improve the accuracy of well-log interpretation, I developed a new machine learning (ML) workflow for multi-well well-log normalization and permeability prediction, and to improve the modeling for subsurface uncertainty, I proposed a new machine learning workflow for single- and multi-scale stochastic reservoir modeling.

To improve the accuracy of permeability prediction, a new machine learning model for well-log normalization and permeability prediction workflow is developed. The machine learning model is trained with data from *type wells*, which are wells with well-calibrated well logs. The model is then used to normalize the well logs and predict the permeability of *test wells*, which are wells with well logs that need correction. Type wells are identified with a new divergence-based distance matrix. The new type well identification method and permeability prediction model improve the reliability of petrophysical interpretation by imposing a stationarity constraint, which assumes that the formation property distribution among a test well and associated type wells is stationary, i.e., statistics of formation property distribution do not vary spatially.

Conventional geostatistical methods for stochastic reservoir modeling generally do not reproduce long-range depositional patterns. The sequential simulation strategy adopted in conventional geostatistical methods makes it slow to calculate multiple, detailed reservoir model realizations. To mitigate these problems, a new method, the stochastic pix2pix model, is developed for reservoir modeling. It is trained using training images calculated with a rule-based reservoir modeling method and applied to generate multiple reservoir model realizations that honor seismic and petrophysical interpretations and reproduce depositional patterns.

The first section of this chapter gives a review of the background and relevant literature on permeability prediction, well-log normalization, and reservoir modeling. The next three sections discuss the limitations of current methods, the objectives of my research, and provide an overview of the new methods. The last section provides an outline of the subsequent chapters, related journal publications, and conference proceedings.

1.1 Background and Literature Review

The first part of this section reviews the definition and common methods for permeability prediction and different types of well-log correction methods; the second part of this section reviews the definition of reservoir modeling and common geostatistical methods for reservoir modeling.

1.1.1 Permeability Prediction and Well-Log Correction

Accurate permeability prediction is important for the evaluation of the flow potential of a reservoir. Permeability prediction is about using direct or indirect measurements of formation properties to predict permeability. Many models have been proposed to predict permeability from different measurements, such as well logs, porosity, grain size, and pore size. Some petrophysical models are based on an ideal physical model, such as the tube bundle model (Carman, 1956); others are based on an empirical correlation between different features. Krumbein and Monk (1943), Berg (1970), and Van Baaren (1979) propose to use grain size to predict permeability; Swanson (1981) and Pittman (1992) predict permeability from capillary pressure curve measurements; Nicolaysen and Svendsen (1991) use lookup table to directly predict permeability from well logs. In this dissertation, I mainly focus on developing new methods of using well logs to predict permeability. The simplicity of empirical petrophysical models makes it unlikely to overfit the data, thus making the models suitable for permeability prediction in homogeneous reservoirs. However, for complex reservoirs with many facies and different degrees of diagenesis, simple petrophysical models may underfit the data and not capture the complex relationship between permeability and well logs. *Overfitting* is the situation where the model's performance in the training set is better than that in the test set, and *underfitting* happens when the model is too simple to accurately predict permeability even for the training set.

To capture the complex relationship between permeability and well logs, researchers resort to data-driven methods. For example, to make permeability predictions, Finol and Jing (2002) use the fuzzy modeling method, Mohaghegh et al. (1995) use an artificial neural network (ANN), and Otchere et al. (2021) use ensemble modeling methods, such as the random forest (RF) method. These models can accurately predict permeability for the training set (type wells).

However, an accurate permeability prediction model for type wells does not guarantee an accurate permeability prediction for test wells, because logging conditions, such as logging tools, logging vintage, and borehole environment of each well may vary, resulting in different degrees of bias in well logs. Therefore, well-log correction methods based on physical models and statistical models are proposed, respectively.

To perform the correction based on physical models, interpreters use a physical model to simulate potential measurement bias introduced by different environmental conditions. For example, borehole correction removes the signal from the borehole to obtain the signal solely from the formation by simulating the formation of mud cake and intrusion of mud filtrate (Grove and Minerbo, 1991; Doetsch et al., 2010). Despite the physical basis of these methods, a lack of information about logging parameters, such as mud weight, mud composition, drilling speed, logging tools, etc., and the complexity of the logging environment may cause an inaccurate physical model-based correction.

A more straightforward way of performing well-log correction is to use statistical methods to perform well-log normalization. Statistical methods do not require information or make assumptions about the logging tools and borehole conditions. They are only based on the assumption of the *stationarity* of formation properties between wells. Well-log normalization assumes a test well and associated type wells have similar formation properties, which should yield similar well logs if they are measured under the same environmental conditions (Bornemann and Doveton, 1981; Sheir, 2004; Pan et al., 2022). The dissimilarity between distributions of well logs of each well can be quantified as the *divergence*, which is defined as the statistical distance between two probability distributions (Kullback and Leibler, 1951; Fuglede and Topsoe, 2004). In conventional well-log normalization methods, well logs from a test well are linearly scaled to match the histograms of well logs from associated type wells. For example, the two-point scaling normalization matches the minimum and maximum values of well logs that correspond to rocks with distinct petrophysical properties (Sheir, 2004).

1.1.2 Stochastic Reservoir Modeling

Stochastic reservoir modeling is important for understanding the propagation of uncertainties from the static data, such as understanding of geological setting, well, and seismic data, to dynamic data, such as production and pressure data. Pyrcz and Deutsch (2014) define reservoir modeling as the calculation of a numerical representation of the subsurface over the volume of interest, and the properties of interest. Reservoir models should integrate all information available in the field, e.g., interpretations of wireline logs, seismic data, and production data. The uncertainty of a reservoir is represented by calculating multiple reservoir model realizations and scenarios, and the model realizations can be used for risk management during decision-making.

Many geostatistical methods have been developed to perform stochastic reservoir modeling. They are based on different assumptions and are used to reproduce different spatial statistics. Sequential Gaussian simulation (SGS), which is one of the earliest reservoir modeling methods, is still very popular in the industry for modeling homogenous reservoirs. The SGS method is used to simulate a Gaussian field, where the simulated data is assumed to be autocorrelated, Gaussian random variables. When it is used for formation property modeling, the property to be simulated is transformed to be Gaussian distributed with the quantile transformation method, and then the simulation domain is filled with property prediction along a random raster path. The value assigned to each cell in a reservoir model is calculated as the weighted sum of nearby simulated data, well data, and random residuals (Pyrcz and Deutsch, 2014). The weights of different data and the variance of residuals are calculated with the Kriging method (Oliver and Webster, 1990). The SGS model realizations only reproduce two-point statistics, i.e., the semi-variogram (autocorrelation) of the formation property. Despite the simplicity of this method, i.e., the SGS method only requires well data for geostatistics (semi-variogram) calculation, it is difficult for the SGS method to generate reservoir model realizations with complex patterns.

To mitigate this problem, the multiple-point simulation (MPS) method is introduced. The MPS method extracts patterns, i.e., the multiple-point statistics, from training images (TI) using a filter, which is denoted as the *template*. The pattern extracted with the template is denoted as the *event*, the statistics of which are used to guide the stochastic, sequential simulation of a reservoir model. The statistics of events can be stored and searched in different ways during the sequential simulation. For example, Strebelle (2002) proposes to use the dynamic data storage search tree to store and retrieve patterns; Mariethoz (2010) proposes to use the direct sampling method to avoid storage of the event, and search for a matched event in a random portion of the TI for every step of the sequential simulation. Despite the improvement in pattern reproduction of the MPS method, a large template is needed to reproduce large-scale patterns, which requires large computer memory and storage. Moreover, sequential simulation with a large template also makes it slow to perform the simulation, because of a large number of conditional data within a template and a complex search tree. To improve the computational efficiency, the method based on the simulation of patches is developed, where a small patch instead of a node is simulated for every step of the sequential simulation (Hu and Chugunova, 2008; Pyrcz and Deutsch, 2014; Li et al., 2016). However, the lack of continuity near the boundary of adjacent, simulated patches is still an unsolved problem.

To enable more efficient reservoir modeling and reproduction of large-scale patterns, researchers resort to machine learning methods. Generative adversarial neural network (GAN), variational autoencoder, and associated variants are recently used for unconditional (not conditioned to field data), stochastic reservoir modeling (Goodfellow et al., 2014; Chan and Elsheikh, 2017; Laloy et al., 2018). Compared to the MPS method, which stores and retrieves pattern information with a search tree, machine learning models enable large-scale pattern detection, learning, and retrieval via stacked convolutional neural networks that do not require that much computer memory and storage space. Instead of sequentially simulating each node like the MPS method, which may take about an hour for a large simulation grid (>1000000 cells) and large template size (>800 cells), the machine learning model simulates the whole simulation grid at once within a few seconds. The fast simulation is achieved by mapping the spatial statistics of training images to a simple Gaussian distribution via variational inference. During the training of a GAN model, we minimize the divergence between statistics of training images and those of generated reservoir model realizations. In a GAN model, two neural networks denoted as the generator and the discriminator, are trained adversely to generate reservoir models that reproduce the spatial statistics of the training image. The generator is trained to generate reservoir models that reproduce patterns in the training image. The discriminator is trained to distinguish the training images from reservoir model realizations generated by the generator. When the generator is successfully trained, the discriminator cannot tell if generated reservoir model realizations are from the training image or not. Jason-Shannon (JS) divergence between training image patches and generated reservoir models is a metric to identify the training process. Once the JS divergence is minimized, the Nash equilibrium is reached (Goodfellow et al., 2014), and the discriminator cannot tell the generated reservoir models from the training image patches, and the generated reservoir model realizations are believed to successfully reproduce patterns in the training image.

1.2 Problem Statement

Good reservoir models should honor accurate well-log interpretation. Biases in well-log measurements and interpretation tend to propagate to reservoir models and deteriorate efficient reservoir development; Reservoir models that do not reproduce well interpretation results may yield unreliable estimation for the productivity of a reservoir. Despite many successful applications of previous methods for well-log correction, permeability prediction accuracy imaprovement, and conditional stochastic reservoir modeling (Aly et al., 1997, Aguirre and Antelo, 2001; Hassanpour et al., 2013; Quartero et al., 2014; Al-Mudhafar, 2017; Wood, 2020), challenges remain for more accurate formation evaluation under different logging environments and modeling of a complex reservoir. Three problems with the well-log normalization and permeability prediction, and two challenges in reservoir modeling are discussed as follows:

1) For permeability prediction, most machine learning models assume independent samples and stationary and independent well-log noise. For example, when the mean squared error (MSE) is used as the loss function to train a model, the measurement noise covariance is assumed to be a constant, and the autocovariance of adjacent data noise is assumed to be zero. However, the well-log bias introduced by different logging environments invalidates this assumption. For example, we may constantly overestimate or underestimate the permeability for a whole interval in some wells, which is a common issue observed when previous methods are applied to predict permeability. The nonstationary well-log measurement bias leads to the nonstationary permeability prediction error. Therefore, the loss function of

the permeability prediction model needs to be modified, and well-log correction is needed to include additional constraints to mitigate the effect of the nonstationary bias on permeability prediction.

2) For well-log normalization, conventional methods only consider the univariate statistics of each well log. However, the correlation between different types of well logs, which is important for constraining the normalization of a well log, is largely ignored or requires the subjective knowledge of an expert. An automatic normalization method considering the statistics of and between well logs is needed.
3) For type well identification in well-log normalization, the nearest wells do not necessarily have similar formation property distribution, especially in the conditions that the reservoir is complex and nonstationary, formation property lacks spatial continuity, and the well spacing is large. A method to directly calculate the statistical similarity between a test well and a type well is needed.
4) For reservoir modeling conditioning, the GAN method tends to have mode collapse issues, i.e., the lack of diversity in the reservoir model realizations it generates. To improve the conditioning to both well and seismic data interpretation while generating diverse model realizations, a more robust generative machine learning model is needed.
5) For large, high-resolution reservoir modeling, direct simulation with the GAN model may require too much memory and storage resource. A hierarchical modeling approach should be integrated with the GAN method for more efficient modeling.

1.3 Research Objectives

To address the limitations in conventional permeability estimation, well-log normalization, type well identification, and reservoir modeling methods, I develop new statistical and machine learning models. The scope of this dissertation includes:

1) Developing a permeability prediction model that is robust to different logging environments.
2) Developing a new, automatic, well-log normalization method that considers the joint distribution of each well log.
3) Developing a type-well identification method to properly identify type (training) wells for a test well in a complex reservoir with large well spacing.
4) Developing a new reservoir modeling method that improves reservoir modeling efficiency and generates reservoir model realizations that reproduce long-range patterns while honoring well, and seismic data.
5) Developing a workflow that efficiently calculates high-resolution, large reservoir model realizations for reservoirs with many depositional hierarchies.

1.4 Method Overview

The interpretation of well logs and the calculation of reservoir models involves the manipulation of "big data", i.e., large, high-dimensional data, which is difficult to handle with simple empirical or physical models. To improve our capability of handling "big data", many data-driven methods that rely on advanced statistics are proposed. Data-driven methods are applied to the interpretation of well logs and reservoir modeling with success (Deng et al., 2019; Wood et al., 2020; Zhang et al., 2022). However, few petrophysical and geostatistical insights are incorporated in these methods; the statistical and physical assumptions of the methods are still vague and not discussed. Therefore, I extend current machine-learning methods to incorporate geostatistics and petrophysics constraints. The assumptions and application of the new data-drive methods and the conventional machine learning methods are discussed and compared. The new data-driven methods I developed to reach the objectives and mitigate the problems in well-log normalization, permeability prediction, and reservoir modeling are as follows:

1) Conventional well-log interpretation methods do not consider the error introduced by logging conditions that vary with wells. To mitigate the effects of different logging environments for permeability prediction, I developd a new deep neural network model, the discriminative adversarial (DA) neural network. Compared to classical neural network models (Mohaghegh et al., 1995; Aminian et al., 2003), which only minimize the mean squared error of permeability prediction in the training data, this new model has an additional constraint term, which is based on the assumption of stationary formation property among test and training wells. Therefore, the new model is trained to minimize both the error of permeability prediction in the training data and the divergence between training and test data.
2) The classical well-log normalization methods for well-log correction ignore the relationships between different types of well logs, making the correction results unreliable. To improve the reliability of well log correction, I developd an automatic well-log normalization method that considers the multivariate statistics of different types of well logs. The well-log normalization model is embedded in the permeability prediction model so that the statistics of predicted permeability are also considered when performing the normalization.
3) Conventional type-well identification methods assume the same logging conditions for all wells and stationary rock property distribution. However, these assumptions are rarely valid. To identify type wells in a complex reservoir and with different

logging conditions, I develop a type-well identification method based on the divergence between well logs of each well.

4) It is difficult for conventional geostatistical methods to reproduce long-range depositional patterns while honoring the seismic and well data. Therefore, I developed a new deep learning model, the stochastic pix2pix model, that fills in high-resolution heterogeneity models consistent with low-resolution seismic regions, geologic architecture, and well data with reasonable realizations to represent uncertainty ready for flow forecasting. In addition, I have extended minimum acceptance reservoir model checks to QC these models for reliable forecasting.
5) Multi-scale reservoir modeling is difficult because it is computationally expensive and the relationships between architectural elements at different scales are difficult to model. To perform efficient multi-scale reservoir modeling, I propose a workflow that first calculates large-scale depositional elements, and then populates small depositional elements within large containers. The workflow is based on sequential application of a GAN-based, stochastic depositional-element modeling method and density-based spatial clustering of applications with noise (DBSCAN)-based depositional-element identification.

1.5 Dissertation Outline

This dissertation is divided into five chapters. Following this introductory chapter, the next three chapters discuss the research objectives, new methods, and associated results in more detail, and the last chapter summarizes the findings and conclusions.

Chapter 2 introduces new data-driven methods for type-well identification, well-log normalization, and permeability prediction. The assumptions, development, and application of these methods are discussed and compared to conventional methods. This chapter provides the details of the three new methods, which are 1) type well identification with the new, divergence-based method, 2) the well-log normalization with the DA model and linear constraint model, 3) permeability prediction with the DA model and linear constraint models. The new methods are validated with core measurements and well logs from the Seminole San Andres Unit (SSAU), a carbonate reservoir located in the Central Basin. The new methods are compared to conventional methods based on the MSE of permeability prediction.

Chapter 3 describes the structure of the stochastic pix2pix model and its application. The stochastic pix2pix model is an extension of the GAN method (Goodfellow et al., 2014) to perform stochastic reservoir modeling that is conditioned to well and seismic interpretation results. To validate the new method, I calculate fluvial channel models as training images with the rule-based method and use the new method to generate reservoir model realizations based on the training images. Different statistics, such as variogram and multiple point histogram (MPH), of the training images and reservoir model realizations are compared to validate the reproduction of patterns. The conditioning to well and seismic interpretation is also discussed.

In chapter 4, I develop a new workflow by combining the stochastic pix2pix method with the DBSCAN-based depositional element identification method to perform multi-scale reservoir modeling. To validate the workflow, I first calculate conceptual models for the deepwater lobate system with the rule-based method and then use them as training models to train the new workflow to generate multi-scale reservoir model realizations that reproduce patterns in the training images. To assure the reproduction of patterns in the reservoir model realizations, the realizations are compared to the training models based on statistics related to the depositional pattern, geometry of depositional elements, and the conformance of depositional elements across different scales.

In chapter 5, I summarize the finding and conclusions from Chapters 2-4 and provides recommendations for best practice related to this dissertation.

1.6 List of Publications

Based on the research in this dissertation, several journal and conference papers are published or submitted for peer review. They are listed as follows:

1.6.1 Refereed Journal Publications

Pan, W., Torres-Verdín, C., and Pyrcz, M. J. (2021). Stochastic Pix2pix: a new machine learning method for geophysical and well conditioning of rule-based channel reservoir models. Natural Resources Research, 30(2), 1319-1345.

Pan, W., Jo, H., Santos, J. E., Torres-Verdín, C., and Pyrcz, M. J. (2022). Hierarchical machine learning workflow for conditional and multiscale deepwater reservoir modeling. AAPG Bulletin (*accepted*).

Pan, W., Torres-Verdín, C., Duncan I. J., and Pyrcz, M. J. (2021). Reducing the uncertainty of multi-well petrophysical interpretation from well logs via machine-learning and statistical models. Geophysics (*Manuscript submitted for review*).

1.6.2 Refereed Conference Proceedings

Pan, W., Torres-Verdín, C., and Pyrcz, M. J. (2020). New machine learning method for integrated subsurface modeling. Presented at the AGU 2020 Fall Meeting, December 7-16, 2020.

Pan, W., Jo, H., Santos, J. E., Torres-Verdín, C., and Pyrcz, M. J. (2021). Stochastic Pix2Pix method for conditional and hierarchical deepwater reservoir modeling. Presented at the Geostats 2021 Meeting, July 12-16, 2021.

Pan, W., Torres-Verdín, C., and Pyrcz, M. J. (2021). Feature engineering in well log interpretation. Presented at the GeoGulf 2021 Meeting, October 27-29, 2021.

Pan, W., Torres-Verdín, C., and Pyrcz, M. J. (2022). Reducing the uncertainty of multi-well petrophysical interpretation from well logs via machine-learning and statistical models. Presented at the SPWLA 2022 Spring Topical Conference on Petrophysical Machine Learning, March 23-24, 2022.

Chapter 2: Well-Log Normalization and Permeability Prediction via New Machine Learning and Statistical Models

Well-log interpretation provides *in situ* prediction of formation properties such as porosity, hydrocarbon pore volume, water saturation and permeability that support reserve-volume estimates, production forecasts, and decision making in reservoir development. However, due to measurement errors, variability of well logs caused by multiple measurement vendors, different borehole tools, and non-uniform drilling/borehole conditions, predictions of formation properties with original well logs without preprocessing may not be accurate, especially in the context of multi-well prediction. To improve the robustness of multi-well petrophysical property prediction, well-log normalization techniques such as two-point scaling and mean-variance normalization are commonly used to correct well logs. However, these techniques often do not consider the correlation between well logs and require subjective knowledge to be effectively implemented. To reduce the uncertainties and time associated with multi-well petrophysical property prediction, I develop the discriminative adversarial (DA) model and the linear constraint model for well-log normalization and petrophysical property prediction. I also develop a new divergence-based type well identification method for improved test well and training well assignment.

The DA neural network model developed for well-log normalization and interpretation can perform both linear and nonlinear well-log normalization by considering the joint distribution of each well log and formation properties. The linear constraint model uses an ensemble of predictions from linear models to constrain both well-log normalization and petrophysical property prediction. The divergence-based type well identification method is developed to select type (training) wells for a test well based on the statistical similarity of associated well-log distributions instead of the distance between wells.

I apply the proposed methods to improve the accuracy of well-log normalization and the prediction of permeability for the Seminole San Andres Unit, a carbonate reservoir. In comparison to the classical machine-learning model without normalization, the model with two-point scaling normalization, and the model with linear constraints, the DA model yields better performance, e.g., the mean-squared error of permeability prediction decreases by approximately 20-50%.

2.1 Introduction

Petrophysical property prediction is important for accurate reservoir characterization, reservoir modeling calibration, and decision-making during the development of reservoirs (Xu et al., 1992; Pan et al.,2021; Santos et al., 2021; Jo et al., 2020; Jo et al., 2021). Improving the accuracy of petrophysical interpretation of complex reservoirs, such as carbonate and shale reservoirs, is a major challenge in the oil and gas industry (Greder et al., 1996; Mohaghegh et al., 1997; Deng et al., 2020). The complexity of pore geometries, the role of micro fractures, and extensive modification of pore systems by diagenesis (Figure 2.1) confound the relationships and weaken correlations between well logs and petrophysical properties, and make it challenging to predict flow-related petrophysical properties, such as permeability.

The uncertainty of permeability prediction with well logs is mainly caused by two factors: a lack of pore throat structure information in all kinds of well logs except for the nuclear magnetic resonance (NMR) log, and the measurement error (uncertainty) of well logs (Medellin et al., 2019; Wang et al., 2019; Jachmann, 2020).

To better explore related information conveyed by each type of well log, researchers develop complex permeability prediction models, such as machine learning models (Gashler, 2008; Bestagini et al., 2017; Sidahmed et al., 2017; Shashank and Mahapatra, 2018; Bennis and Torres-Verdín, 2019; Brazell et al., 2019; Deng et al., 2019; Lang et al., 2019; Liang et al., 2019; Shao et al., 2019; Xu et al., 2020; Deng et al., 2021; Yu et al., 2021). Compared to petrophysical model-based methods, e.g., the Timur-Coats equation and Windland's equation (Leverett, 1941; Timur, 1968), machine-learning approaches obtain better results by fitting more complex relationships between well logs and permeability. Common machine-learning methods used for permeability prediction include random forest, feed-forward neural network, and convolutional neural network (CNN) (Collobert and Weston, 2008; Bhattacharya and Mishra., 2018; Zhu et al., 2018; Zhong et al., 2019). Given that many models have been successfully applied to extract features from well logs to predict permeability, I decide to focus on the second factor, which is to mitigate the propagation of well-log measurement uncertainty to permeability prediction.

Understanding the statistics of well-log bias (uncertainty of well logs) can inform the correction of well logs and build better models for petrophysical property prediction. However, in almost all previous research about using machine learning methods to make permeability predictions, the uncertainty of well logs is ignored. The permeability prediction model is trained with training data that is compiled by lumping raw well log data from all available wells. By using all training data to train a single model, we implicitly assume that the measurement error and bias of well logs and permeability prediction are stationary, i.e., the error does not vary with well locations or depths, and the well-log interpretation is unique, i.e., permeability can be uniquely determined from a set of well logs. However, these assumptions are not always valid in practice. Well-log measurement error is mainly caused by different environmental conditions. Environmental conditions, such as logging tools, vendors and vintage, and borehole fluids, commonly vary with wells. Therefore, errors are rarely stationary, hampering effective multi-well permeability prediction for carbonate reservoirs (Prasad et al., 2004; Deng et al., 2019). These errors are exacerbated by the complexity of the borehole environment, as well as the behavior of drilling tools, typically alternatingly slippery and sticking, making errors vary with well location and depth along the well. Furthermore, well-log interpretation is commonly non-unique because of incomplete or inadequate measurements, whereby different formation properties may yield similar well logs (Mallan et al., 2018; Gaillot et al., 2019; Liu et al., 2019; Maalouf et al., 2020).

Physics-based preprocessing methods, such as borehole correction, and statistics-based methods, such as well-log normalization, are commonly used to mitigate the well-log error and help decrease the permeability prediction uncertainty. Physics-based correction is accurate when physical models reproduce the actual physical phenomenon and operational data are available. However, the operational data are not always accessible, and models may not reflect the reality. Therefore, in this dissertation, I mainly discuss data-driven workflows that incorporate statistics-based preprocessing methods into machine learning models. Well-log normalization is the process of re-scaling or re-calibrating well logs of a well so that they are consistent with well logs acquired in other wells within the same field or region (Shier, 2004). Wells with well logs that are interpreted, calibrated with core measurements or corrected for borehole environmental effects, are denoted as *type wells* or *training wells*, and their well logs are denoted as *type well logs* or *training well logs*, respectively, while wells with well logs that require normalization and interpretation are denoted as *test wells*, and their well logs are denoted as *test well logs*. Normalization of test well logs reduces errors introduced by variations in environmental conditions and non-uniqueness by constraining the prediction of test well logs with statistics of type well logs, thereby making models calibrated with type wells robust for test-well petrophysical property prediction.

Imposing constraints to petrophysical interpretation based on statistics of core measurements or accurate petrophysical predictions is an important aspect of petrophysics that has not been well-studied. For conventional normalization methods, e.g., the two-point scaling method (Shier, 2004), one first identifies type wells with formation properties that are regionally or globally representative. Then, each test well log is linearly normalized to match the values of type well logs in two formations with distinct formation properties. For example, the gamma-ray log values of pure shale and sandstone facies in a test well are normalized to be the same as those in type wells. The values for distinct formation properties are usually chosen as the minimum and maximum values within an interval (Shier, 2004). When petrophysical properties are stationary among test and type wells, i.e., the summary statistics of well logs do not vary among these wells, test well logs should exhibit marginal distributions similar to those of the type wells. This normalization method is also known as affine correction in geostatistics (Pyrcz and Deutsch, 2014). According to Shier (2004), there are 5 common methods for type well identification. Based on their assumptions of stationarity, they can be roughly divided into two categories (Figure 2.2):

1). **Stationary reservoir assumption**: the specified statistics of well logs are invariant over a specified interval (Figure 2.2A). The big histogram well-log normalization method (Shier, 2004) makes this assumption. In the big histogram method, one normalizes test well logs to match all type well logs in the field. I refer to this category of type well identification methods as the *stationary well method*.

2). **Non-stationary reservoir (regional stationarity) assumption**: the specified statistics of well logs are variant over a specified interval (Figure 2.2B). The well logs should not be normalized to match the global statistics. To mitigate the nonstationarity issue, spatial continuity of petrophysical properties is used to help identify type wells. If petrophysical properties are continuous regionally, the closest wells within the small region should have similar petrophysical properties (regional stationarity). Therefore, test well logs are normalized to match well logs from the nearest type wells instead of all type wells. Type well, neighbor comparisons, and the trial normalization method (Shier, 2004) make this assumption. I refer to this category of methods as the *type well* method.

There are three limitations in classical well-log normalization methods: (1) the successful application of the normalization depends heavily on the experience of the interpreter; a bad choice of normalization parameters, such as the two values representing different facies in the two-point scaling method (Shier, 2004), or a bad choice of type wells can introduce bias into the interpretation results and cause problems, such as over alignment. Over alignment is the situation where the statistics of formation properties from one well are different from those of the type wells, whereas well logs are incorrectly normalized to exhibit the same distribution. (2) Conventional normalization methods only normalize test well logs to reproduce the marginal distribution of each type well log, i.e., the histograms of each well log. However, the reproduction of marginal distributions does not guarantee the reproduction of correct correlations between normalized well logs; a misleading correlation between normalized well logs can degrade the performance of prediction models, whereby the joint distribution of multiple well logs needs to be considered. The joint distribution is the distribution of a well log given the values of other types of well logs. (3) Conventional normalization methods are linear. However, the bias introduced by environmental conditions can be nonlinear and varies with other formation properties, e.g., facies, resulting in non-linear structures that must be corrected by normalizing joint distributions.

To normalize well logs such that test well logs have joint distributions similar to those of type well logs, one can minimize the divergence between the joint distribution of type well logs and test well logs. Divergence measures, such as the Kullback–Leibler (KL) divergence (Kullback and Leibler, 1951) and Jason-Shannon (JS) divergence (Manning and Schutze, 1999), can be used to quantify the statistical dissimilarity between two joint distributions. Chang et al. (2021) use the maximum mean discrepancy domain transfer (MMDDT) learning model to predict rock facies, which implicitly imposes the spatial stationarity assumption and minimizes the maximum mean discrepancy (MMD) for the outputs of intermediate layers in a neural network, the intermediate features, during training. The intermediate features are non-linear transformations of the input well logs, thus can also be regarded as non-linearly normalized well-log features for corrected joint distributions. However, the model is not flexible enough to be applied with other pre-trained machine-learning or calibrated petrophysical models because intermediate features are not normalized well logs, we cannot directly use them in other models. Additionally, in their model, the prediction error and divergence are minimized simultaneously (synchronized); differences in the convergence time of these two loss functions lead to either overfitting or over alignment in petrophysical prediction. The output facies prediction is not constrained based on the stationarity assumption. Furthermore, the lack of physical meaning for the intermediate features makes it difficult to interpret the results and provide useful findings.

To mitigate the above limitations, I propose to use a modified asynchronized discriminative adversarial (DA) domain adaptation method (Tzeng et al., 2017) to normalize well logs and make permeability predictions. In the modified DA model, the predictive layers, which are layers that map normalized well logs to formation properties, are first trained. Then preprocessing layers are trained to normalize test well logs by minimizing the divergence between normalized test well logs and type well logs, and the divergence between associated permeability predictions through a discriminator neural network. With this structure, the prediction error of formation properties and the JS divergence are minimized asynchronously to avoid overfitting or over alignment. The predictive layers can be pre-trained petrophysical or machine-learning models, making the model more flexible. Intermediate features in the DA model are normalized well logs that are comparable to training well logs of properly selected type wells, which are more interpretable.

With this model, I also mitigate the remaining two limitations of conventional well-log normalization methods, i.e., nonlinear normalization can be performed with nonlinear preprocessing layers, and the divergence is calculated in the feature space identified by a discriminator neural network, which can avoid over alignment.

Compared to previous methods, the asynchronized DA model for multi-well petrophysical interpretation mitigates overfitting and over alignment problems, improves the accuracy and interpretability of well-log normalization and permeability prediction.

2.2 METHOD

This section first describes the data used to compare the proposed methods to conventional methods for the case of permeability prediction, then introduces the structure of the DA model for well-log normalization and permeability prediction. I use the DA model to calculate normalized test well logs and associated permeability prediction that reproduce the joint distribution of type well logs and associated permeability measurements, mitigating errors introduced by non-stationary well logs. The DA model assumes stationary formation properties and well logs from the test well and associated type wells and adds constraints to improve the accuracy of the interpretation.

Another new model proposed here to perform the normalization and permeability prediction is the linear-constraint model, which uses an ensemble of linear model predictions from the linear well-log interpretation model and the linear stationarity model to constrain the well-log normalization and interpretation instead of DA loss in a DA model. The DA, linear constraint, two-point scaling, and unconstrained interpretation workflows are compared in the Results section of this chapter to decide on the best interpretation workflow for well-log normalization and permeability prediction in the examined carbonate reservoir.

Divergence-based type well identification methods are also discussed in this section to address the problem of non-stationary formation properties among different wells and compared to the distance-based type well identification method in the Results section.

Compared to conventional well-log normalization, type well identification and well-log interpretation models, I expect the new methods to perform more effectively for multi-well petrophysical interpretation, and to predict formation properties more accurately from well logs in the presence of environmental uncertainties, spatial continuity/discontinuity, and (regional) stationarity.

2.2.1 Data Preparation

The proposed method is verified with core permeability measurements and wireline log data from the Seminole San Andres Unit (SSAU), a dolomitized carbonate reservoir located on the eastern shelf of the Central Basin, West Texas, USA (Wang et al., 1998). The SSAU has produced more than 700 million barrels of oil from the upper and lower San Andres formations, with water flooding conducted between 1960 and 1980 and CO2 flooding since the 1980s. Rock porosity in the producing reservoir zone ranges from 5% to 20%, while permeability ranges from 0.01 mD to 2000 mD (Male and Duncan, 2020). I select 30 wells with core permeability measurements and complete well logs from 625 wells drilled between 1940 and 2010. The well logs used as inputs for permeability prediction are gamma-ray (GRD), density (RHOB), neutron porosity (NPHI), and compressional slowness (DT), along with relative depth and porosity prediction. The caliper log (CALD) is used for well-log quality control. Core porosity (CPOR) and maximum horizontal permeability (CKMAX) from cores are used to calibrate and validate my interpretation workflow (Figure 2.3).

Several steps are taken to perform the quality control: (1) Abnormal spikes and outliers in well logs are evaluated for potential errors; (2) caliper logs are used to identify intervals with severe borehole washouts; (3) well logs are depth shifted by matching the troughs and peaks of core porosities and the interpreted porosity log.

Wells are divided into the training set consisting of type wells and test set consisting of test wells to train and validate the proposed method, respectively. Cross-validation is performed to determine the optimal combination of well logs and hyperparameters for permeability prediction. Core permeability is log-transformed; all well logs are min/max normalized to a minimum of -1 and a maximum of 1 to improve the performance of the gradient-based optimization method for machine-learning model training.

2.2.2 Discriminative Adversarial (DA) Model

The proposed DA model has a model structure similar to that of the generative adversarial neural networks (GAN). As shown in Figure 2.4, there are two neural networks in the DA model, the first one is denoted as the generator (G), while the second one is denoted as the discriminator (D). During training, the discriminator is optimized to distinguish the normalized well logs and petrophysical predictions of the type wells from those of the test wells, and output 1 for the type wells and 0 for test wells. The generator is optimized to calculate the normalized well logs and predict formation properties in the test wells, such that the statistical distributions of well logs and properties are similar to those of the type wells, making the discriminator fail to distinguish the outputs of the generator from the data of the training set (update 2 in Figure 2.4). The generator is also responsible for minimizing the prediction errors in type wells (update 1 in Figure 2.4). Both generator and discriminator are trained adversarially until the generator outputs normalized well logs and petrophysical property predictions for the test wells that reproduce the statistics observed for type wells, and Nash's equilibrium is reached (Goodfellow et al., 2014). Due to noise and bias present in well logs, which are caused by various borehole environmental conditions, e.g., irregular caliper, noisy and inadequate measurements, wells penetrating similar formation properties may exhibit different well logs.

The generator can be further divided into two parts (Figure 2.4), the preprocessing layers (P) normalizing well logs and the mapping layers (M) mapping normalized well logs to formation properties. Preprocessing layers calculate normalized well logs ($\tilde{X}_s, \tilde{X}_t$) from well logs of the training set (X_s) and test set (X_t) with the same structure but different weights and biases (P_s, P_t); when P_s is an identical mapping, and P_t is a linear mapping, the preprocessor is equivalent to the conventional linear normalization. Mapping layers (M) for $\tilde{X}_s$ and $\tilde{X}_t$ are the same, where petrophysical property predictions for the training set ($\tilde{Y}_s$) and the test set ($\tilde{Y}_t$) are calculated. Mapping layers are optimized to minimize the prediction errors of the training set (X_s, Y_s), cross-validation is applied to obtain optimal weights and biases of mapping layers that avoid overfitting. Mapping layers are the only layers that exist in a conventional, unconstrained machine-learning model. In the DA model, mapping layers can be a pre-trained machine-learning model or a classical petrophysical model that does not overfit the training data. Algorithm 2.1 summarizes the training process of the asynchronized discriminative adversarial model. The objective functions for the discriminator and the generator are given by

$$\min_{D} \mathcal{L}_{adv_D}(X_s, X_t, P_s, P_t, M\ ) = -\mathbb{E}_{x_s}\left[\log D\left(M\big(P_s(X_s)\big), P_s(X_s)\right)\right] - \mathbb{E}_{x_t}\left[\log\left(1 - D\left(M\big(P_t(X_t)\big), P_s(X_s)\right)\right)\right] \tag{2.1}$$

$$\min_{P_t} \mathcal{L}_{adv_G}(X_t, M, D\ ) = -\mathbb{E}_{x_t}\left[\log D\left(M\big(P_t(X_t)\big)\right)\right] \tag{2.2}$$

$$\min_{P_s, M} \mathcal{L}_{pred}(X_s, Y_s\ ) = \mathbb{E}_{x_s, y_s}\left[\left\|Y_s - M\big(P_s(X_s)\big)\right\|_2\ \right], \tag{2.3}$$

where $\mathcal{L}_{adv_D}$ is the discriminator adversarial loss and $\mathcal{L}_{adv_G}$ is the generator adversarial loss. The $\mathcal{L}_{pred}$ term in Eq. 2.3 is the mean-squared error (MSE) of the prediction for the continuous response feature and can be replaced with categorical cross-entropy for categorical output or other types of errors that are commonly used in machine-learning models. The mapping layers can be replaced with pre-trained petrophysical or machine-learning models, and in these cases, Eq. 2.3 is not used to train the pre-trained models to avoid overfitting. The model trained with Eq. 2.3 only is denoted as the original (unconstrained) model because no preprocessing layers are used for well-log normalization. The other loss functions (Eqs. 2.1 and 2.2) are formulated adversarially, the generator is trained to minimize the probability of fake assigned by the discriminator to predictions from the generator (Eq. 2.2), and the discriminator is trained to maximize the probability of assigning fake to predictions from the generator (Eq. 2.1). When the model is trained in batch, the total probability is the multiplication of the probability of each sample, which can be very small when the batch size is large. To avoid truncation error and vanishing gradient, the logarithm of probability is used as the loss function, so that the loss of each sample is additive, and the expectation is the arithmetic mean of the logarithmic probability.

When bias between the well logs of the training and test sets is deemed negligible, high certainty should be assigned to unconstrained predictions and slight normalization should be performed to avoid over alignment. In this latter case, another loss term to quantify the certainty of unconstrained prediction is added to Eq. 2.2, such that Eq. 2.2 is modified into Eq. 2.2* as follows:

$$\min_{P_t} \mathcal{L}_{adv_{GC}}(X_t, P_s, M, D, \lambda) = -\mathbb{E}_{x_t}\left[\log D\left(M\big(P_t(X_t)\big)\right)\right] + \lambda \mathbb{E}_{x_t}\left[\left\| M\big(P_t(X_t)\big) - M\big(P_s(X_t)\big)\right\|_2\right], \tag{2.2*}$$

where λ quantifies the certainty of unbiased well logs in the test set and λ is set to 0 in my workflow to impose high uncertainty to test well logs. The L2 constraint term ($\| \quad \|_2$) can be replaced with other types of loss functions for the prediction of other types of formation properties, such as categorical cross-entropy for categorical output for rock facies prediction; $M\big(P_t(X_t)\big)$ is equal to $\tilde{Y}_t$ in Algorithm 2.1.

When a pre-trained model is used as the mapping layers, and the gradient is not accessible, such as tree models and black-box commercial interpretation algorithms, a simple model, such as the random forest (RF) is used as the discriminator. The RF discriminator calculates the $\mathcal{L}_{adv_D}$ with cross-validation to avoid overfitting and the optimum model parameters for P_s are obtained through grid search.

To apply the DA model for well-log normalization and permeability prediction, two assumptions need to be made: (1) well logs and core measurements from the type wells are of good quality and petrophysical properties are stationary among a test well and associated type wells. I recommend the following three steps to improve the stationarity between wells: first dividing well logs into zones, then performing well correlation, and finally training the DA model for each zone. (2) Type wells exhaustively sample the formation penetrated by test wells, i.e., one can find at least one type well with petrophysical property distribution similar to any of the test wells. When the type wells have biased samples compared to the test wells, data balancing and semi-supervised learning should be applied.

To make these two assumptions valid, proper selection of type well(s) for a test well is important. To choose the type well(s), I propose two divergence-based type well identification methods for reservoirs with stationary and non-stationary petrophysical property distribution. These methods better capture the statistical similarities between training and test wells, compared to the classical, distance-based type well identification method, which only considers spatial distance and assumes spatial continuity of formation properties. The statistical similarity is a better metric to choose training wells that exhibit petrophysical property statistics similar to those of a test well, especially in the case where formation properties are non-stationary among wells, e.g., adjacent wells may penetrate different zones.

2.2.3 Type-Well Identification with Statistical Distance

Type wells should be selected to have formation properties similar to those of a test well. Because of spatial continuity and stationarity of petrophysical property distribution, spatial distance is commonly used, i.e., a type well for a test well is the well spatially closest to the test well. This type of well identification method is the conventional type well method (Shier, 2004), and assumes spatial continuity, where two adjacent wells should exhibit similar formation properties.

$$Dist(i,j) = \sqrt[2]{\left(loc_{x_i} - loc_{x_j}\right)^2 + \left(loc_{y_i} - loc_{y_j}\right)^2} \tag{2.4}$$

where $Dist(i,j)$ is the distance between well i and well j, loc_x and loc_y are the x and y coordinates of the interval of interest within well i and j.

However, when formation properties are non-stationary, zone thickness varies at different well locations, wells penetrate different zones, and well spacing is large, spatially close wells may not have similar well-log and petrophysical property distribution, e.g., in a complex depositional environment, depositional environments and architectural elements varies with region, spatially close wells do not necessarily penetrate the same architectural elements or stratigraphic intervals.

Therefore, we propose to directly calculate the statistical similarity between wells to identify type wells, i.e., the divergence between the well logs of each pair of wells (Pérez-Cruz, 2008; Sasaki et al., 2015). Wells with small divergence to the test well are identified as the type wells. The JS divergence between wells is calculated as the sum of two KL divergences. The JS divergence calculation is as follows:

$$\begin{aligned} Div(i,j) &= KL(P_i||P_j) + KL\left(P_j||P_i\right) \\ &= -\sum P_i(X)\log\left(\frac{P_j(X)}{P_i(X)}\right) - \sum P_j(x)\log\left(\frac{P_i(X)}{P_j(X)}\right) \end{aligned} \tag{2.5}$$

where $Div(i,j)$ is the JS divergence between the well logs (X) of well i and j, which is the sum of the KL divergence between well logs from the two wells; it is calculated for each zone; $P_i(X)$ is the probability of having well log measurements around x in well i, nearest neighbor method is used to calculate the probability (Wang, et al., 2009). When no zonation information is available, data coverage of well i by well j ($KL(P_i\|P_j)$) is calculated and used for type well selection. In this chapter, I use the JS divergence of density, neutron, and sonic logs between wells to identify the type wells.

Depending on whether the type wells for each test well are the same, I further define the divergence-based method into two methods. When the formation properties are stationary, we may use all type wells with similar statistics to train a single predictive model and normalize test wells, this method is denoted as the stationary well method. While when formation properties are not stationary, depositional patterns/environments vary with regions, a test well is corrected using well logs from type wells that are statistically similar to it, type wells vary with the test well. I denote this method as the type well method.

Therefore, in this study, three training and testing splitting strategies are discussed: 1) the spatial distance-based type well method, which assumes a non-stationary petrophysical property distribution and identifies type wells for each test well with spatial distance, 2) the statistical distance-based type well method, which assumes non-stationary petrophysical property distributions and identifies type wells for each test well with divergence, and 3) the stationary well method, which assumes a stationary petrophysical property distribution and identifies type wells for all test wells with divergence. For methods (1) and (2), the weights of mapping layers vary for different test wells, while for method (3), only one set of mapping layers is trained with all the data from all training wells.

Cross plots and histograms of well logs and core measurements of all the wells are visualized and analyzed to support the stationarity assumption for the reservoir and find potentially biased test wells. Additionally, to ascertain the statistical similarity, divergences between type wells and test wells are visualized with multi-dimensional scaling (MDS) (Borg and Groenen, 2005), where wells are mapped to a 2-D feature space that maximizes the reproduction of the pairwise divergence as pairwise separation distance. The isolation forest method (Liu et al., 2008) is used to identify wells with abnormal well logs, i.e., outlier wells whose distances to other wells are large.

2.2.4 Model with Linear Constraints

The DA model normalizes well logs by imposing the DA loss constraints; it is important to compare the DA constraint to other common constraints. Therefore, I compare the DA model to the machine-learning model with linear model constraints. The linear constraint model has the same model structure as the DA model, except that it does not use the DA loss to optimize the preprocessing layers; instead, it optimizes the preprocessing so that the output permeability predictions are consistent with the predictions obtained from the unconstrained model and all types of linear models.

The linear model ensembles include a stationarity constraint and linear models between well logs with high certainty and permeability. With the stationarity constraint and linear models between well logs and permeability, we can decrease the model variance and improve the prediction accuracy. The assumption made for the linear constraint model is that the distribution of petrophysical property, i.e., logarithmic permeability, is stationary and that the distribution of the prediction error of the linearly constrained model is also stationary.

To impose the stationarity constraint for a test well and associated type well(s), the mean value of a petrophysical property, the global proportion of different facies, and their spatial covariance are assumed stationary among a test well and associated training wells. The spatial statistics are then used to perform the prediction of formation properties. Due to the spatial heterogeneity of the reservoir, properties such as permeability have a limited spatial continuity; therefore, for permeability prediction, I only use the mean value to constrain the prediction, i.e.,

$$\overline{Y_s} = \mathbb{E}_{y_s}[Y_s], \tag{2.6}$$

where $\overline{Y_s}$ is the average value of the petrophysical property of type wells for a test well.

For the prediction of continuous formation properties, such as porosity, the Kriging method instead of the mean value is used to impose the constraint. With the Kriging method, the formation property prediction ($\overline{Y_s}$) is the weighted (m_i) average of nearby formation properties (Y_s) at a lag distance of s_i (Eq. 2.6*). The weight (m_i) is determined through variogram calculated from type wells, I refer interested readers to Pyrcz and Deutsch (2014) for more information.

$$\overline{Y_s} = \sum_{i=1}^{N} m_i Y_s[s_i] \tag{2.6*}$$

To impose the linear well-log interpretation model constraint, a simple linear model or petrophysical model is used to predict formation properties from well logs that are believed less likely to be affected by the borehole logging environment and logging tools, e.g., density log (RHOB), i.e.,

$$\min_{A,B} \mathcal{L}_{linear}\left(X_{s_u}\right) = \mathbb{E}_{x_s,y_s}\left[\left\|AX_{s_u} + B - Y_s\right\|_2\right] \tag{2.7}$$
$$\tilde{Y}_{s_l} = AX_{s_u} + B,$$

where A and B are coefficients of the linear model calibrated with the training data, X_{s_u} are the reliable well logs of type wells for a test well, and $\tilde{Y}_{s_l}$ is the prediction of the linear model for the training set.

To combine different types of linear predictions, the covariance matrix of the predictions of different models is used to weight the predictions from different models. The variance of the ML model predictions is calculated with the K-fold cross-validation, i.e., the covariance between predicted and true formation properties of the validation set instead of the training set is calculated and used to represent the uncertainty of different predictions, thereby constraining the prediction of the complex mapping model and avoiding potential overfitting; the corresponding loss function is written as

$$C_d = \begin{bmatrix} \frac{Cov\left(M\left(P_s(X_s)\right), Y_s\right)}{\lambda_l^2} & \frac{Cov\left(M\left(P_s(X_s)\right), \overline{Y_s}\right)}{\lambda_l} & \frac{Cov\left(\tilde{Y}_{s_l}, M\left(P_s(X_s)\right)\right)}{\lambda_l} \\ \frac{Cov\left(M\left(P_s(X_s)\right), \overline{Y_s}\right)}{\lambda_l} & Cov\left(\overline{Y_s}, Y_s\right) & Cov\left(\overline{Y_s}, \tilde{Y}_{s_l}\right) \\ \frac{Cov\left(\tilde{Y}_{s_l}, M\left(P_s(X_s)\right)\right)}{\lambda_l} & Cov\left(\overline{Y_s}, \tilde{Y}_{s_l}\right) & Cov\left(\tilde{Y}_{s_l}, Y_s\right) \end{bmatrix} \tag{2.8}$$

$$E = \left[M\left(P_t(X_t)\right) - M\left(P_s(X_t)\right);\ M\left(P_t(X_t)\right) - \bar{Y}_s; M\left(P_t(X_t)\right) - \left(AX_{t_u} + B\right)\right]$$
$$\min_{P_t} \mathcal{L}_{lc}(X_s, X_t, Y_s, P_s, M) = \mathbb{E}_{x_t}[E^T C_d^{-1} E],$$

where Cov is the covariance of the predictions of two methods, λ_l is similar to λ, quantifying the certainty that well logs of a test well and associated type wells have the same logging environment, E is the array of differences between different predictions, and $\mathcal{L}_{lc}$ is the linear constraint added to Eq. 2.3. During training, the linear constraint (Eq. 2.8) instead of the adversarial loss (Eqs. 2.1 and 2.2) is optimized after the optimization of the P_s and M with Eq. 2.3.

2.2.5 Design of Numerical Experiments

Machine-Learning workflows without any constraints (conventional machine-learning method), the DA model, the model with two-point scaling normalization, and the model with linear constraints are compared. Two-point scaling method normalizes the test well logs to match the distribution of type well logs by matching the maximum and minimum values, the corresponding equation is written as:

$$\widetilde{X_t} = \min\,(X_s) + \frac{(\max\,(X_s) - \min\,(X_s))(X_t - \min(X_t))}{(\max(X_t) - \min\,(X_t))} \tag{2.9}$$

where the 10% and 90% quantiles are regarded as the minimum and maximum values to avoid the effects of outliers.

The structures of P_s and M layers are identical for all workflows, and only the normalization layers of the test set (P_t), and loss functions vary in different workflows and are summarized as follows:

1). In conventional machine-learning workflows, the test data normalization layer (P_t) is an identical mapping layer, i.e., normalized well logs are the same as the original well logs as no normalization is performed. Only update 1 (Figure 2.4) is performed, and only the prediction MSE loss of Eq. 2.3 is minimized to update the mapping layer (M).

2). In the two-point scaling method, the test data normalization layer (P_t) is replaced with the two-point normalization operation, only the prediction MSE loss of Eq.2.3 is minimized to update the mapping layer (M).

3). In the DA workflow, the test data normalization layer (P_t) is determined through Eq. 2.2 or Eq. 2.2*, both adversarial and prediction MSE loss (Eqs. 2.1, 2.2, and 2.3) are used to update the mapping layer (M) and test well normalization layer (P_t).

4). In the model with linear constraints, the test data normalization layer (P_t) is determined through Eq. 2.8 and Eq. 2.3 is used to update the mapping layer (M).

Three different type-well identification methods and four workflows, a total of 12 conditions, are compared. All 30 wells are used for the numerical experiment, the training testing data split is based on the jackknife test method, a.k.a. the leave-one-out validation method, i.e., each time a well is selected from all wells as the test well while the type wells are selected from the remaining wells. For the type well methods, one training well is selected for each test well from the rest 29 wells, while for the stationary well method, 6 wells are selected from the 30 wells to be the training wells that have the shortest distances to the other non-outlier wells, if the test well is one of the training well, then only the rest 5 wells are used for training. The 6 training wells are kept the same when they are used to train a prediction model for test wells. I apply these schemes to train and test different permeability prediction models, and the permeability predictions of each model are validated against core measurements. The performances of the different type well identification methods and prediction models are evaluated based on the MSE of permeability predictions (Eq. 2.10). the MSE is first calculated for each test well, and the performance is evaluated by averaging the MSE of all test wells. The performance of different workflows on wells identified as outlier test well using MDS and isolation forest and non-outlier test wells are discussed respectively.

$$MSE = \left\| Y_t - \widetilde{Y_t} \right\|_2 \tag{2.10}$$

2.3 RESULTS

I first visualize well logs of all wells to identify abnormal well logs that may need normalization. Then divergence-based type wells are calculated and visualized. Finally, I visualize the normalized well logs and associated permeability prediction for two wells and summarize the MSE of permeability prediction of all 12 scenarios to determine the best workflow for well-log normalization and permeability prediction.

2.3.1 Well-Log Visualization

I visualize the pairwise cross plots (bivariate joints) and the marginal distribution of well logs from all 30 wells in Figure 2.5. Cross plots between porosity core measurements (CPOR) and permeability core measurements (CKMAX) from different wells are similar, indicating a stationary carbonate reservoir. Cross plots and histograms of well logs indicate that biases exist in the sonic logs (DT) and neutron logs (NPHI) of some of the wells, which will be corrected with the normalization models in the following sections. Abnormal wells can be identified by observing the scatter plots in Figure 2.5. For the same density and neutron porosity values, the abnormal wells have abnormally high sonic well logs compared to other wells, which can lead to an overestimate of porosity and permeability. Possible causes for the abnormal sonic log are different sonic logging tools, and logging vintage.

Even though formation properties from core measurements are stationary, the bias introduced by the measurement environments, such as different logging tools, vendors, and vintages may not be stationary; therefore, I also compare results obtained with both the stationary well method and the type well method.

2.3.2 Type Well Identification

Figure 2.6 shows the locations of all the wells available for my study. For the distance-based type well identification method we select training wells as the wells closest to the test wells. To better understand the statistical similarity of well logs between wells, the divergence between each pair of wells is calculated and summarized as the distance matrix in Figure 2.7. In the distance matrix, a large distance between two wells indicates a huge difference in their well log distribution, whereas a small divergence indicates a similar distribution. It is obvious from the distance matrix that well 9 and well 24 have large distances to other wells, which indicates the associated well-log joint distributions are different from others. Therefore, I refer to them as the outlier test wells. In Figure 2.8, the 2D multiple dimensional scaling (MDS) map calculated from the divergence matrix helps to visualize the statistical distance between the wells. Each point in Figure 2.8 represents a well and the distances (lines) between them is the divergence, the x- and y-axis do not have a physical meaning, they are embedded features to reproduce the statistical distance between wells. Wells 9 and 24 (yellow) are identified as outlier wells with isolation forest with the parameterization of the MDS method. In the stationary well method, 20% of wells with the smallest distances to the center of the well cloud are used as the training wells (green), and the other wells (blue) are not used for training, while in the divergence-based type well method, the well statistically closest to a test well is identified as the training well, no matter if it is close to the center.

2.3.3 Permeability Prediction and Normalized Well Logs Calculated with Different Methods

Permeability prediction for all wells is performed with the 12 combinations of methods and the MSE of prediction is calculated. Tables 2.2 and 2.3 summarize the average MSE of the permeability predictions for the two outlier test wells and 28 non-outlier test wells. The following observations stem from the two tables:

1) Compared to models without constraints, all types of constraints discussed above improve the performance of the permeability prediction model.
2) For outlier test wells, the DA model combined with the stationary type well identification method yields the best permeability predictions.
3) For non-outlier test wells, the DA model combined with the divergence-based type well identification method yields the best permeability predictions.
4) For the training well selection strategy, the distance-based type well method exhibits the highest MSE, regardless of the constrained model used. The differences between permeability predictions obtained with the divergence-based type well and stationary well methods are small for test wells that are not outliers.

Permeability predictions and permeability core measurements from the outlier well 24 are compared in the first four tracks in Figure 2.9. Compared to predictions without normalization (K_origin), the two-point scaling, DA constraint, and linear constraint methods yield the best permeability predictions. Permeability prediction with the DA method (K_DA) has the lowest MSE. For tracks 5 to 8, the normalized and original well logs are compared, the correction to sonic log (DT) is large for all three methods, and the DA constraint method predicts the lowest normalized compressional slowness compared to other methods. While differences between normalized and original nuclear logs are small for the DA method, well logs normalized with the linear constraint method are smoother than the original well logs, and the average value of the density log normalized with the two-point scaling method decreases by 3% compared to the original density log.

Figure 2.10 summarizes the multivariate statistics of normalized well logs and permeability. The distribution of well logs (orange, "Test") of the outlier test well is different from that of the training well logs (blue. "train"). Predictions obtained without well-log normalization (green, "Origin") overestimate the permeability due to the biased sonic log; the prediction and normalized well logs calculated with the linear constraint method (red, "Linear constraint") have a smaller variance and a higher correlation than those calculated with other methods. Normalized well logs calculated with the two-point scaling method (pink, "Two-point scaling") reproduce the univariate statistics of the training well logs, while normalized well logs calculated with the DA method (brown, "DA") and reproduce the joint distribution of the training well logs. Compared to other methods, the variance of permeability predicted with the linear constraint method (K_linear) decreases 23% on average, while the correlation coefficient of normalized well logs increases 11 % on average. Marginal distributions of normalized well logs calculated with both the two-point scaling and DA methods match those of the training wells.

Figure 2.11 compares the permeability predictions and normalized well logs from one of the non-outlier test wells, well No. 0. Prediction errors are low for all four methods, and corrections to well logs are small for the DA and two-point scaling methods, while the linear constraint method smooths and increases the sonic log after normalization. The pairwise, multivariate statistics of well logs and permeability predictions in Figure 2.12

show that the normalized well logs are similar to the training well logs except for the linear constraint method. The distribution of well logs (orange, “Test”) from this well exhibits univariate and pairwise statistics similar to those of the training well logs (blue. “train”). Permeability predictions and normalized well logs calculated with the original (green, “Origin”), DA (brown, “DA”), and two-point scaling (pink, “Two-point scaling”) methods all reproduce the distribution of the training well logs, while permeability predictions and normalized well logs calculated with the linear constraint method (red, “Linear constraint”) have smaller variance and higher correlation compared to other methods.

The divergence of well logs and permeability predictions between the test and type wells is calculated for every iteration of DA (blue) model training, and the final iterations of two-point scaling (red) and unconstrained (yellow) models. Figure 2.13 compares the divergence with the MSE of permeability prediction. A lower divergence indicates that the normalized well logs better reproduce the distribution of training well logs. Training of all three constrained models decreases the divergence and better predicts the permeability. The DA model at its lowest divergence point (blue) has the lowest error, followed by the two-point scaling method (red) and the original model (yellow). Also, the two-point scaling method may have lower divergence than the DA model (A) due to over alignment. The DA model training is an iterative optimization process: the error does not monotonically decrease or increase; instead, the model normalizes well logs and makes predictions to explore the solution space iteratively, guided by discriminators optimized at different epochs, where the optimal output can be determined as the point with the lowest divergence. In Figure 2.14, the discriminator accuracy is calculated and compared to the MSE of permeability prediction.

A strong correlation exists between the divergence and the MSE of permeability prediction and between the discriminator accuracy and the MSE. Because the DA model training is an iterative optimization process, we determine the optimal permeability predictions of the DA model by only keeping the iteration with the lowest divergence/ discriminator accuracy. Although the two-point scaling method sometimes has a lower divergence, the DA method yields more accurate permeability predictions. Compared to the other two methods, the DA method has the lowest discriminator accuracy.

In Figure 2.15, cross-plots of predicted permeability and permeability core measurements of all wells indicate that no obvious bias exists in any of the predictions obtained with the four methods, while the DA method has the lowest error.

2.4 DISCUSSION

2.4.1 Comparison of Different Type Well Identification Methods

As shown in Tables 2.2 and 2.3, permeability predictions calculated with the distance-based type well method have the highest error compared to the divergence-based methods, indicating a non-stationary petrophysical property distribution and/or different environmental effects between spatially adjacent wells. Wells that are spatially close to each other do not necessarily have similar petrophysical property distributions or borehole environments, resulting in different statistics of well logs in adjacent wells, which introduces the non-uniqueness and measurement bias and degrades the performance of machine-learning models. Divergence-based type well and stationary well methods mitigate this adverse behavior by training machine-learning models with only the training wells with small well-log joint distribution divergence to test wells, i.e., the distribution of well logs and formation properties of the test wells are similar to those of the training wells, and the training data are better adapted to the test data.

For outlier test wells, the stationary well method has better performance than the divergence-based type well method. Outlier test wells have petrophysical property statistics or borehole environments that are very different from other wells, whereby it is difficult to find training wells with formation properties and borehole environments similar to those of the outlier test wells. Consequently, constraining the interpretation with global unbiased statistics yields better permeability predictions.

For other test wells, the divergence-based type well method is better than the stationary well method because wells with similar logging environments and petrophysical property statistics are available, and only minor well-log normalization is needed for the prediction.

2.4.2 Comparison of Different Permeability Prediction Models

The performances of different methods are compared for outlier and non-outlier test wells identified with isolation forests and are summarized in Tables 2.2 and 2.3. The performances of different methods for imposing constraints can be ranked as follows: top performance is for the DA method, followed by the linear constraint method, then the two-point scaling method and the worst performance is for the original model without constraint.

Normalized well logs and permeability predictions obtained with the different methods vary in multivariate statistics as shown in Figures 2.9 and 2.12. The differences are as follows:

1) The linear constraint method constrains the original model with the average permeability and a simple linear relationship between reliable well logs and permeability. By decreasing model variability, the model is less prone to overfitting the training data, resulting in a stronger linear correlation between permeability predictions and well logs.
2) The two-point scaling method reproduces marginal distributions of well logs. It normalizes well logs to have a small divergence to the training wells. However,

failure to consider the joint distribution of well logs and predicted permeability causes degradation of the prediction accuracy.

3) The DA method is designed to reproduce the joint distribution of well logs and permeability distribution (Figure 2.4). However, it is found that the approximated divergence can be higher than for the two-point scaling method, as shown in Figure 2.13A. Two possible explanations, besides an inaccurate divergence approximation, for this behavior are as follows: (1) the DA method is not likely to over-align the training data, e.g., for a perfect discriminator and shallow P_S layers, if the test set is a biased subset of the training set. The best strategy for P_S layers to "fool" the discriminator is to perform an identical mapping instead of minimizing the divergence; therefore, the DA method is robust to potential over-alignment, (2) P_S layers are trained to minimize the distance between the high-level features extracted by the discriminator instead of the divergence of the normalized well logs and permeability, i.e., discriminator accuracy (Figure 2.14); consequently, the associated features are better representations of the relationship between well logs and permeability.
4) The performance of the original model without any constraints is degraded by different borehole environmental conditions and the non-uniqueness of well-log interpretation.

Overall, the DA method yields the best permeability prediction by considering the multivariate statistics and high-level features extracted by the discriminator.

2.4.3 Convergence of the DA Method

The training of the P_S layers in the DA model is a dynamic process, i.e., the P_S layers and the discriminator are optimized in an adversarial way. There is no clear indicator for the end of the training process for the DA model, i.e., the training continues as long as the training of the generator or discriminator does not overwhelm the training of the other. However, as shown in Figures 2.13 and 2.14, a strong correlation exists between the divergence, discriminator accuracy, and prediction mismatch. Therefore, I propose to use the discriminator accuracy or divergence to determine the end of the training, where the training should be long enough to obtain a result with small discriminator accuracy and divergence, while the permeability predictions obtained at the iteration with the lowest possible discriminator accuracy or divergence are taken as the final prediction.

2.4.4 Computational Time

On a standard desktop, it takes an average of 160 seconds of CPU time to train a DA model, 150 seconds to train a linear-constraint model, and 120 seconds to train a model without normalization or with two-point scaling normalization. Despite the longer training time for DA and linear-constraint models, the normalization module is integrated with the interpretation module within the model structure, which saves the extra time and effort for manual well-log normalization. It usually takes many iterations and several minutes for each iteration to perform the manual well-log normalization of each well.

2.4.5 Comparison to Petrophysical Model

The multimineral analysis is performed to obtain the porosity and saturation predictions for outlier well No. 24 without normalizing the sonic well log. Petrophysical model, the Timur equation, is used to calculate the permeability from porosity and water saturation. Figure 2.16 compares the petrophysical permeability prediction to other predictions. The petrophysical model yield better permeability predictions except for the DA prediction . There are two reasons for the good petrophysical model prediction: (1) The high uncertainty assigned to the sonic log makes multimineral analysis yield a more accurate prediction for porosity, which is used to predict permeability. (2) The simple petrophysical model, which uses porosity and saturation to predict permeability, is more robust and general compared to complex models.

2.5 CONCLUSIONS

For the first time, I provided geostatistical insights and assumptions of classical well-log normalization methods for consistent quantification of petrophysical properties from well logs acquired in multiple neighboring wells, i.e., the stationarity of formation properties. I found that statistical distance-based type well identification methods are better than the distance-based type well identification method for permeability prediction from well logs. While the permeability prediction error ((log mD)^2) of the distance-based type well identification method is between 0.51 and 0.91, the error of statistical distance-based type well identification methods is between 0.4 and 0.8. Compared to the distance-based method, the statistical distance-based method decreases the permeability prediction error by 20-40%. The statistical distance-based type well identification method improves the interpretation accuracy by better adapting test wells to training wells with borehole environmental conditions and formation properties similar to the test well. Therefore, I recommend using the divergence-based type well identification method for well-log normalization in test wells without obvious measurement biases and noise, while using the stationary type well identification method for test wells with well-log statistics very different from those of training wells.

With the two new, constrained, machine learning-based, multi-well petrophysical interpretation workflows introduced in this chapter, i.e., the linearly constrained and DA models integrated with statistical distance-based type well identification strategy, I successfully decreased the petrophysical interpretation error introduced by logging vintage, vendors, and borehole environments of different wells, and greatly decreased the time and effort required for manual well-log normalization and interpretation. While the permeability prediction error without constraints is between 0.57 and 1.6, the error of permeability prediction with constraints is between 0.43 and 0.91. Compared to classical machine-learning models without constraints, the linear constraint model decreases the permeability prediction error by 10%-50%, while the DA model decreases the permeability prediction error by 20-60%. I found that the enforcement of proper constraints greatly improved the accuracy of petrophysical interpretation; hence, I propose to use either the DA model or the linear constraint model for machine-learning-based well-log interpretation.

Accurate formation properties predicted with my proposed statistical distance-based type well identification method and constrained machine-learning model help to construct reservoir models that provide more accurate reserve-volume estimates and production forecasts and help with decision-making in reservoir development.

Both the statistical distance-based type well identification method and the constrained machine-learning model assume that well logs are stationary among training and test wells, thus proper zonation is necessary for the successful application of my interpretation workflow. In the future, I will examine the possibility of performing automatic zonation to further automate the petrophysical interpretation procedure.

Table 2.1: Summary of loss functions, calibration methods, and normalization operations of different well-log normalization and interpretation methods. Two-point scaling method normalizes test well logs to match the histograms (univariate statistics) of training well logs; the normalization is performed before the training of the permeability prediction model (asynchronized); the normalization is performed via linear operations. The maximum mean discrepancy domain transfer (MMDDT) method performs normalization by minimizing the maximum mean discrepancy (MMD) between training and test well logs; the objective functions of the normalization and predictive models are optimized simultaneously (synchronized); the MMDDT method supports both linear and non-linear normalization of well logs. The discriminative adversarial (DA) method normalizes test well logs to minimize the Jason-Shannon divergence (JSD) to the training well logs; the normalization model is trained after the training of the permeability prediction model (asynchronized); the DA model supports both linear and non-linear normalization of well logs.

Methods	Loss	Calibration	Operation
Two-point scaling	univariate statistics	asynchronized	linear
MMDDT	MMD	synchronized	(non)linear
DA	JSD	asynchronized	(non)linear

Table 2.2: MSE of logarithmic permeability predictions for outlier test wells. Without proper constraints, the MSE can be greater than one order of magnitude (1.6299). Adding constraints and properly normalizing the well logs help to decrease the permeability prediction error.

Methods	No constraint	Two-point scaling	Linear constraint	DA loss constraint
Divergence-based type well	0.76077	0.800165	0.617754	0.628871
Distance-based type well	1.25534	0.740518	0.652266	0.91469
Stationary well method	1.6299	0.653783	0.691621	0.588523

Table 2.3: MSE of logarithmic permeability predictions for non-outlier test wells. The overall MSE is lower than that for outlier test wells. Adding constraints and properly normalizing the well logs also help to increase to decrease the permeability prediction error.

Methods	No constraint	Two-point scaling	Linear constraint	DA loss constraint
Divergence-based type well	0.584184	0.529513	0.452425	0.427909
Distance-based type well	0.745191	0.592629	0.517844	0.595696
Stationary well method	0.571057	0.509348	0.453453	0.438051

Algorithm 2.1: Asynchronized discriminative adversarial (DA) model for petrophysical interpretation.

1. Calibrate petrophysical models or train machine-learning models (P_s, M) according to Eq. 2.3, with the training data (X_s and Y_s) from type wells and perform K-fold cross-validation to avoid overfitting of the training data.
2. Fix and save the model parameters obtained in the first step.
3. Use the model obtained in the previous step to calculate $\tilde{Y}_s$ and $\tilde{Y}_t$ with X_s and X_t, respectively.

   For number of training iterations do
   - Sample minibatch x_s, $\tilde{y}_s$ from $X_s, \tilde{Y}_s$, and x_t, $\tilde{y}_t$ from $X_s, \tilde{Y}_t$
   - Update the discriminator (D) by descending the discriminator loss of Eq. 2.1
   - Update the preprocessing layers for the test set (P_s) by descending the generator loss of Eq 2*

   End for
4. Save the weights of P_s when the $\mathcal{L}_{adv_{GC}}$ is small.
5. Make predictions for the test set with P_s and M.

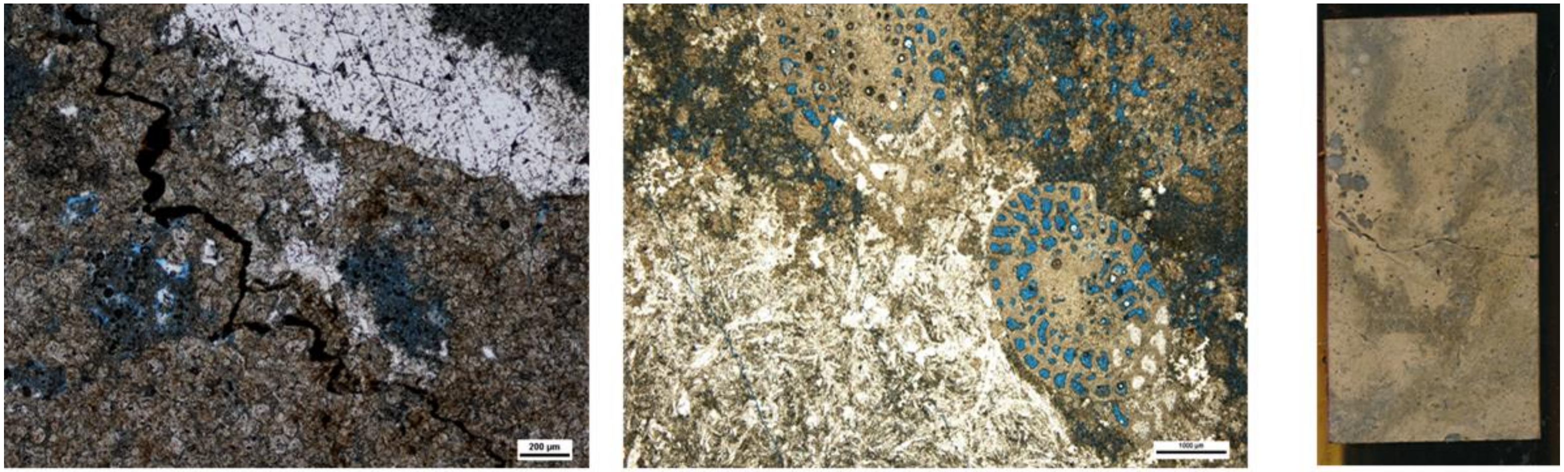

(A) (B) (C)

Figure 2.1: Optical microscope images and core images from cores of the Seminole San Andres Unit (SSAU), taken by Almirall. Open Fractures at small (A) and large scales (C), filled and void pores (B) in carbonates make the accurate characterization of connectivity between pores difficult, resulting in a weaker correlation between porosity and permeability than for the case of sandstones, thereby posing formidable challenges for permeability prediction.

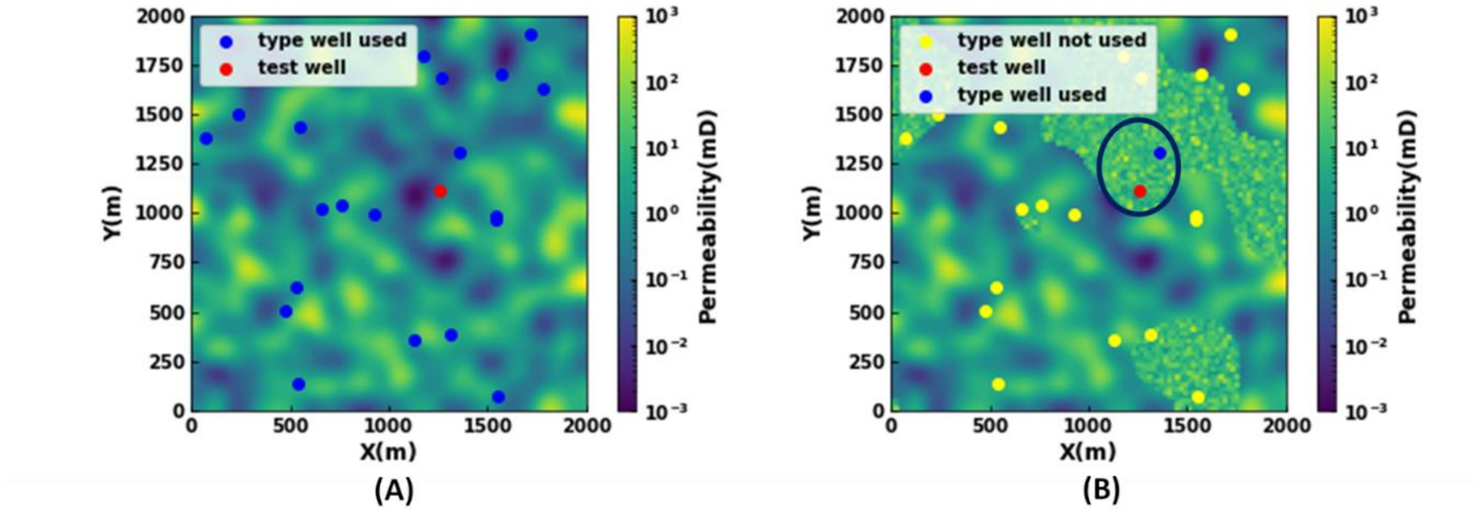

Figure 2.2: Well-log normalization methods based on different assumptions. (A) In a stationary reservoir, the statistics of well logs from a test well (red) are normalized to match those from all type wells (blue). (B) In a non-stationary reservoir, the statistics of well logs from a test well are normalized to match those of nearby type well(s) that have similar statistics.

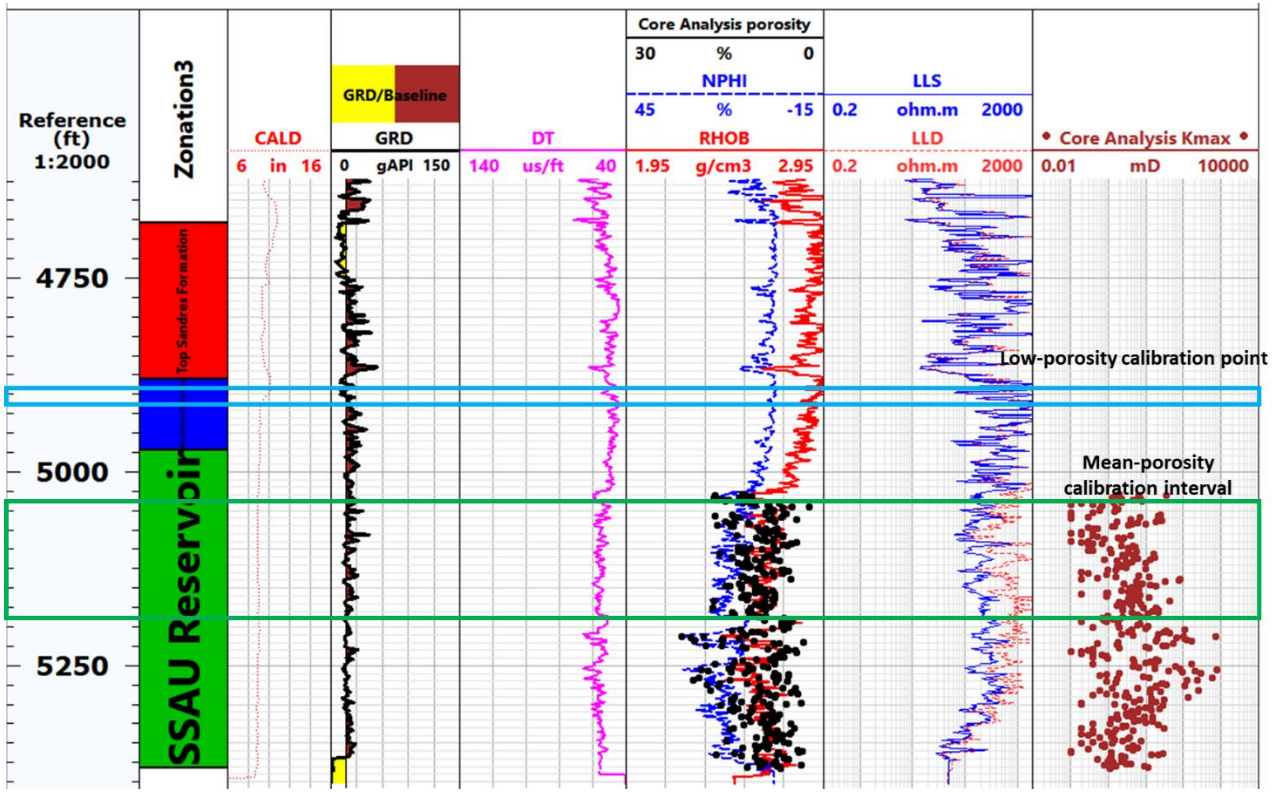

Figure 2.3: Input well logs and core data for quality control and workflow validation. There are three zones in this interval (Zonation, track 2), and we are interested in predicting the permeability (Core Analysis Kmax) of the "SSAU Reservoir" production zone using the caliper log (CALD), gamma-ray log (GRD), sonic log (DT), neutron (NPHI) and density (RHOB) porosity logs and resistivity logs (laterolog LLD, LLS). Conventionally, well logs are normalized with the two-point scaling method to reproduce the univariate statistics of well logs from the type wells. One endpoint is chosen from the anhydrite/dolomite interval (blue) overlaying the production zone (green) while the remaining endpoint is selected from the dolomite facies in the production zone (green).

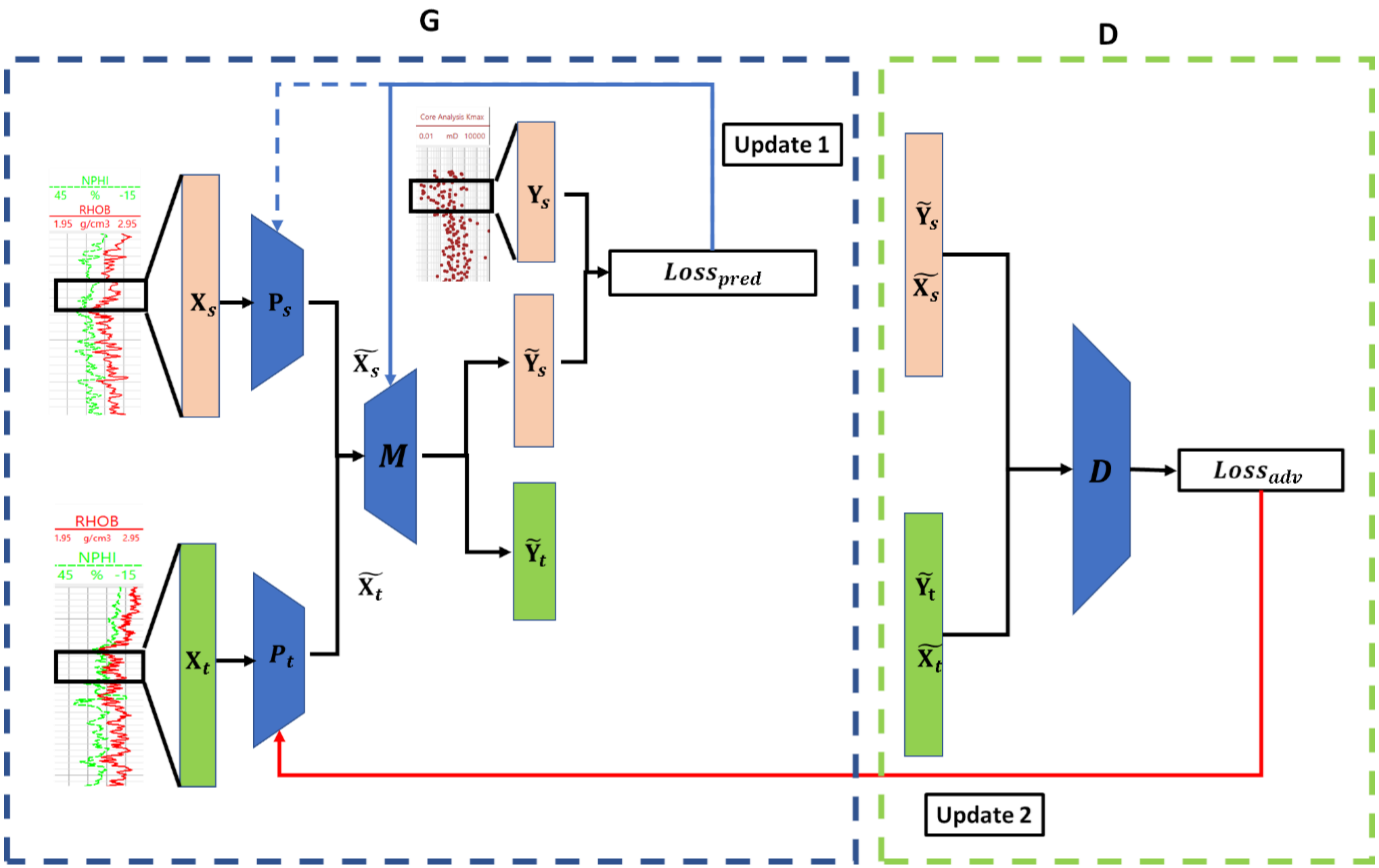

Figure 2.4: Structure of the Discriminative Adversarial (DA) model. MSE loss function and adversarial loss function are optimized asynchronously through update 1 (blue line) and update 2 (red line) respectively. P_s is an identical mapping and not updated, unless intermediate features instead of well logs are deemed to be stationary (blue, dash line).

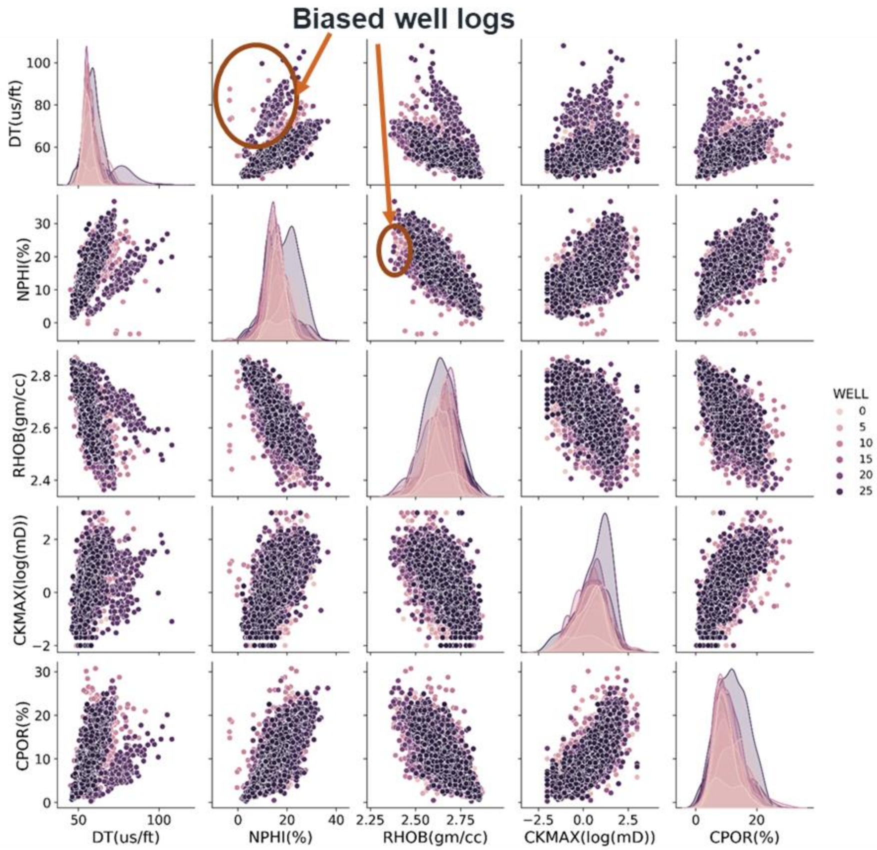

Figure 2.5: Histograms and pair-wise scatter plots of sonic (DT), neutron (NPHI), density (RHOB), core permeability (CKMAX), and core porosity (CPOR) logs of all 30 wells. Each color in histograms and scatter plots represents data from a well, the well number is listed every five wells in the legend. Biased well logs are identified with red circles.

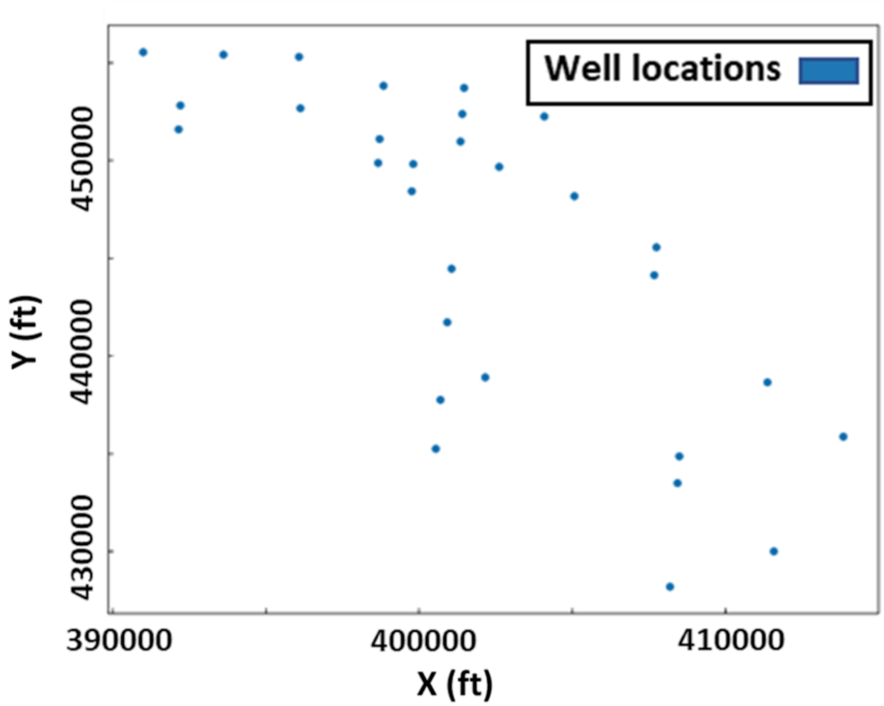

Figure 2.6: Wellhead locations of 30 wells (blue) at SSAU. Core measurements and well logs are available for these wells to calibrate and validate different models.

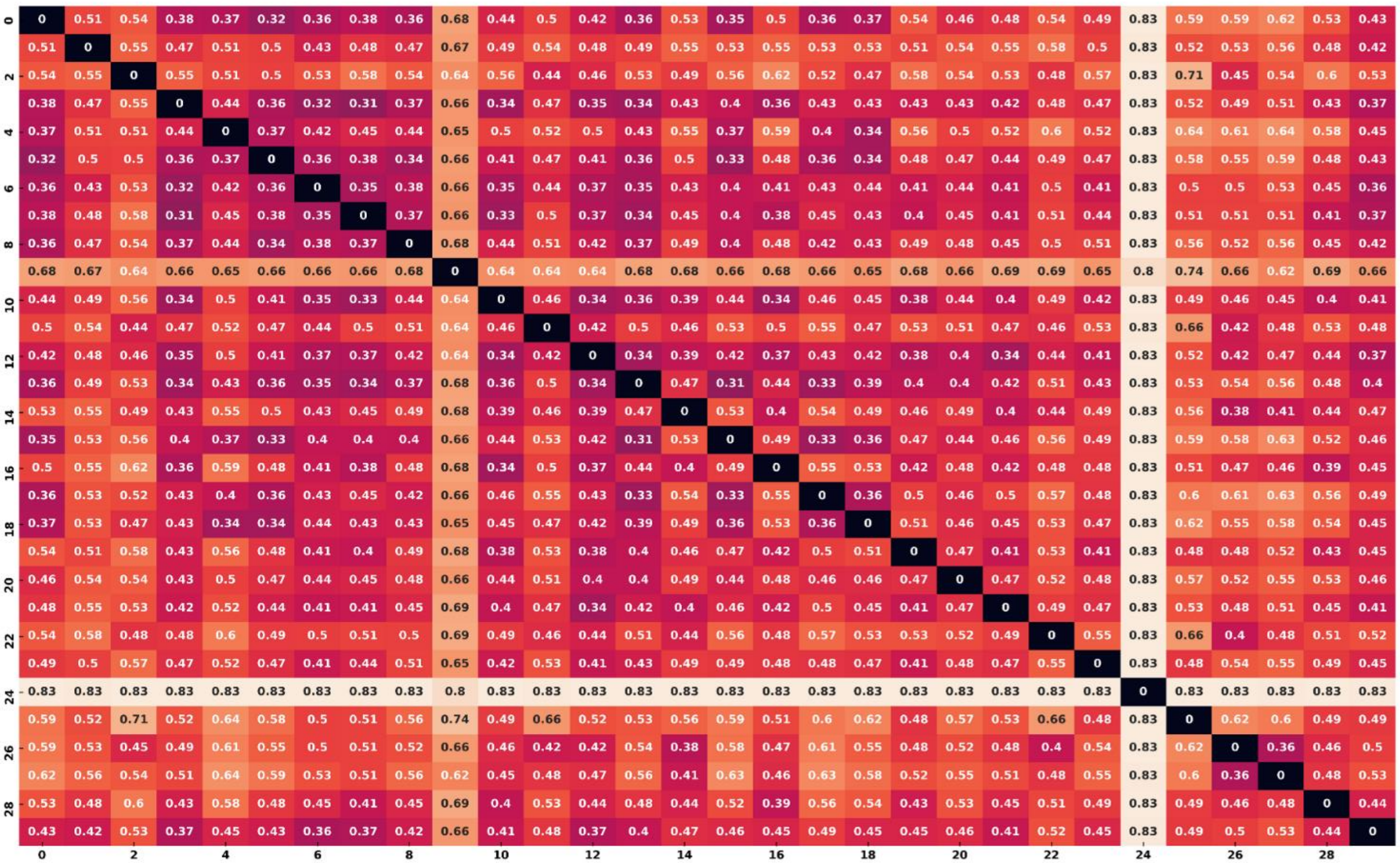

Figure 2.7: Statistical distance matrix representing the well-log divergence between any pair of wells. The statistical distance between a pair of wells is calculated as the divergence of the well-log joint distribution between the wells, a high value indicates different well-log distribution of a pair of wells, and vice versa.

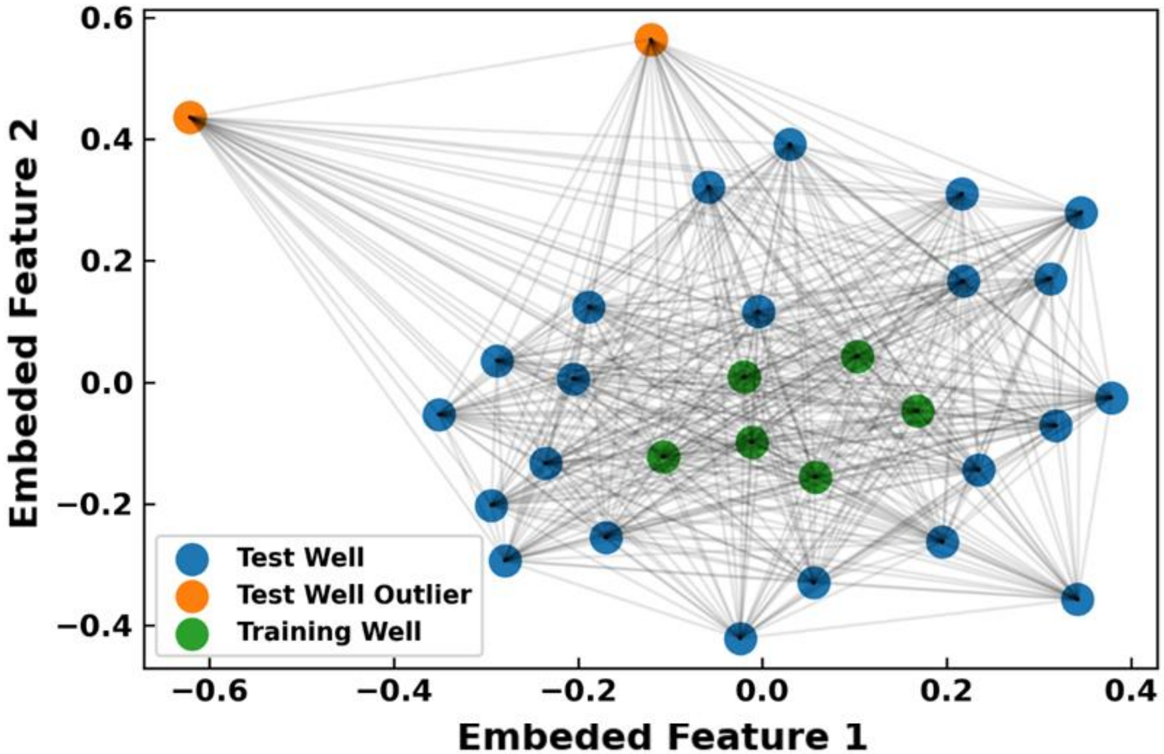

Figure 2.8: MDS map calculated based on the statistical distance of all wells. Test wells (blue) and training wells (green) are statistically similar, while outlier test wells (orange) are statistically different from the other wells; lengths of lines between wells represent their pair-wise statistical distances on the two-dimensional MDS feature space.

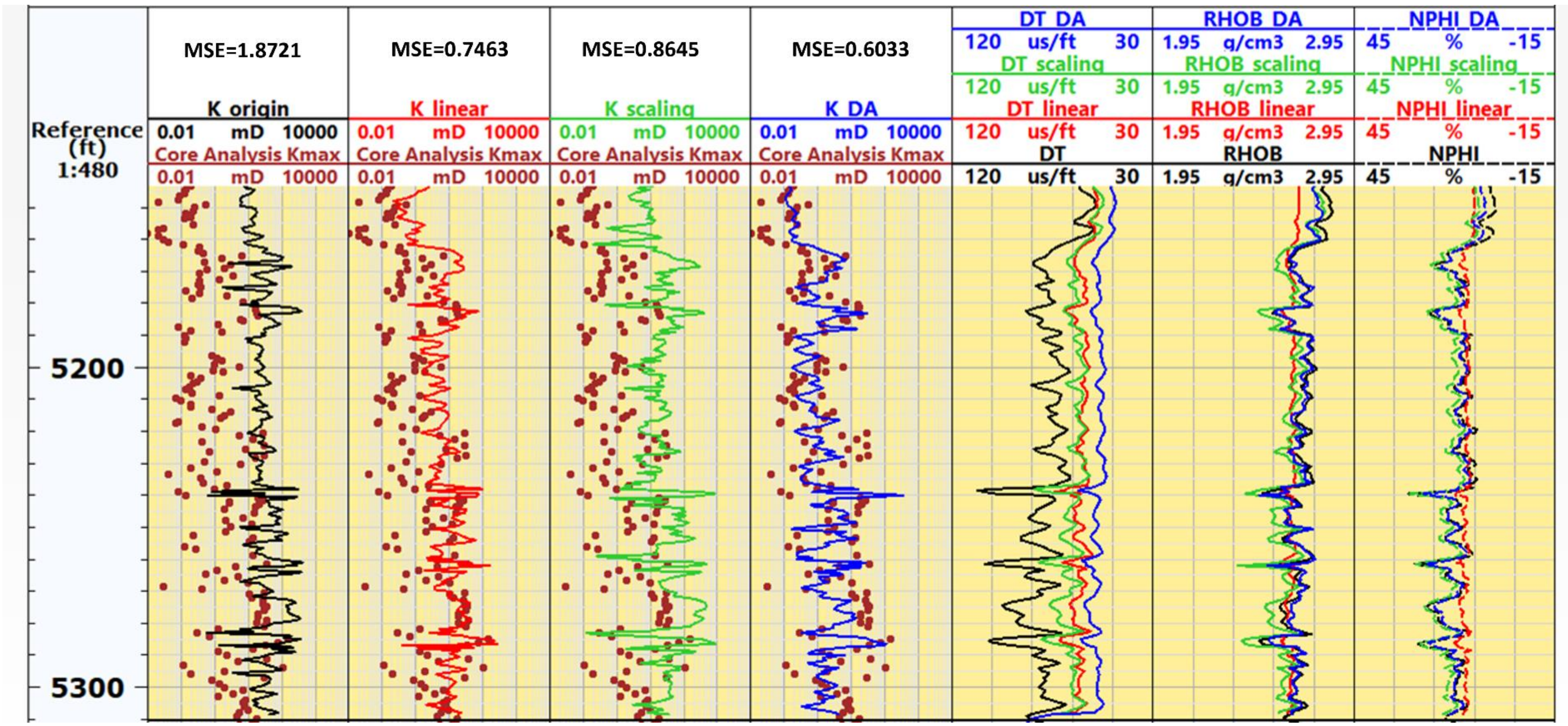

Figure 2.9: Permeability predictions and normalized well logs of the outlier well No. 24 based on 6 stationary training wells. Comparison of results obtained with the unconstrained model (black with suffix "_origin"), linearly constrained model (red with suffix "_linear"), two-point scaling normalized model (green with the suffix "scaling"), and DA model (blue with the suffix "_DA"). The first four tracks show the actual (brown dots) and predicted permeability (line), and the MSE of permeability prediction is shown at the header of each track. The next three tracks show the original (black) and normalized sonic (DT), density (RHOB), and neutron (NPHI) well logs.

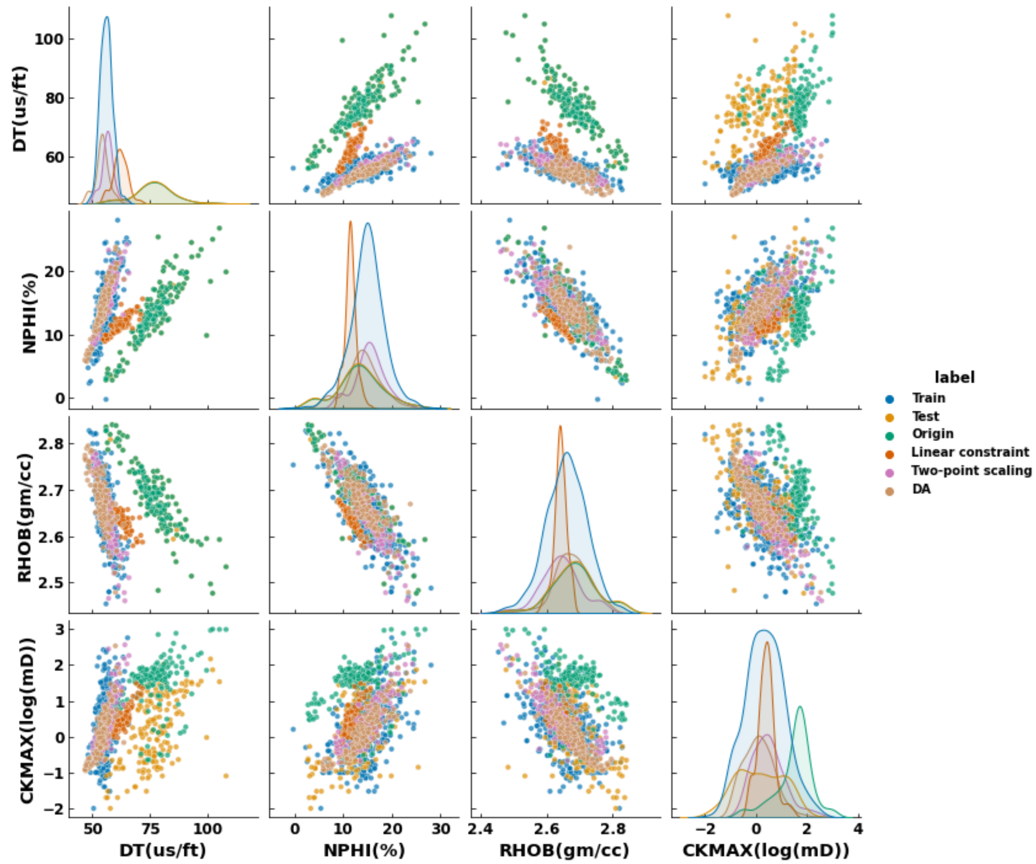

Figure 2.10: Cross-plots and histograms of normalized well logs and permeability of outlier test well No. 24. The distribution of well logs and permeability measurements of the test well (orange, “Test”), of the training wells (blue. “train”), and well logs and permeability prediction calculated without well-log normalization (green, “Origin”), calculated with linear constraint method (red, “Linear constraint”), calculated with the two-point scaling method (pink, “Two-point scaling”) and calculated with the DA method (brown, “DA”) are compared.

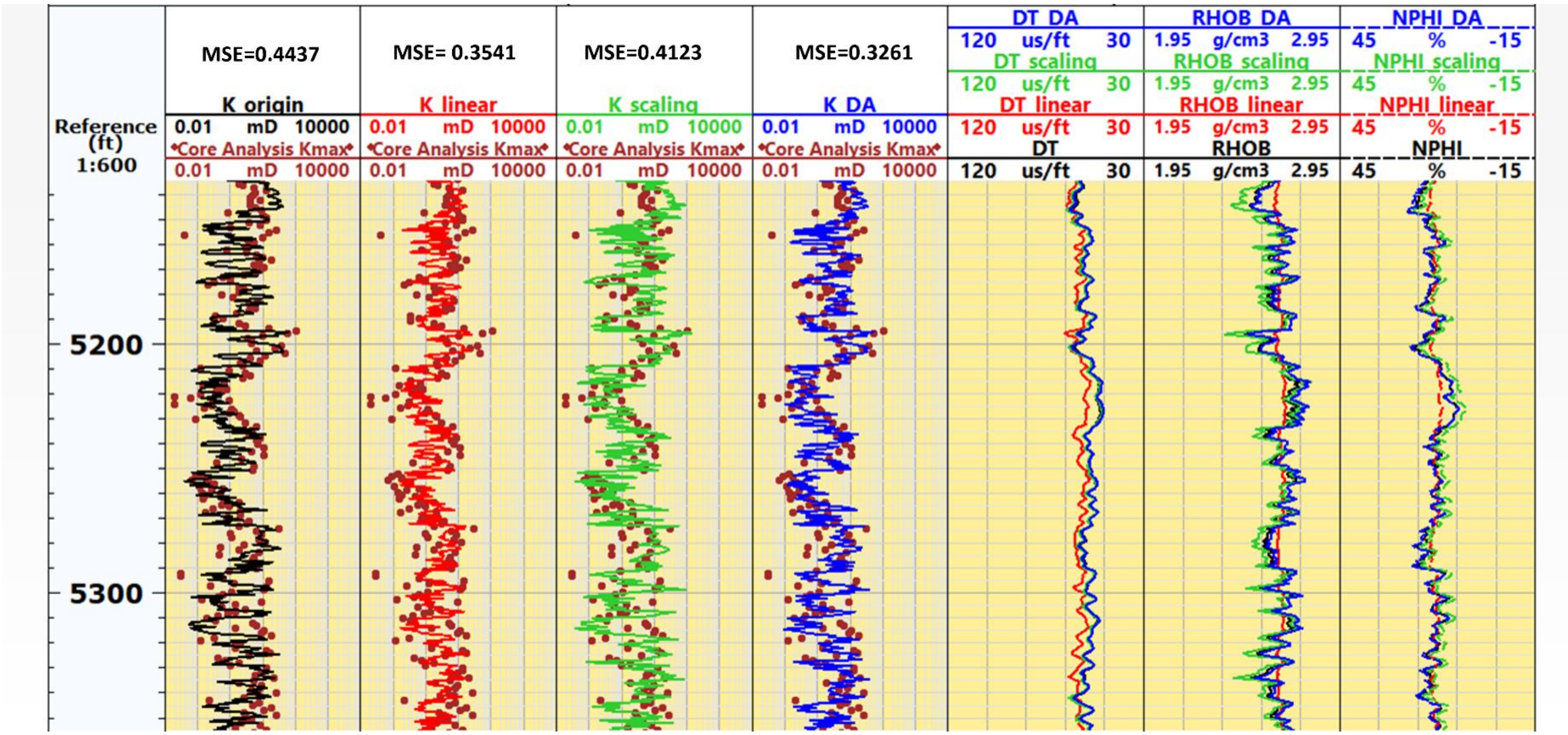

Figure 2.11: Normalized well logs and permeability predictions of a non-outlier test well No. 0. Comparison of results obtained with the unconstrained model (black with suffix "_origin"), linearly constrained model (red with suffix "_linear"), two-point scaling normalized model (green with the suffix "scaling"), and DA model (blue with the suffix "_DA"). The first four tracks show the actual (brown dots) and predicted permeability (line), and the MSE of permeability prediction is shown at the header of each track. The next three tracks show the original (black) and normalized sonic (DT), density (RHOB) and neutron (NPHI) well logs.

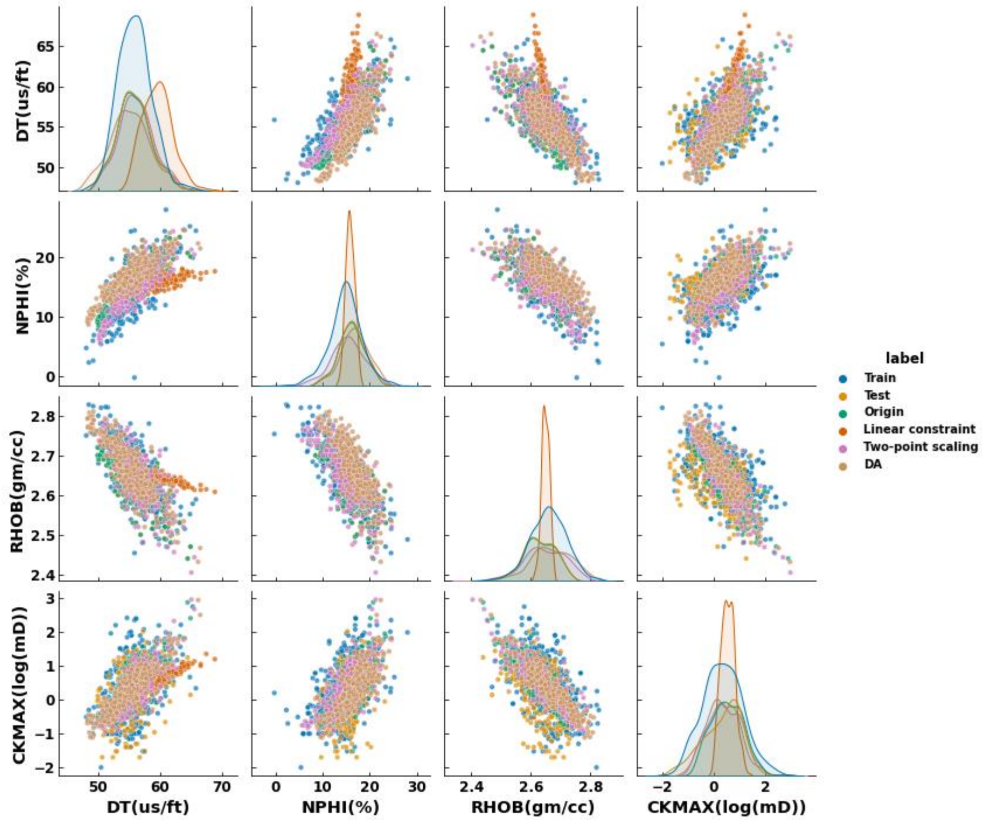

Figure 2.12: Cross-plots and histograms of normalized well logs and permeability predictions obtained from a non-outlier test well No. 0. The distribution of well logs and permeability measurements of the test well (orange, "Test"), of the training wells (blue. "train"), and well logs and permeability prediction calculated without well-log normalization (green, "Origin"), calculated with linear constraint method (red, "Linear constraint"), calculated with the two-point scaling method (pink, "Two-point scaling") and calculated with the DA method (brown, "DA") are compared.

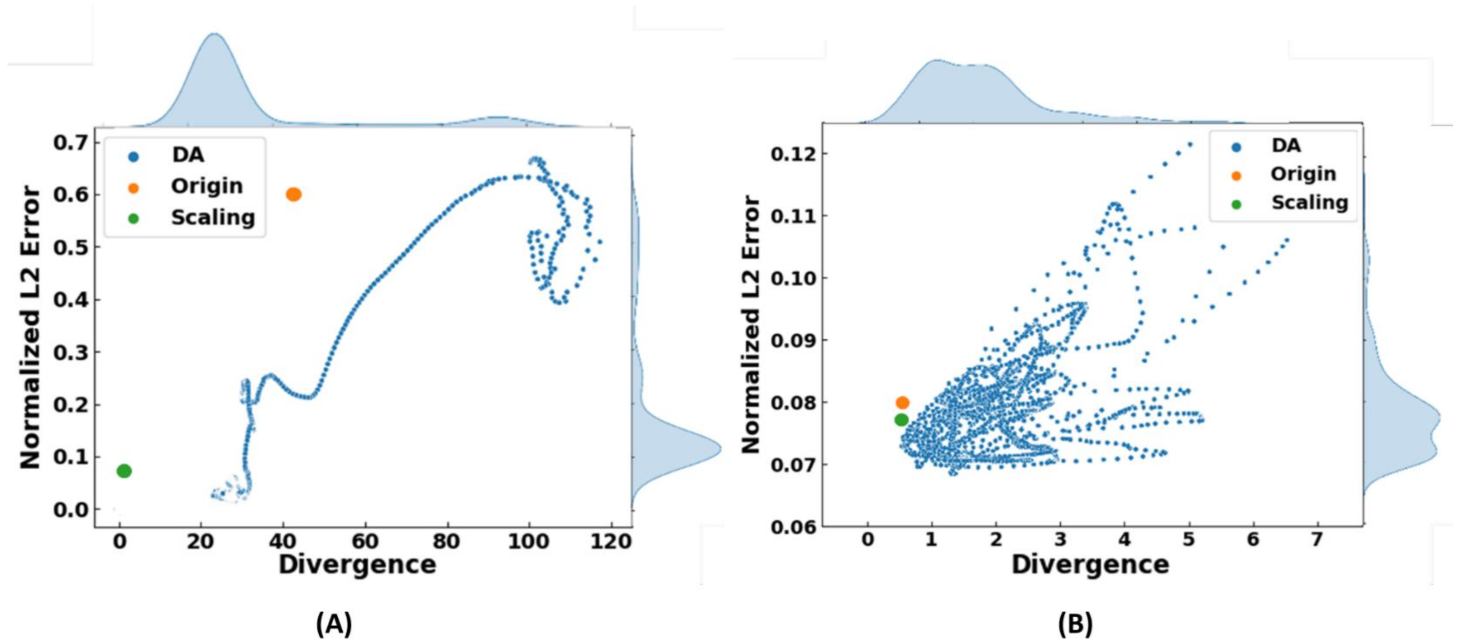

Figure 2.13: The divergence vs. the MSE of permeability prediction from 3 constrained models at different training epochs for outlier test well No. 24 (A) and non-outlier well No. 0 (B). A lower divergence indicates that the normalized well logs better reproduce the distribution of training well logs. Training of all three constrained models decreases the divergence and better predicts the permeability. The DA model at its lowest divergence point (blue) has the lowest error, followed by the two-point scaling method (red) and the original model (yellow). Also, the two-point scaling method may have lower divergence than the DA model (A) due to over alignment. The DA model training is an iterative optimization process: the error does not monotonically decrease or increase; instead, the model normalizes well logs and makes predictions to explore the solution space iteratively, guided by discriminators optimized at different epochs, where the optimal output can be determined as the point with the lowest divergence.

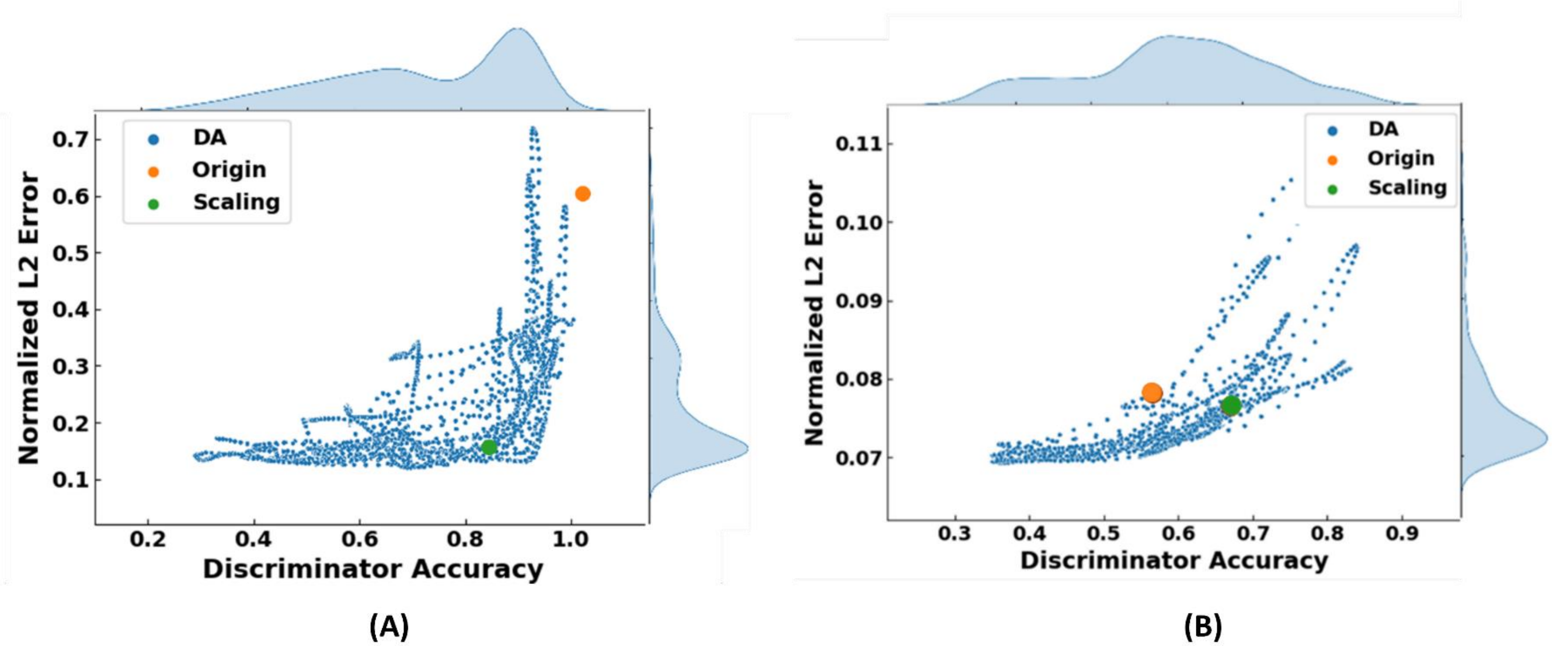

Figure 2.14: Accuracy of the discriminator vs. the MSE of permeability predictions at different training epochs of three constrained models for an outlier test well (A) and a non-outlier test well (B). Permeability calculated with the DA method (blue) has the lowest prediction error, followed by the two-point scaling method (red) and the original model (yellow). The DA method has the lowest discriminator accuracy. The DA model training is an iterative process, where the discriminator accuracy oscillates between 0 and 1 during the training, and the optimal output can be determined as the training epoch with the lowest discriminator accuracy at a late training stage.

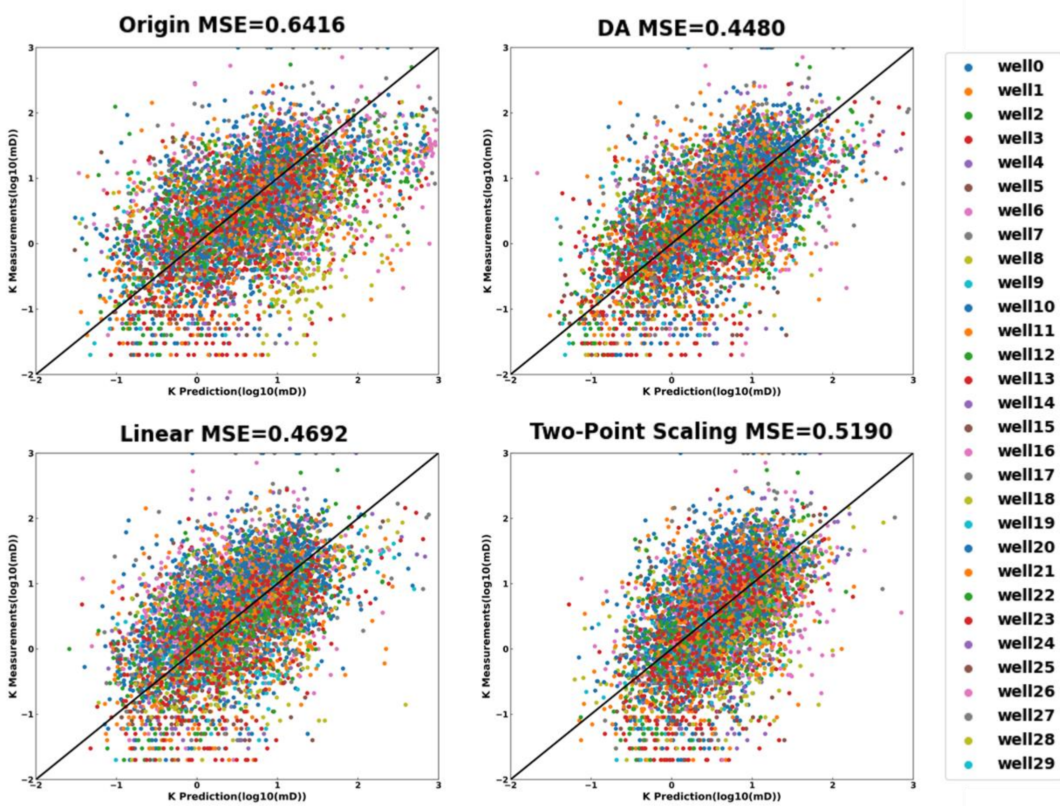

Figure 2.15: Accuracy of the discriminator vs. the MSE of permeability predictions at different training epochs of three constrained models for an outlier test well (A) and a non-outlier test well (B). Permeability calculated with the DA method (blue) has the lowest prediction error, followed by the two-point scaling method (red) and the original model (yellow). The DA method has the lowest discriminator accuracy. The DA model training is an iterative process, where the discriminator accuracy oscillates between 0 and 1 during the training, and the optimal output can be determined as the training epoch with the lowest discriminator accuracy at a late training stage.

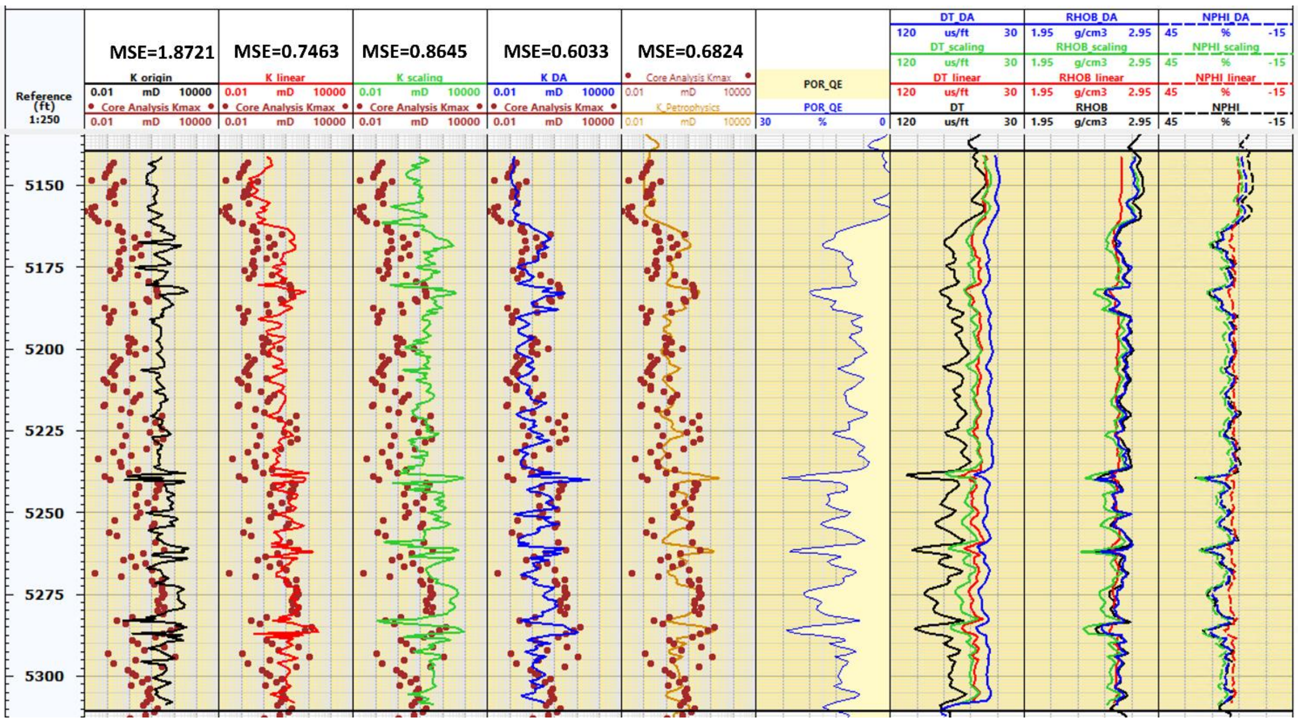

Figure 2.16: Permeability predictions and normalized well logs of the outlier well No. 24 based on 6 stationary training wells. Comparison of results obtained with the unconstrained model (black with suffix "_origin"), linearly constrained model (red with suffix "_linear"), two-point scaling normalized model (green with the suffix "scaling"), DA model (blue with the suffix "_DA"), and petrophysical model (orange with suffix "_Petrophysics"). The first five tracks show the actual (brown dots) and predicted permeability (line), and the MSE of permeability prediction is shown at the header of each track. The sixth track shows the porosity prediction from multimineral analysis.The last three tracks show the original (black) and normalized sonic (DT), density (RHOB), and neutron (NPHI) well logs. The petrophysical model is robust to abnormal sonic log due to the high uncertainty assigned to the sonic log.

Chapter 3: Conditional Simulation of Fluvial Channel Reservoir with the Stochastic Pix2pix Method

Constructing subsurface models that accurately reproduce geological heterogeneity and their associated uncertainty is critical to many geoscience and engineering applications. For hydrocarbon reservoir modeling and forecasting, for example, spatial variability must be consistent with geological processes, geophysical measurements, and time records of fluid production measurements. Generating such subsurface models can be time-consuming; conditioning them to different types of measurements is even more computationally intensive and technically challenging. Using too many free variables can cause overfitting of the data, thereby decreasing the predictive ability of the model; high dimensionality also slows convergence during history-matching of fluid production measurements. To contend with these problems, I introduce a new machine learning approach, referred to as the stochastic pix2pix method, which parameterizes high-dimensional, stochastic reservoir models into low-dimensional Gaussian random variables in latent space.

Many of the world's significant hydrocarbon fields originate from fluvial or turbidite deposits, with sedimentary processes and spatial distribution of rock facies significantly influencing their flow behavior. Rule- or object-based methods are commonly used to geostatistically model these types of reservoirs. I introduce a new and efficient machine learning-based reservoir modeling workflow capable of generating 2D fluvial reservoir models that account for the available field data and the geometries of different facies. By constraining subsurface model realizations to available geophysical and petrophysical interpretations, multi-physics inversion can be greatly accelerated thereby, requiring only production history matching. Although my models are 2D, an extension to

3D can be readily implemented through reservoir-unit modeling and conditioning. The proposed method and workflow also partially solve the common problem of machine learning methods, wherein mapping low- to high-resolution images often yields reduced spatial variability.

The proposed method is an extension of conditional generative adversarial networks (CGAN), in which I incorporate a novel penalty term into the loss function to generate various realizations honoring the same conditional data, such as structural interpretation from seismic data, and borehole measurements at key well locations. I "train" the generative model on geologically realistic, multivariate spatial models generated with a rule-based fluvial reservoir simulator. Each high-resolution training image includes 5 lithofacies with distinct petrophysical property trends. To evaluate the performance of the proposed method, visual inspection and indicator variograms are applied to gauge how well the realizations reproduce existing patterns in the true model. A new metric, the mean categorical error, is proposed to quantify how well the realizations match the conditioning data.

The new method reproduces seismic amplitude data with 99.69% accuracy and borehole measurements with 93.3% accuracy in synthetic examples. Spatial heterogeneity is verified with visual inspection and two-point statistics: it is found that spatial patterns and indicator variograms from the training images for all facies are reproduced well. The proposed method correctly reproduces patterns even when the conditioning data are significantly different from those in the training set. Likewise, the method can perform continuous model modifications, meaning that the machine learning procedure effectively reproduces the migration rule of a meandering (fluvial) system.

3.1 INTRODUCTION

Generating an ensemble of reservoir models that accurately predicts the range of possible subsurface flow behavior is critical for hydrocarbon reservoir management, risk analysis, and development decision-making. Such reservoir models are often generated with geostatistics-based stochastic modeling methods that incorporate all available field measurements, such as well logs, seismic interpretation data, and time records of fluid production measurements.

Fluvial and deep-water reservoirs are two of the world's most important types of hydrocarbon reservoirs (Swanson, 1993). High-quality clastic rocks in these reservoirs are capable of storing huge amounts of hydrocarbon and water. Building reservoir models that accurately characterize the distribution of these rocks is therefore of great importance for optimum reservoir development decision-making. However, because the spatial distribution of reservoir rocks is associated with the depositional process, each facies in a fluvial reservoir often demonstrate unique architectural geometries, this complicates accurate reservoir modeling (Onesti & Miller, 1974; Ferguson et al., 2001; Zhang et al., 2005; Guin et al., 2010; Ramanathan et al., 2010). It is common practice to perform reservoir modeling and conditioning via two-point geostatistical methods, but the nonlinear and non-stationary property distribution in fluvial reservoirs limits the accuracy of variogram-based approaches without an extreme level of deterministic constraints (Cressie & Hawkins, 1980; Cressie, 1985; Warrick & Myers, 1987; Deutsch & Journel, 1992; Williams, 1998; Gringarten & Deutsch, 2001; Pyrcz & Deutsch, 2014).

Many multi-point simulation (MPS) methods have been developed to generate models reproducing the nonlinear ordering relationships and non-stationary property distributions pertinent to fluvial reservoirs (Strebelle & Journel, 2001; Caers, 2003; Boisvert et al., 2006; Boisvert et al., 2007; Hu & Chugunova, 2008; Pyrcz et al., 2008;

Boisvert et al., 2010; Mariethoz et al., 2010; Pyrcz et al., 2012; Mariethoz & Caers, 2014). MPS methods use multiple-point templates to extract patterns from exhaustive, analog reservoir models. Patterns are stored as a large set of conditional probabilities, which are then applied in the sequential simulation paradigm to generate reservoir models. Training images are commonly derived from object-based or rule-based models, with the expectation that the generated reservoir models will reproduce the patterns present in the training images. However, MPS methods often fail to reproduce the long-range patterns of the training image; in particular, the bias of reduced connectivity resulting from, e.g., broken channels, remains an unsolved problem for MPS methods. To capture large-scale features, a large training image and a large template are required, but the limits in computer memory and computational time prohibit a large template to be used.

Object-based methods have been developed to reproduce certain long-range patterns. These methods model facies as parameterized architectural geometries, which are then incorporated into the reservoir model by enforcing constraints such as data conditioning, global proportions, and locally variable proportions (Haldorsen & Lake, 1984; Deutsch & Wang, 1996; Holden et al., 1998; Hu & Jenni, 2005; Hassanpour et al., 2013). Other rule- and surface-based methods have been developed to better account for sedimentary dynamics, wherein reservoir models are generated sequentially according to sedimentary dynamics-based rules (Øren & Bakke, 2002; Pyrcz et al., 2005; Zhang et al., 2009; Pyrcz et al., 2012; Pyrcz et al., 2015). However, both object- and rule-based methods face an important technical challenge, which is that some of the model parameters are integers and not differentiable. Non-differentiable variables complicate reservoir model conditioning and model parameterization (Pyrcz & Deutsch, 2005; Zhang et al., 2009; Boisvert & Pyrcz, 2014; Alpak et al., 2017; Wang et al., 2018). This is especially the case with the rule-based reservoir model because each geological object is generated as a random process and conditioned upon previously simulated objects, thereby resulting in large-scale emergent features (Pyrcz et al., 2014).

The ensemble of reservoir models currently available to researchers is based on a large suite of parameters and random processes. With current geostatistical approaches, it is difficult to provide more compact parameterization for fluvial reservoirs because of the large number of objects (Oliver et al., 2008). In turn, the large number of parameters in any given model poses problems for both history matching and static conditioning.

Model dimensionality reduction is thus important for all kinds of subsurface inverse problems, and researchers have achieved success with different methods for reservoir model reduction (Laloy et al., 2015; Asher et al., 2015; Li et al., 2016; Laloy et al., 2017; Jin et al., 2019; Mo et al., 2019). In recent years, a new machine learning method referred to as GAN has been developed to parameterize high-dimensional reservoir models to a low-dimensional latent space (Goodfellow et al., 2014). Latent space is a hidden space effectively created by this parameterization. Its dimension is equal to the number of reduced model parameters. GAN consists of two deep convolutional neural networks (CNN) (Hansen & Salamon, 1990; Specht, 1991; LeCun et al., 1998; Yosinski et al., 2014), called generator and discriminator neural networks. The GAN is used to stochastically generate new images which show the same patterns as the images used for training. Researchers have investigated conditional and unconditional fluvial reservoir models generated using different types of GANs, and some of their work shows promising results (Chan & Elsheikh, 2017; Dupont et al., 2018; Laloy et al., 2018; Zhang et al., 2019; Jo et al., 2019). Likewise, GANs have proven to be efficient for reservoir model parameterization and model reduction. Chan & Elsheikh (2017) used Wasserstein GAN (Arjovsky et al., 2017) to generate permeability fields for fluid flow simulation. Laloy et al. (2018) generated unconditional reservoir models from hand-drawn training images using the spatial GAN; the models are then used as *a priori* models in Markov Chain Monte Carlo sampling methods (MCMC) for history matching. Single-phase fluid flow inverse problems have been successfully solved using the latter method. To condition reservoir models to static well-log data, Dupont et al. (2018) added facies mismatch at well locations to the loss function and applied a sampling method to generate conditional realizations. It should be noted, however, that in Dupont et al. (2018) the geometries of different facies in the training images were relatively simple. Jo et al. (2019) increased model complexity by using rule-based models as training images; well data conditioning was performed by inpainting the areas near well locations. However, because only well data were used to constrain the realizations, the inpainting method could result in artifacts near wells. Finally, in all of the above papers, "mode collapse" is a common problem during training. Mode collapse means that models generated by GAN are similar to each other, thus only simple geometries have been learned during training.

In my effort to produce reservoir models mimicking the sedimentary process of channel systems, I generate training images using the rule-based reservoir modeling method. The training images have up to five facies with distinct geometries and inter-facies spatial relationships. I also require that the reservoir models not only honor the well-log data, but also the seismic data. Given so many conditioning constraints, it is difficult to use sampling methods to perform the conditioning; the number of constraints also makes it difficult to parameterize the posterior distribution and use it as the *a priori* distribution for other inversion calculations, e.g., production history matching. Therefore, I developed a new generative method, the stochastic pix2pix method, to generate reservoir model realizations to honor well logs and seismic interpretations and to parameterize reservoir models to low-dimensional Gaussian space. It is based on the pix2pix method (Isola et al., 2017), which is built upon conditional generative adversarial networks (CGAN) (Mirza &

Osindero, 2014). CGAN generates diverse realizations given constraints such as labels and categories. However, as noted by Isola et al. (2017), CGAN and pix2pix methods cannot generate realizations that vary significantly given the same complex conditioning data. The new loss function in the proposed stochastic pix2pix method makes it possible to stochastically generate significantly different reservoir models conditional to the same complex constraints. The stochastic pix2pix method reproduces both the long- and short-range patterns observed in the training images. The resulting models honor well data and large-scale seismic constraints, and they are consistent with geological knowledge. The workflow may also be used to generate reservoir models conditioned to well locations, and well and seismic data, or as downscaling seismic data while honoring well constraints.

The machine learning-based subsurface modeling method can be applied to a variety of subsurface modeling problems, such as oil or water reservoir modeling, for instance, the stochastic pix2pix method can build better reservoir models which not only reproduce complex geological patterns, but also efficiently incorporate geophysical and petrophysical interpretations. Well parameterized latent space variables can be used as a good *a priori* distribution for efficient history matching. The proposed workflow can greatly help reservoir management and decision-making in fluvial or turbidite reservoirs.

3.2 METHOD

3.2.1 A Review of the Pix2pix Method

The stochastic pix2pix method is an extension of the pix2pix method developed by Isola et al. (2017). pix2pix is a CGAN with one additional L1-norm loss term (Eq. 3.1). CGAN is a GAN conditioned to labels and other *a priori* knowledge about the training image. All generative models are used to learn patterns from the training images, such as the shape of objects, relative positions of different objects, and the trend within each object, to generate realizations reproducing these patterns. For common reservoir modeling applications, training images can be rule-based reservoir models, object-based reservoir models, hand-drawn conceptual reservoir models, outcrop photographs, physics-based geologic process models, flume experiments, or shallow seismic interpretation. Generated models are stochastic subsurface reservoir models.

In the GAN approach, there are two neural networks (NNs), which are generator (G) and discriminator (D). While the generator attempts to produce more realistic models from low-dimensional random variables, the discriminator learns to identify the fake reservoir model realizations (y) obtained from the training images. They compete constantly until the generator yields reservoir models similar to training images, effectively fooling the discriminator. The neural network used in the generator is a special CNN structure called U-Net (Ronneberger et al., 2015), while the discriminator consists of a series of CNNs. I use CNNs for both generator and discriminator because CNNs are proven efficient tools for automatic pattern extraction (O'Shea & Nash, 2015). Compared to conventional CNNs, U-Net uses less computational memory and can transfer local patterns from the conditioning image to the realizations, enhancing the reproduction of local patterns (Ronneberge et al., 2015).

In CGAN, the input and loss functions are different from GAN. While the generators (G) in GANs learn to map from only random variables, z, in the latent space to realizations y: y=G(z), the generator (G) in CGAN learns to map from both random variables and conditioning data, x, to realizations: y= G (x, z). The latent space is a low-dimensional space that high-dimensional training images can map to, thus we can expect to generate conditional, stochastic reservoir models by simply changing the parameters in latent space. The discriminator (D) in CGAN not only is responsible for distinguishing the generated models from the training images, but also verifies that the models are consistent with the conditioning data. In reservoir modeling, the conditioning data can be the low-resolution seismic inversion and interpretation, well-log interpretation, or prior knowledge about the reservoir architecture (e.g., channel and levee width).

Compared to CGAN, the pix2pix method adds the L1-norm of the difference between the generated models and actual models over all pixels to the loss function (see Eq. 3.1). The additional L1-norm enhances the resolution of generated models and encourages the exact reproduction of the training images.

The additional L1-norm loss term and the loss function of the pix2pix method are expressed as:

$$\mathcal{L}_{L1}(G) = \mathbb{E}_{x,y,z}[\|y_{train} - G(x,z)\|_1] \tag{3.1}$$

$$\mathcal{L}_{CGAN}(G,D) = \mathbb{E}_y[logD(y)] + \mathbb{E}_{x,z}\big[\log\big(1 - D(G(x,z))\big)\big] \tag{3.2}$$

$$\mathcal{L}_{pix2pix} = arg \min_G \max_D \mathcal{L}_{CGAN}(G,D) + \lambda\mathcal{L}_{L1}(G) \tag{3.3}$$

Where x are the conditioning data, z are random variables in latent space, $G(x,z)$ and y are generated models, y_{train} are training images, D is the discriminator and G is the generator, λ is the certainty coefficient of the L1-norm, $\mathcal{L}_{CGAN}$ is the loss function of CGAN, and $\mathcal{L}_{pix2pix}$ is the total loss function.

Specifically, in property modeling, $\mathcal{L}_{L1}(G)$ represents the L1 norm of the differences between the generated reservoir property models, such as porosity models, and the training images over all pixels. In facies modeling, $\mathcal{L}_{L1}(G)$ is the L1 norm of the binary correctness map over all pixels. The value at each point of the binary correctness map equals 0 if the facies at that point in both the realization and the training image are the same; otherwise, it equals 1.

$\mathcal{L}_{CGAN}(x, z)$ is the loss function of a CGAN, which is a binary cross-entropy loss function in facies modeling. $\mathbb{E}_y[logD(y)]$ is the logarithmic probability that the discriminator decides whether a training image originates from the training image set. $\mathbb{E}_{x,z}\left[\log\left(1 - D(G(x, z))\right)\right]$ is the logarithmic probability that the discriminator decides whether a generated reservoir model does not originate from the training image set.

In Eq. 3.3, $\mathcal{L}_{pix2pix}$ is the total loss function, and $arg \min_G \max_D \mathcal{L}_{CGAN}(G, D)$ represents the process of finding parameters (arg) for (1) the generator to minimize $(\min_G)$ the probability that the discriminator successfully distinguishes the generated reservoir models from training images, and (2) the process of finding parameters for the discriminator to maximize $(\max_D)$ the probability that the discriminator can successfully distinguish the generated reservoir models from training images. The generator and discriminator compete constantly until Nash equilibrium is reached (Myerson, 1978) and the generator can generate realizations reproducing the patterns in the training images.

One problem with pix2pix, as noted by Isola et al. (2017), is that the images generated with it do not show much variability. Two factors cause the lack of variability in results obtained with the pix2pix method: (1) the L1-norm term tends to cause overfitting to the training image, and (2) inputting conditioning images into the discriminator decreases the variety of patterns in the ensuing realizations.

3.2.2 Stochastic Pix2pix for Diverse Reservoir Model Generation

To alleviate the limitations of pix2pix, I develop the stochastic pix2pix method. In this method, I first back-calculate the conditioning data from the generated reservoir models, and then use the mean squared error (MSE) between the target conditioning data and back-calculated conditioning data as an additional loss term to enforce the conditioning. The loss function can be expressed as

$$\mathcal{L}_{L2_{sto}}(G) = E_z[\|x_{train} - G^{-1}(G(x_{train}, z))\|_2] \tag{3.4}$$

$$\mathcal{L}_{\ sto}(x, z) = arg \min_G \max_D \mathcal{L}_{CGAN}(G, D) + \lambda \mathcal{L}_{L2_{sto}}(G) \tag{3.5}$$

where x_{train} are the target conditioning data, z are random variables in latent space, $G(x_{train}, z)$ are generated models, G^{-1} is the back calculator, D is the discriminator and G is the generator, λ is the certainty coefficient of additional L2-norm loss term, $\mathcal{L}_{L2_{sto}}$ is the L2-norm of conditioning data mismatch, $\mathcal{L}_{\ sto}(x, z)$ is the total loss function, and $\mathcal{L}_{CGAN}$ is the loss function of a CGAN.

More specifically, $G^{-1}(G(x_{train}, z))$ is the inverse process of mapping the generated or training reservoir models back to the target conditioning data (e.g., seismic, well-log interpretations maps), x_{train} , using simple arithmetic operations. $\mathcal{L}_{L2_{sto}}(G)$ is the L2-norm of the difference between back-calculated conditioning data and the actual conditional data; and $arg \min_G \max_D \mathcal{L}_{CGAN}(G, D)$ is the process (arg) of finding both parameters for the generator G to minimize the probability of correct classification $(\min_G)$ and parameters for the discriminator D to maximize the probability of correct classification $(\max_D)$. λ represents how certain we are about the conditioning data. The additional MSE term $\mathcal{L}_{L2_{sto}}(G)$ in the total loss function is included to avoid generated models converging to a simple mode; λ controls how well the generated models reproduce the conditioning data. When λ is small, the stochastic pix2pix method defaults to CGAN, and tends to reproduce only common patterns in training images while ignoring the conditioning data; on the other hand, when λ is large, the method tends to perfectly reproduce the conditioning data, thereby decreasing the variability of realizations. The patterns in the training images are not well reproduced in the realizations when λ is above 10000.

By incorporating only the mismatch of conditioning data as an additional loss term into the loss function, we avoid the overfitting problem in the pix2pix method. The generator of the stochastic pix2pix model is a U-net, which outputs the realizations and the back-calculated conditioning images (see Figure 3.1); the discriminator is a series of CNNs, which output the probability of the input image being a training image (Figure 3.2).

It is worth noting that the structure of my algorithm is similar to the cycle-consistent adversarial networks (CycleGAN) method (Zhu et al., 2017), but with CycleGAN the G^{-1} operator is effectively another generative adversarial network because the images are unpaired. Nevertheless, the neural network can be easily fooled (Nguyen et al., 2015), which may cause the lack of variability seen with CycleGAN. Therefore, in my proposed method, I use simple arithmetic operations to back-transform the generated models into conditioning models. Random variables, z, are also added to the input of the generator to ensure the variation of generated models.

Unlike the pix2pix method, where realizations, training images, and conditioning data are all inputs for the discriminator, in the stochastic pix2pix I only use generated models and training images as the input for the discriminator. I do this because the patterns of architectural element distribution (geological settings) are stationary among all training images, i.e., the same rule-based reservoir modeling simulator is used to generate the training images.

There are 3 main differences between the classical and the new methods:

1) I did not use the reconstruction loss (L-1 loss term) to enforce exact reproduction.
2) I did not input conditioning data to the discriminator because I assume the patterns are stationary among all training images.

3) I add loss terms to force the realizations to honor the conditioning data.

By making these modifications, I successfully generate diverse realizations by only changing the latent variables.

3.2.3 Markov Chain Monte Carlo (MCMC) Method for Globally Optimum Models Search

The generation of diverse models requires that the certainty coefficient, λ, not be set too large. To find the optimal match between models and the well logs and seismic interpretation, we can use the MCMC method, Metropolis-Hastings (M-H) sampling to assess the realizations. Although other sampling methods can be used, MCMC gives the most accurate *a posteriori* distribution. The workflow can be summarized as follows:

1) $x_t \sim f(x)$, initialize input $x_{t=0}$ as a combination of (1) 100 random variables (z) in latent space, and (2) conditioning data, such as channel widths, levee widths, and avulsion rate according to *a priori* distribution $f(x)$.
2) For t< $T_{threshold}$:
    a) $x_{t+1} = x_t + \Delta x \sim g(x_{t+1}|x_t)$, add a small perturbation to x_t according to a user-defined probability distribution g.
    b) $l_{t+1} = f_2(x_{t+1})$, calculate the likelihood function using the uncertainty probability function f_2 in geophysical interpretation.
    c) Generate random variable α from a 0 to 1 uniform distribution.
    d) Compare $\frac{l_{t+1} f(x_{t+1})}{l_t f(x_t)}$ and α.
    e) If $\frac{l_{t+1} f(x_{t+1})}{l_t f(x_t)} > \alpha$, $x_t = x_{t+1}$, return to (2).
    f) If $\frac{l_{t+1} f(x_{t+1})}{l_t f(x_t)} \leq \alpha$, return to (2).

The posterior distribution can be calculated by fitting a multi-Gaussian model to the $T_{threshold}$ samples.

3.2.4 Training Images From the Rule-Based Model

The images used for training the pix2pix model are generated with UTFLUVPY, a rule-based, channel system modeling program. This software is developed in Python. It is based on the algorithm developed by Pyrcz et al. (2008). The centerline of each channel is initialized as a second-order autoregressive random (AR) process. The two parameters in this AR process are determined by wavelength (k), dampening factor (h), and disturbance variance (s) (Ferguson, 1976). Migrations of channels are modeled using the bank retreat model developed by Sun et al. (1996). Neck cutoffs occur when the centerline of a channel intersects itself. The channel avulsion takes place according to the probability given by the user. The avulsion point is selected at a probability proportional to the curvature of the channel. In this rule-based model, I model five facies: channel fill elements, lateral accretion elements (point bar), levee, abandoned channel element (neck cutoffs), and background shale.

Property trends within different facies are modeled according to the depositional rules. For example, porosity trends in point bars are simulated according to the depositional rules described by Thomas et al. (1987). In directions perpendicular to the active channel's trajectory, sand quality near the channel is higher. Along the trajectory of the channel, sand upstream is of better quality than that downstream. To integrate the vertical upward-fining trend in point bars, point bars deposited earlier are assigned lower quality than those deposited later. Trends in other facies are modeled according to Pyrcz & Deutsch (2014). In the lateral direction, both channels and oxbow lakes have better quality sand in the middle and lower quality sand at the edge. It is assumed that the mean flow rate in an oxbow lake is lower than that in a channel, so the overall sand quality in a channel is higher than that in an oxbow lake. Point bars have the highest quality rock because, at the time of deposition, the flow rate is higher in point bars than in abandoned channels and oxbow lakes. Different types of trends are tested, which are all well reproduced by my machine learning algorithm, but in this dissertation, I only show trends based on the spatial basis of a square root distance function (square root of the distance away from the centerline of a channel).

3.2.4 Applying Stochastic Pix2pix to the Generation of Conditional Models of Fluvial Reservoir Facies

3.2.4.1 Inputs and Loss Functions

To perform more efficient sampling and ensure the generative model converges to the mode constrained by all conditioning data, conditioning data are integrated into both the input and loss function. The loss function is shown in Eq. 3.5. The additional loss term in Eq. 3.4 is composed of the mismatch between the seismic data and well-log data.

3.2.4.2 Seismic Data Conditioning

The proposed workflow assumes that seismic data have been inverted and interpreted to a low-resolution local sand and shale proportion map (Figure 3.3A). The inverted and interpreted image is applied in both the input layer and loss function. In the loss function, an additional MSE term (Eq. 3.6) between the back-calculated proportion map and the training proportion map is added (Figure 3.3A). The additional loss term for seismic data conditioning is expressed as

$$\mathcal{L}_{\text{seismic}}(G) = -\frac{\sum_{i=1}^{N}\sum_{k=1}^{K}(t_{ik} - t_{ik}^{*})^2}{NK} \tag{3.6}$$

where N is the batch size, K is the number of pixels in the reservoir model; t_{ik} is the probability that in the i_{th}realization, facies at $\mathrm{k_{th}}$ pixel is sandy; t_{ik}^{*} is the probability that in the i_{th}training image, facies at $\mathrm{k_{th}}$ pixel is sandy facies

3.2.4.3 Well Data Conditioning

As in seismic data conditioning, facies at well locations in the training images are applied in both the input and loss function of the stochastic pix2pix model. The additional loss term for well data conditioning can be expressed as

$$\mathcal{L}_{\text{well\_log}}(G) = -\frac{\sum_{i=1}^{N}\sum_{L=1}^{L}\|w_{il} - w_{il}^{*}\|_2}{NL} \tag{3.7}$$

where N is the batch size, L is the number of well-log interpretations, w_{il} is the probability of each facies at the lth well location in the ith reservoir model realizations, and w_{il}^{*} is the one-hot encoding (Paktar, 2017) of the facies at the lth well location in the ith training image.

3.2.4.4 Encoding the Parameters of Rule-Based Models

Parameters of the rule-based models, such as channel width, levee width, cutoff threshold, and avulsion frequency vary when generating training images. To ensure sufficient training images for different combinations of parameters, to decrease the number of input parameters, and to avoid mode collapse, training images are clustered according to the properties of their corresponding rule-based model using K-means clustering and encoded by a feed-forward neural network. I employ K-means clustering for the ease of interpretability and sufficient simplicity for the workflow. The output from this neural network is reshaped to that of the training image and used as input in the stochastic pix2pix model (Figure 3.1). Although I do not explicitly incorporate these model parameters into the loss function, the results show that the generated images are consistent with the input model parameters (Figure 3.6). 100 Gaussian random variables in latent space are also combined with a feed-forward neural network to generate a random model parameter map with the same shape as the training image (Figure 3.1).

3.2.4.5 Encoding the Parameters of Rule-Based Models

I add all the additional loss terms and rewrite the total loss function (Eq. 3.5) as

$$\mathcal{L}^*_{\text{sto}}(x,z) = arg\min_G \max_D \mathcal{L}_{CGAN}(G,D) + \lambda_{seis}\mathcal{L}_{\text{seismic}}(G) + \lambda_{log}\mathcal{L}_{\text{well\_log}}(G) \tag{3.8}$$

where λ_{seis} and λ_{log} are the certainty coefficients of the seismic and well-log interpretations. The weights, λ_i, must be small enough to avoid overfitting and to generate diverse realizations.

The purpose of the training process is to find the parameters in the CNNs that minimize $\mathcal{L}^*_{\text{sto}}$. Figure 3.3 shows the inputs and outputs for the generator. Inputs for the generator are a proportion map of the training image (seismic interpretation) (A); facies data in the training image at well locations (well-log interpretation) (B); random variable map generated from 100 random variables in latent space (C); and random model parameter map from the parameters of the rule-based models (D). These are stacked and input into the generator (Figure 3.1) to generate simulated facies distributions (E). As for the discriminator (Figure 3.4), the inputs are the generated facies distribution (E), and the training images (E*). Another option is to use (A), (B), and (D) as input if the number of training images is large. The output of the discriminator is the probability that an input reservoir model is from the training set. The algorithms for training the generator and discriminator and for performing prediction are summarized as

- Generator:
    1) Generate (C) and (D) using feed-forward neural networks from low-dimensional variables.
    2) Extract (A) and (B) from the training images.
    3) Combine (A), (B), (C), and (D) and use them as input for U-Net (Figure 3.1) to generate the facies distribution (E) and back-calculate (A) and (B). Find weights for U-Net by minimizing $G^*{}_{sto}$.
- Discriminator:
    1) Combine (E), (E*) and use them as input for the discriminator CNNs (see Figure 3.2). Optionally, also input (A), (B), and (D) into the CNNs.
    2) Differentiate the generated and training images and find weights for the discriminator by maximizing $\mathcal{L}_{CGAN}$.
- Prediction:
    1) Obtain (A) and (B) from seismic interpretation and well-log interpretation, respectively; generate (D) from prior knowledge about the depositional environment of the reservoir; generate (C) as a Gaussian field with 0 mean and 1 variance.
    2) Use (A), (B), (C) and (D) as input for the generator; the outputs are conditional realizations.

The generator and discriminator are sequentially trained until Nash equilibrium is reached. To find realizations that best match the seismic and well-log interpretations, we can use the Metropolis-Hastings method to sample the realizations from the generator (see Figure 3.5).

3.2.4.6 Property Model Generation with Stochastic Pix2pix

Continuous subsurface property model generation is similar to facies model generation, except for the input and output. In a stochastic pix2pix model, the inputs for reservoir property model generation are well-log interpretations (B) and facies maps generated in facies modeling (E). These output a continuous property trend model. Depending on the application, continuous property noise based on two-point statistics can be added to property trend models to optimize well log match and to incorporate heterogeneity into the reservoir models (similar to the method of Pyrcz et al., 2005).

3.2.4.7 Training Image Generation and Hyper-Parameters

The synthetic case comprises 10,000 images with a cell size of 16m as the training set. The training images are generated with the rule-based channel reservoir simulator UTFLUVPY. I also generate a validation set of 1,000 reservoir models with different random seeds. The shapes of training images, validation models, and realizations are all 56×56. I train the stochastic pix2pix model on the training set and evaluate its performance on the validation set. For each training image, its parameters in rule-based modeling are uniformly sampled from Table 3.1, and consistently used during the rule-based modeling.

The architecture of the stochastic pix2pix model is tuned to optimize the results. The shape of latent space is fixed at 100×1. In the generator (Figure 3.1), there are 6 convolutional layers with the rectified linear unit (ReLU) activation functions and 1 output layer with the SoftMax activation function to generate categorical probability (Figure 3.6). The discriminator has 3 intermediate CNNs with ReLU activation functions and an output layer with a Sigmoid activation function (Figure 3.2). Adam optimization (Kingma & Ba, 2014), with a learning rate of 0.0002, is used for model calibration. I employ the Adam optimizer because it requires less memory and is not very sensitive to hyper-parameters. I train the stochastic pix2pix model on a Tesla P100 GPU with a batch size of 128 for 1,000 epochs. After training the model for 10,000 epochs, realizations still show diversity, with no mode collapse when λ are small. To perform continuous property modeling, one only needs to change the SoftMax activation function in the output layer of the generator to the Tanh function and scale the property in the training images to between -1 and 1. By scaling the property and introducing the Tanh function, I introduce more non-linearity, thereby preventing the neural network from fitting to potential outliers.

3.2.5 Model Evaluation

Performance evaluations for my suggested workflows are based on two factors, namely, how accurately the generated reservoir models predict the conditioning data in the true model and how well the reconstructed reservoir models reproduce the patterns of training images. The pattern reproduction is evaluated by indicator variogram and histogram. The accuracy of data conditioning is quantified by the mean categorical error, calculated as

$$L_{cat} = \frac{\sum_{i=1}^{N} \sum_{k=1}^{K} m_{ik}}{NK} \tag{3.9}$$

where N is the batch size, K is the number of pixels in the reservoir model, and m_{ik} is a point in the binary correctness map that equals 0 if the facies at k_{th} pixel is the same in both the true model and i_{th} realization.

3.3 RESULTS

3.3.1 Controlling the Geometries of Realizations

I investigate the effect of the input architecture parameters (Figure 3.3D) on the realizations. I assume the correct channel width, levee width, and neck cutoff threshold are unknown. By changing these parameters (see sec. 2.5.4), I expect to change the input layer (D) and control the corresponding features in the generated reservoir models while honoring the seismic interpretation. The results in Figure 3.7 show the realizations with the same seismic conditioning image and different input architecture parameters. It can be seen from these results that the stochastic pix2pix model successfully controls the corresponding features for the given inputs.

3.3.2 Conditioning the Realizations to Accurate Seismic Interpretation

To generate realizations only conditioning to seismic data, I first set λ_{log} to 0 and λ_{seis} to 100, and then delete the well-log facies map in the input layer of the generator (Figure 3.3). In Figure 3.8, I show different realizations generated with the stochastic pix2pix method with the same channel and levee widths and neck cutoff threshold as the true model. The boundary between sandy and shale facies in the true model is well reproduced in realizations, indicating that the realizations honor the seismic interpretations. The mean categorical error (see Eq. 3.9) for seismic interpretation is 0.34%.

The continuous channel fill with low curvature in each realization shows that the stochastic pix2pix method captures long-range spatial patterns. Neck cutoffs with high curvatures show that the method can also capture the local short-scale, spatial features. The distribution of levee facies at the edge of a channel complex is consistent with fluvial channel deposition concepts. Finally, spatial diversity between different realizations shows that this method mitigates the mode collapse and overfitting problems.

In Figure 3.9 I explore model diversity with the probability maps of different facies and the corresponding Shannon entropy map. There are low uncertainties in shale and levee facies distribution, owing to the assumption of accurate seismic interpretation and known channel and levee width. Compared to the probability map of neck cutoffs, the probability map of the abandoned channel (channel fill) shows lower curvature. Point bars away from shale and sand boundaries show higher uncertainty. The Shannon entropy map demonstrates high uncertainty in the center of the sandy facies because the boundary does not provide much information about facies distribution within.

In Figure 3.10, I compare variograms and histograms of different facies from the true model and the realizations. Both histograms and variograms of the realizations match the true model with a high degree of accuracy. The standard deviation of the error in all variograms is less than 10%. Categorical histograms of the proportions of neck cutoffs, abandoned channel, and point bar facies over the realizations are slightly different from those in the true model, indicating that the method does not constrain the realizations to a specific proportion of facies. Facies proportion may be added to the input and loss function in the future, so that calculations from well-log interpretation can be used to better constrain the generated realizations in a relatively stationary reservoir.

3.3.3 Realizations Conditioned to Seismic and Well-Log Interpretation

I generate conditional realizations via the standard stochastic pix2pix workflow. λ_{seis} is set to 100 and λ_{log} is set to 10.

In Figure 3.11 I show different realizations generated with the stochastic pix2pix method having the same channel and levee widths and neck cutoff threshold as the true model. Compared to realizations without well log conditioning, the facies distributions show less variety than expected. Although the realizations do not perfectly match the facies at well locations, most of the facies at well locations are correct. The mean categorical error for seismic interpretation is 0.41% (Eq. 3.9), and the error for well-log interpretation is 6.71%.

Probability and Shannon entropy maps are shown in Figure 3.12. In both the probability and Shannon entropy maps, the facies uncertainties near well locations greatly decrease to an average of 0.2042. So, for example, the probability map of the abandoned channel shows that the channel is more likely to be located at the center of the channel complex.

Variograms and histograms of different facies after well log conditioning are compared in Figure 3.13. After conditioning to well data, the realizations more closely reproduce the variograms and histograms of the true model.

The training process of the proposed method for generating conditional realizations only takes about 2 hours of CPU time, and it is faster than the stochastic sampling method. My models are relatively small compared to the real reservoir model, but the stochastic pix2pix method can be applied hierarchically to downscale the reservoir model, i.e., the low-resolution output can be discretized into several patches, and each patch can be used as input for another stochastic pix2pix model to generate part of a high-resolution reservoir model. Such a procedure of generating high-resolution reservoir models--more computationally efficient and requiring less memory than direct full-scale 3D reservoir modeling--will be the subject of my future work.

3.3.4 Model Realizations with High Uncertainty

To generate conditional realizations in settings with a high degree of seismic and well-log interpretation uncertainty, we can integrate multiple subsurface geophysical and petrophysical interpretations and reduce the weight of seismic and well-log conditioning in the loss function. Given only one set of uncertain seismic and well-log interpretations, I use CGAN to generate possible seismic and petrophysical interpretations and set both λ_{log} and λ_{seis} to 0.1. I then use the stochastic pix2pix method to model the facies distribution conditional to high-uncertainty seismic and well-log interpretation. Realizations are shown in Figure 3.14. Here I see more diversity in the distributions of different facies, but the patterns in the training images are preserved.

Probability maps of different facies and the Shannon entropy map are shown in Figure 3.15. There is reduced certainty in the local facies distribution; however, the general pattern of each facies is preserved. As expected, high uncertainties associated with the interpretations lead to a map with high Shannon entropy.

The variograms and histograms of different facies are shown in Figure 3.16. The realizations have much higher entropy than that shown in cases assigned a higher degree of seismic and well-log interpretation certainty. The histograms are not well matched and the variograms of different facies also show larger variations from the true model.

3.3.5 Multiple Point Statistics Validation

To validate that my method successfully reproduces the higher-order statistics in the training images, I compare the multiple point density functions between the training images and realizations conditioned to both seismic and well-log interpretation. A comparison of the density functions with a 4-point template (Boisvert et al, 2010) is shown in Figure 3.17, only 10 configurations with the highest frequencies are shown.

I also calculate the difference between the multiple point density functions with 4-, and 9-point templates for training images and realizations. I only perform the calculation for 4- and 9-point templates because there are 5 facies in my models. An n-point template has 5^n different configurations. Too much memory and computational resources are required to perform MPS or density function calculation when n is large. The difference between the MPH of training models and model realizations with a 4-point template is 0.0848, and the difference with a 9-point template is 0.1677, which I think is acceptable.

3.3.6 Property Modeling

The facies map is used as input in another stochastic pix2pix model to generate the within-facies property model. Facies trends include point bars where sand quality is lower transitioning to the center of channels with the highest-quality sand. Sand quality in the center of a channel or an oxbow lake is higher than that at the edge.

In both the true model and realizations (Figure 3.18), I observe that point bars adjacent to the active (abandoned) channel fill have better sand quality than those surrounded by oxbow lakes or those away from the channel. I can track the potential depositional order from some of the realizations, which indicates that the order of depositional time in training images is effectively learned by the stochastic pix2pix model. The lateral trends of all facies in the realizations follow the rules defined in Sec. 2. 4. These property models are of direct use, therefore, for reservoir simulation and history matching. Two-point statistics-based residuals can be added to the property models to better capture well-log interpretation results and their statistics.

3.3.7 Comparison to Pix2pix Method

I use the M-H sampling method to find the best match that was generated with stochastic pix2pix and compare it with that generated with the pix2pix method (Figure 3.19). Data matching of both the stochastic pix2pix method and the pix2pix method are good. The mean categorical errors (Eq. 3.9) of seismic interpretation reproduction are 0.096% and 0.542% for the stochastic pix2pix method and the pix2pix method, respectively. The mean categorical errors of well-log interpretation reproduction are 4.5% for both methods. However, the stochastic pix2pix method preserves the patterns of different facies better than does pix2pix; in addition, the stochastic pix2pix method generates more diverse realizations (Figures 3.14 and 3.18). Compared to workflows with inpainting for well data conditioning (Jo et al., 2019), my proposed method does not create artifacts near wells, and the long-range patterns of different facies are better preserved.

3.4 DISCUSSION

The stochastic pix2pix method generates diverse facies and property distributions conditioned by seismic and well data and thus is highly applicable for decision-making in subsurface development operations. Reservoir models generated with this method preserve the patterns observed in the training images, e.g., continuous, small-curvature active channel fill, large-curvature neck cutoffs, drip-like point bars, and continuous levees distributed at the boundary of sandy facies. However, most of the results are based on numerical experiments with the same forward model. This section discusses the robustness of my method for realistic seismic interpretation (field data), how to apply it for real-time reservoir management and pre-drill assessment, the factors controlling the spatial smoothness of the parametric properties, and the method's application to large-scale, complex turbidite channel systems.

3.4.1 How Robust Is Stochastic Pix2pix Method?

In applying this method to field data, one may come across seismic/well-log interpretations that are very different from the training images; in cases such as these, unconditional realizations generated by methods like GAN may not produce satisfactory stochastic reservoir models, which have the same conditioning data. To show the robustness of this method, I apply it to the map of Texas and real seismic interpretations, which are transformed into binary facies maps and used as a constraint. As we can see from Figures 3.20 and 3.21, even though the conditional images are different from those in the training images, the proposed method still reproduces diverse long-range and short-range patterns of facies consistent with the outline. In Figure 3.21, the generated reservoir model reproduces the outline of the segmented seismic interpretation. Potential locations of neck cutoffs, point bars, and channel fills can be identified from the ensemble of realizations.

3.4.2 How Can Stochastic Pix2pix Method be Applied to Real-Time Reservoir Management and Pre-Drill Assessment?

This 2D model is suitable for reservoirs with high aggradation rates or reservoir units with high degrees of vertical isolation. Nevertheless, its extension to 3-D is straightforward. My method has two advantages over other rule-based or object-based methods. First, it can perform fast simulation and conditioning; second, it can parameterize high-dimensional reservoir models to low-dimensional input parameters. This allows us to update the reservoir in real-time and make optimal decisions based on the latest reservoir model. For example, during the exploration phase, we may drill wells to reduce the uncertainty of the reservoir model, targeting locations with high Shannon entropy to maximize information. During the reservoir development phase, we may drill wells intersecting the facies with high certainty of the highest rock quality based on the facies probability map.

With this new reservoir modeling method, we can obtain the probability map of facies distribution as well as property distributions. This information is vital for future drilling and completion operations, e.g., for areas with high uncertainties we may adopt a more conservative drilling strategy. Given this knowledge, we can also design well-log operations to maximize the sensitivity of well logs to the expected range of formation properties or expected lithofacies. Thus, for wells in areas with low uncertainty, we may require fewer well logs. The probability maps can also help petrophysicists choose optimal coefficients for petrophysical models. The entire proposed workflow is summarized in Figure 3.22.

3.4.3 How Does the Training Set Affect the Realizations?

A large training data set does not necessarily yield good results, although a training data set with consistent patterns does. The most important advantage of the stochastic pix2pix method is that it uses the CGAN structure, which allows us to label the training images based on the similarity of their patterns. For example, we can divide the training images based on their mean channel, levee widths, and avulsion probability.

By dividing the training set into groups with more consistent, or stationary, patterns, the performance of my model is enhanced, and we can experiment with more conceptual models. For example, to test if the reservoir is a meandering channel complex, we may use low avulsion frequency and large channel width in the input layer of the stochastic pix2pix model, whereas to test if it is a distributary fluvial delta system, we may use high avulsion frequency and small channel width in the input layer. I will discuss the implications of dividing training images by pattern in my future work.

In this dissertation, I use training images generated with a rule-based model. However, images from high-resolution seismic interpretation and tomography photos can also be used as training images, although manual assignment of labels may be required in these cases.

3.4.4 How Well Does the Stochastic Pix2pix Method Parameterize Low-Avulsion Rate Channel Systems?

My hope, in parameterizing one set of random variables to another set of variables, is that the mapping can be as linear as possible, and the response surface for the two sets of variables as smooth as possible. The stochastic pix2pix method maps complex reservoir models to a 100×1 Gaussian space. To test whether a smooth change in Gaussian space can yield a smooth change in reservoir models, I use the gradual deformation method (Hu, 2000; Hu & Jenni, 2005), given by

$$Y(t) = Y_1 \sin(t) + Y_2 \cos(t) \tag{10}$$

where $Y(t)$, Y_1, and Y_2 are Gaussian random functions, and t is the angle. It can be proved that a new Gaussian random function, $Y(t)$, can be defined as the sum of two independent Gaussian random functions Y_1 and Y_2 weighted by trigonometric functions. By changing the angle, t, I continuously sample between two random variables in the Gaussian latent space. As shown in Figure 3.23, the mapping is smooth because the reservoir models also change continuously; for example, the abandoned (active) channel fill gradually deforms to originate new point bars and neck cutoffs. Figure 3.23 shows that when the channel intersects itself, a neck cutoff forms, which is consistent with the sedimentary process I try to mimic. Similarly, most of the realizations do not break the rules I used to generate training images. We may conclude, therefore, that the stochastic pix2pix method manages to learn the migration rule of the meandering channel system. The combination of stochastic pix2pix and gradual deformation methods can be directly used for history matching.

3.4.4 Application to Large-Scale, Confined Complex Turbidite Reservoir Modeling

The examples shown in previous sections are relatively simple and small. In this section I discuss how to generate training images representing a large-scale, complex turbidite system, using the same ML algorithm to generate realizations conditioning to the boundary of the canyon in which the turbidite channel system resides. The size of the realizations is 1024×256, which can be directly used for field applications.

In rule-based reservoir modeling, when conditioning the channel models to the boundary of a channel complex, many artifacts may be introduced. Channels that intersect the channel complex boundary during accretion may have to be abandoned; or, the accretion rate toward the boundary may be damped to avoid the intersection between channel elements and the boundary. To avoid these artifacts, I use unconditional training images and then employ stochastic pix2pix to perform the conditional model generation. In Figure 3.24, patterns such as continuous channel fill, neck cutoffs indicating left-to-right flow direction, and levee filling to the canyon's confines, all indicate that the stochastic pix2pix method can reproduce the patterns for a large-scale, complex turbidite reservoir.

3.5 CONCLUSIONS

The following conclusions stem from the implementation and verification of new method of stochastic pix2pix for modeling low-avulsion rate channel systems:

1) Results show that the pix2pix modeling method can reproduce the patterns in each facies contained in the training images while honoring static data, and the stochastic pix2pix method improves the pattern reproduction and the diversity of the realizations (see Sec 3.6).

2) The stochastic pix2pix method is successfully applied to construct fluvial reservoir models consistent with well-log and seismic interpretation. It can also be

expressed as downscaling from seismic-scale interpretation to reservoir scale required for flow forecasting. Compared to conventional reservoir modeling and conditioning methods, the proposed method improves computational efficiency and pattern reproduction when simulating and conditioning models (see Sec. 3.1, 3.2, 3.3, 3.4, 4.1).

3) The stochastic pix2pix method reproduces the patterns observed in rule-based fluvial training images, such as continuous, small-curvature active channel fill; large-curvature neck cutoffs; drip-like point bars; and continuous levees distributed at the boundary of sandy facies. One common limitation of generative machine learning methods, however, is that they do not precisely quantify the quality of the reproduction of the patterns in the training images. Therefore, I used visual evaluation and two-point statistics to qualitatively verify that the patterns were adequately reproduced (see Sec. 3.2, 3.3, 4). Additional metrics such as multiple-point histograms could be considered as well (Boisvert et al., 2010).
4) Property models generated with the stochastic pix2pix method follow the trend that we observe in rule-based models. The new method serves as a good parameterization tool for history matching because the 100 variables in latent space represent a much smaller number of variables than otherwise necessary to capture the properties for all the grids.
5) The method can continuously modify the active channel continuously to mimic real meandering channel migration. I regard this as evidence that the new method manages to learn the depositional rule of the meandering channel's point bar

system (see Sec. 4.4). This algorithm can model large-scale channel systems (see Sec. 4.5).

6) I anticipate the new workflow being used by reservoir engineers and geologists as an alternative to conventional MPS and rule-/object-based reservoir modeling methods, allowing them to more efficiently and accurately perform stochastic reservoir modeling and conditioning for channel reservoirs such as fluvial or turbidite systems. The following steps are recommended for optimal performance: first, facies models should be built with the stochastic pix2pix method with relatively low certainty coefficients, λ, with a sampling of realizations performed as necessary; next, property trend modeling conditioned to facies models should be performed by another stochastic pix2pix method; and last, two-point statistical property noise should be added to the property trend model via co-simulation methods.
7) The main limitation of my method is that it is currently applicable to 2D models. It can only be directly used in cases where the aggradation rate of a reservoir is high, e.g., in the upper part of a turbidite sequence. However, 3D models can be easily generated via zone-by-zone (reservoir unit) simulation, which will be the focus of my future work. Also, because the size of the reservoir model is relatively small, I will use by-patch downscaling to hierarchically increase the size of the model and add details to it in future investigations.

Table 3.1: Summary of the ranges of parameters input for the rule-based model.

Parameter	Low	High	Parameter	Low	High
k	0.08	0.15	Channel width	32 m	128 m
h	0.3	0.5	Levee width	32 m	384 m
s	0.03	0.07	Cutoff threshold	64 m	320 m
Avulsion frequency	0.0	0.0			

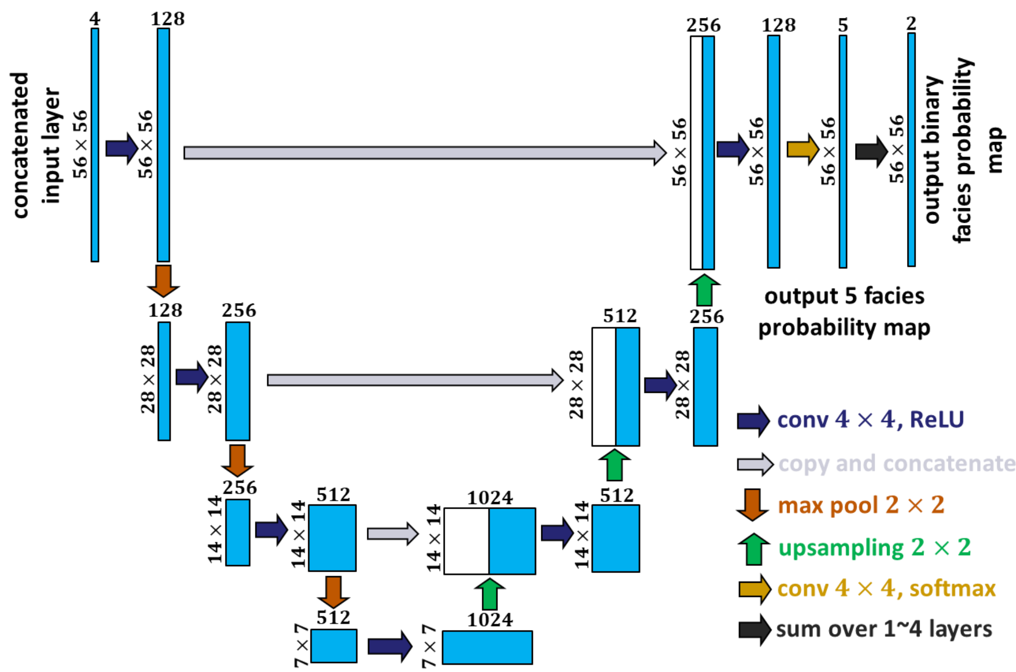

Figure 3.1: Structure of the generator (example of training images with 56×56 pixels). It is a U-net structure. Inputs for the generator are four concatenated layers. The first two layers are conditioning images (well-log map, seismic interpretation) whose sizes are both 56×56. The third layer describes the expanded architectural geometries (channel, levee widths, cutoff threshold); its original shape is 3×1 and is expanded to 56×56 using a fully connected neural network to be compatible with the shape of the reservoir model. The last layer describes the expanded random variables; its original shape is 100, and it is also expanded to 56×56. Concatenated inputs are encoded with a series of CNNs and down-sampling layers and are then decoded by a series of CNNs and up-sampling layers; short cuts between encoding layers and decoding layers preserve the local features. The generator first outputs the probability map of all 5 facies; it then back-calculates the two layers of conditioning images.

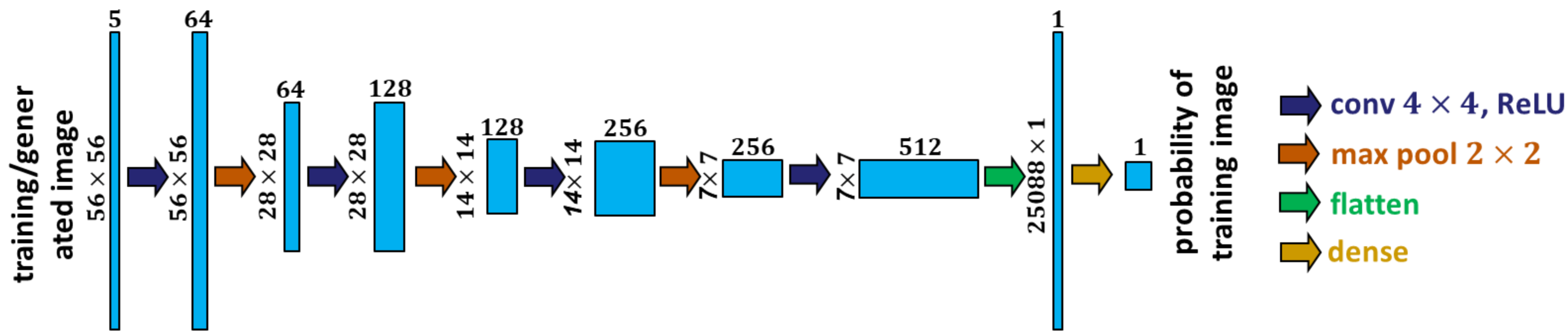

Figure 3.2: Structure of the discriminator (example of training images with 56×56 pixels). It is a series of CNNs. Inputs to the generator are the one-hot encoding (Potdar et al., 2017) of either training images or generated realizations (one-hot encoding transforms categorical facies models into higher dimensions with values of only 0 or 1). Patterns in those images are extracted by a series of CNNs. In the last layer, patterns extracted from CNNs are flattened and linked with a fully connected neural network (NN). The NN then outputs the probability that the input image comes from the ensemble of training images.

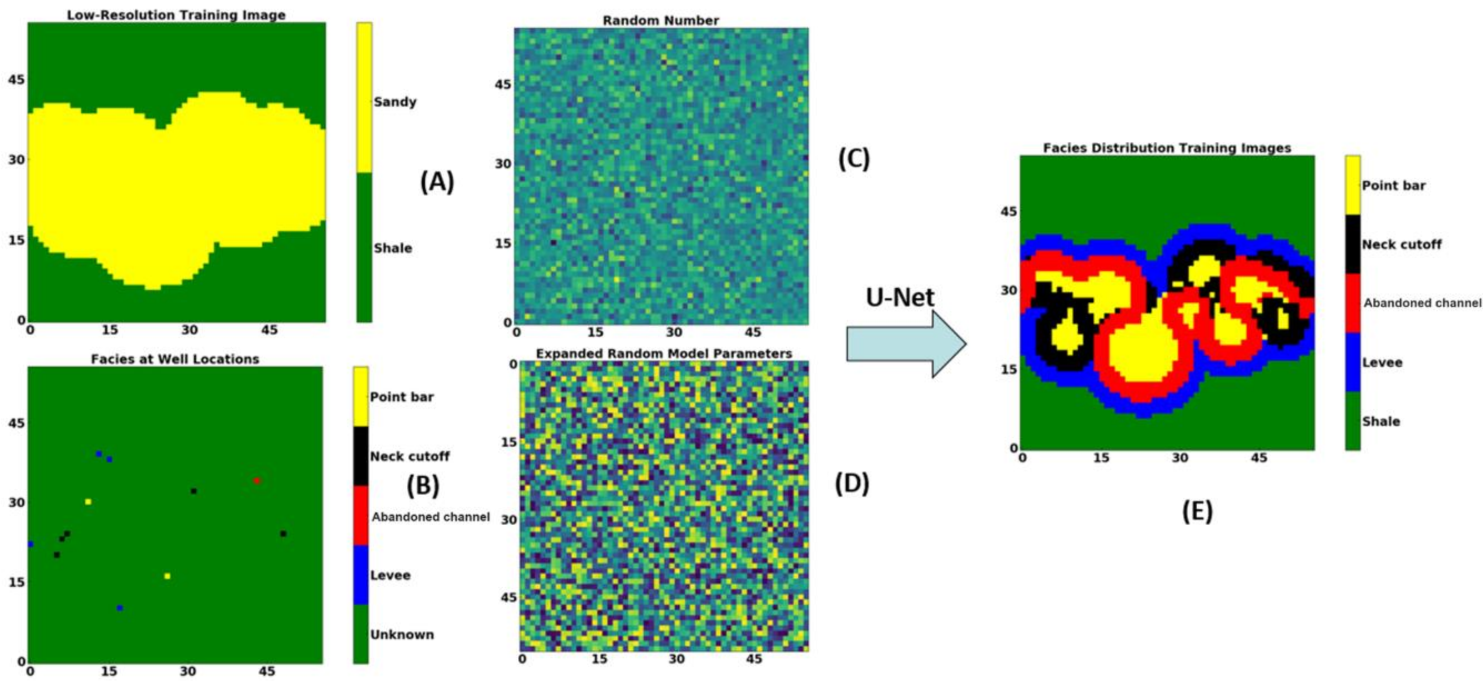

Figure 3.3: Generator architecture for reservoir modeling problems. Inputs for the generator are (A) seismic interpretation map from training images; (B) facies in the training images at well locations; (C) random variables generated from 100 variables in latent space; (D) image generated from random model parameters (channel width, levee width, etc.). These inputs are concatenated and sent into the U-net in the generator to yield one realization of the training image; (E) is the back-calculation of the seismic interpretation and well-log interpretation from the realizations.

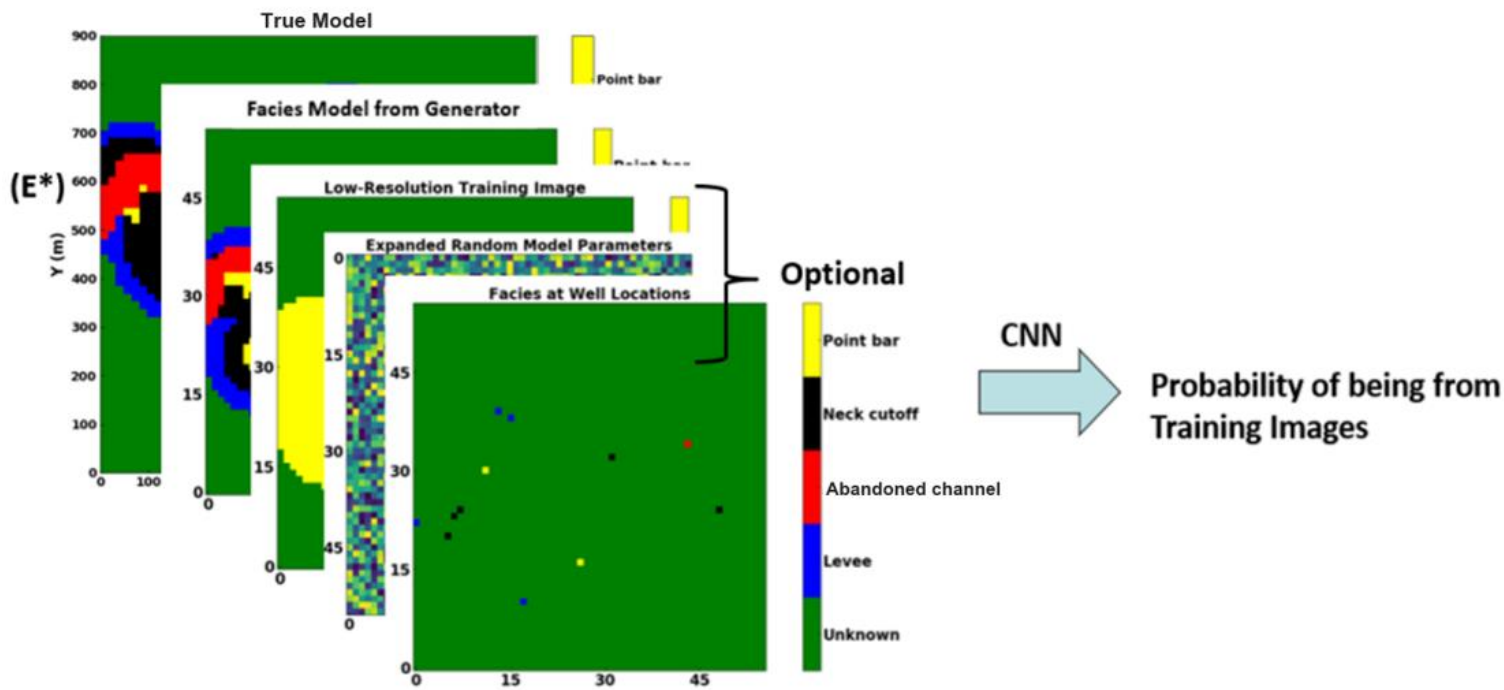

Figure 3.4: Discriminator architecture for the reservoir modeling problem. Inputs for the discriminator are (E*) true model or (E) realizations from the generator. Alternatively, one can input (A) upscaled, low-resolution binary facies distribution from training images; (B) facies in the training images at well locations; (D) image generated from random model parameters (channel width, levee width, etc.). If the number of training images available is small, (A) (B) (D) can be clustered and transformed into labels or omitted in the analysis.

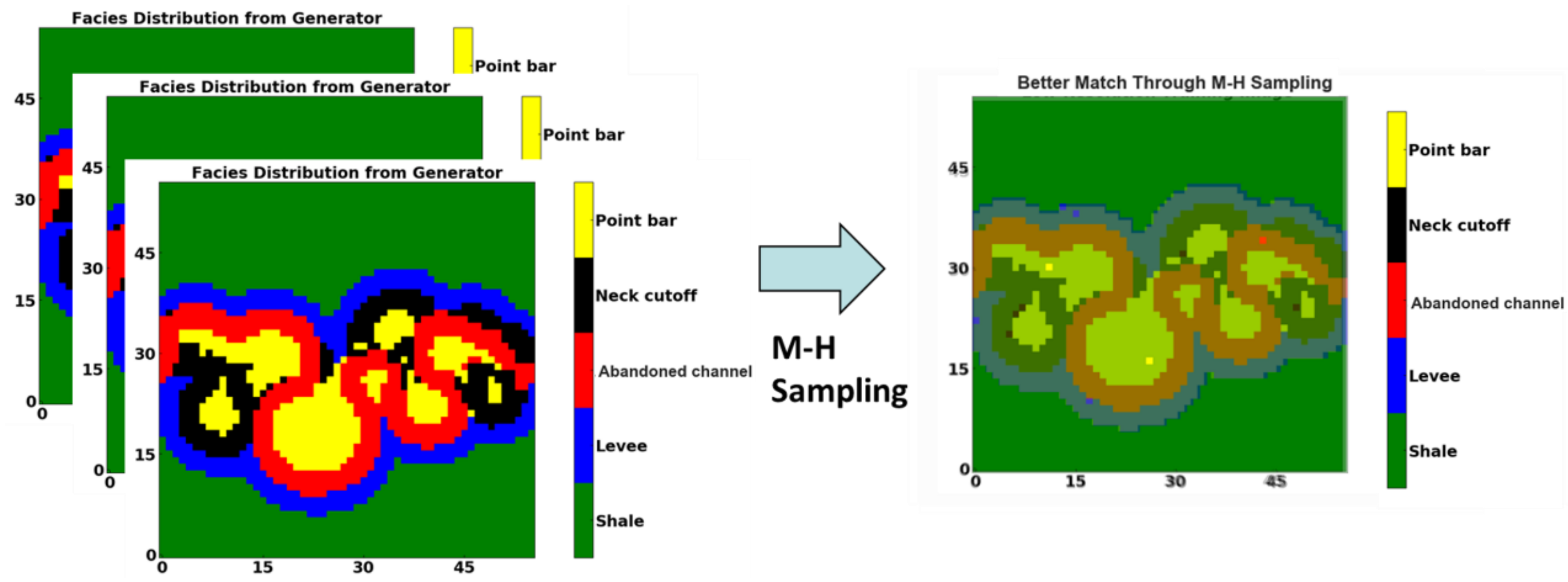

Figure 3.5: Realizations that match the static conditioning data best are found by minimizing the mismatch with seismic interpretation and well-log interpretation using the Metropolis-Hastings (M-H) sampling method.

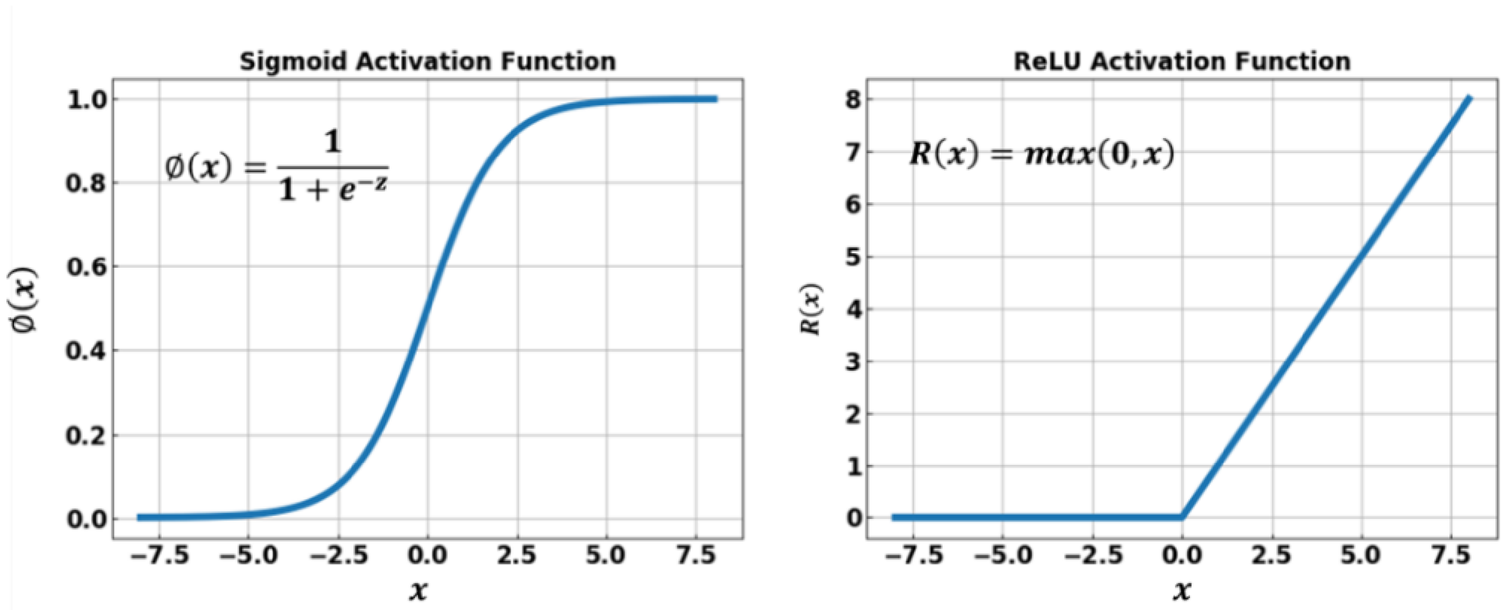

Figure 3.6: Sigmoid and ReLU activation functions. The Softmax activation function is a multivariate sigmoid activation function.

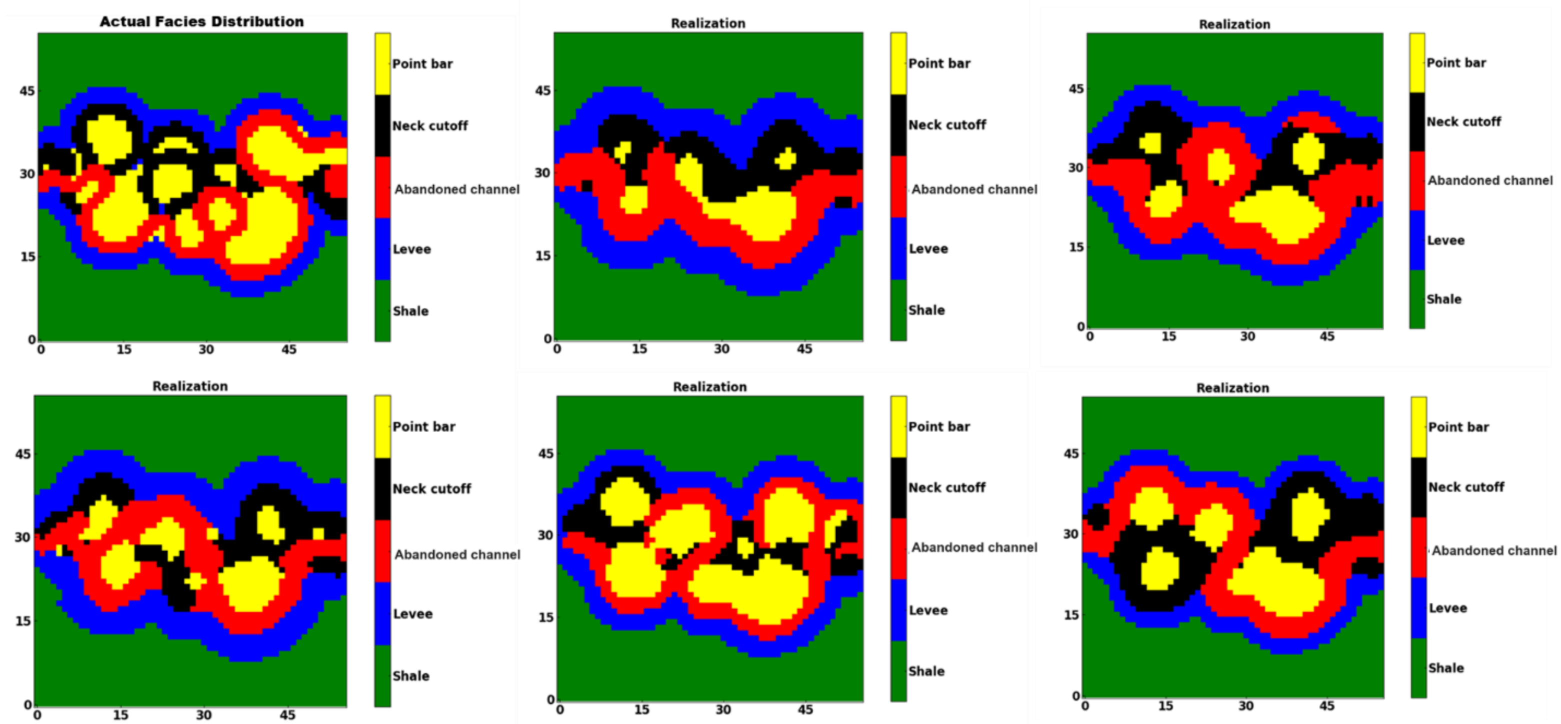

Figure 3.7: Conditioned realizations with different channel and levee widths. Compared to the true model, reservoir model realizations have similar shapes of sandy and shale facies but different channel and levee widths. These results indicate that we have good control over the architecture parameters (in this case, levee and channel widths) by specifying them in the input layer (D) of the stochastic pix2pix model.

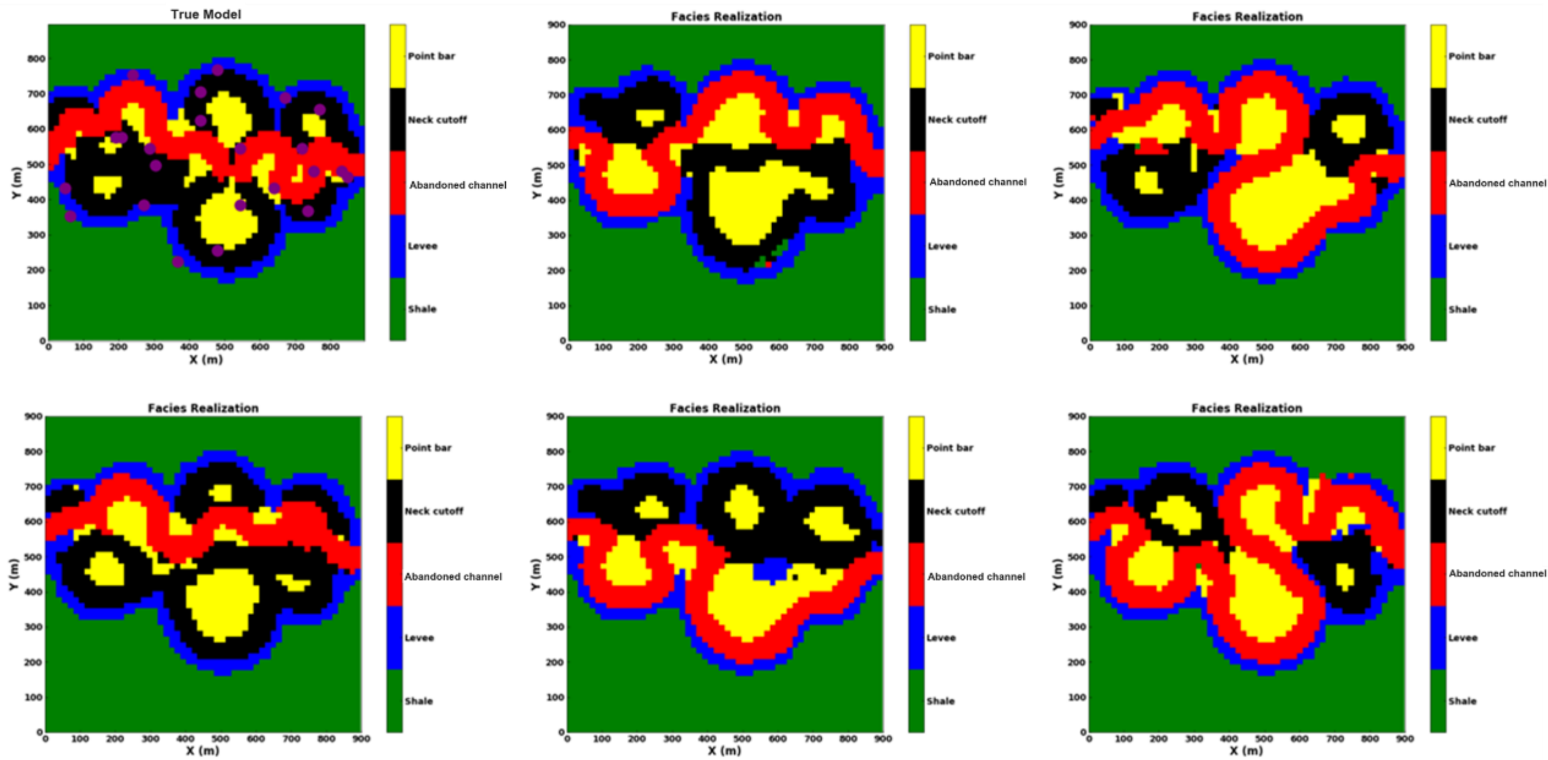

Figure 3.8: Realizations with fixed channel and levee widths and neck cutoff threshold conditioned by seismic interpretation only. The realizations match the outline of the true model; patterns of different facies are preserved and consistent with fluvial channel depositional concepts. Facies distributions are different from realization to realization, confirming that the method solves the mode collapse problem associated with other GAN methods.

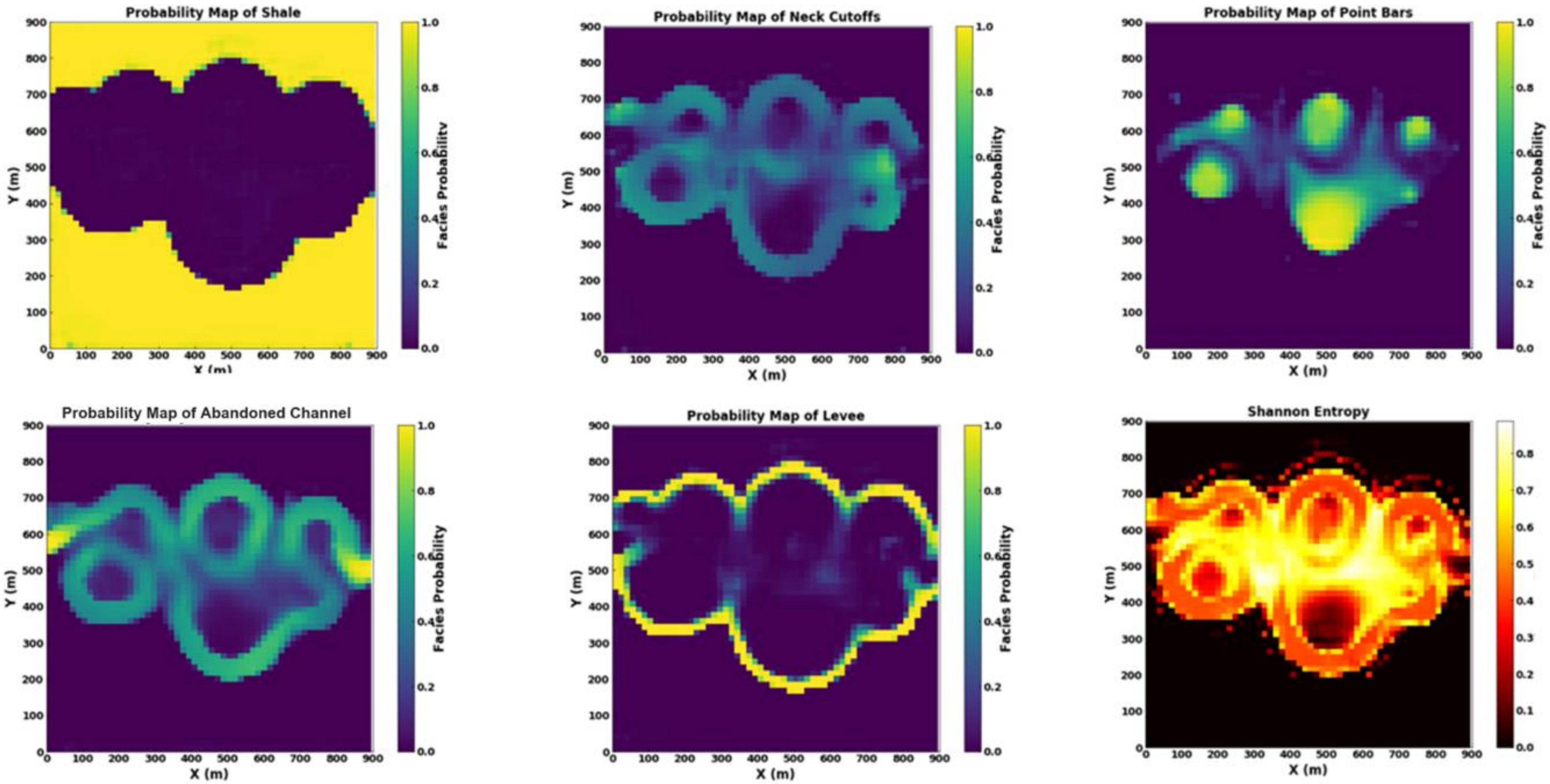

Figure 3.9: Probability maps and Shannon entropy map of different facies with fixed channel and levee widths. The Shannon entropy map summarizes the local uncertainty in the facies distribution; the lighter the color, the greater the uncertainty. Large λ_seis forces realizations to exhibit marginal variation at sand/shale boundaries; the shale facies also exhibits low uncertainty. Fixed levee width causes the levee facies to have low uncertainty as well. I find high uncertainty in the distribution of neck cutoffs, point bars, and abandoned channels. The Shannon entropy map indicates that the center of sandy facies has the highest uncertainty because the information from the sand/shale boundary degrades with distance from the boundary.

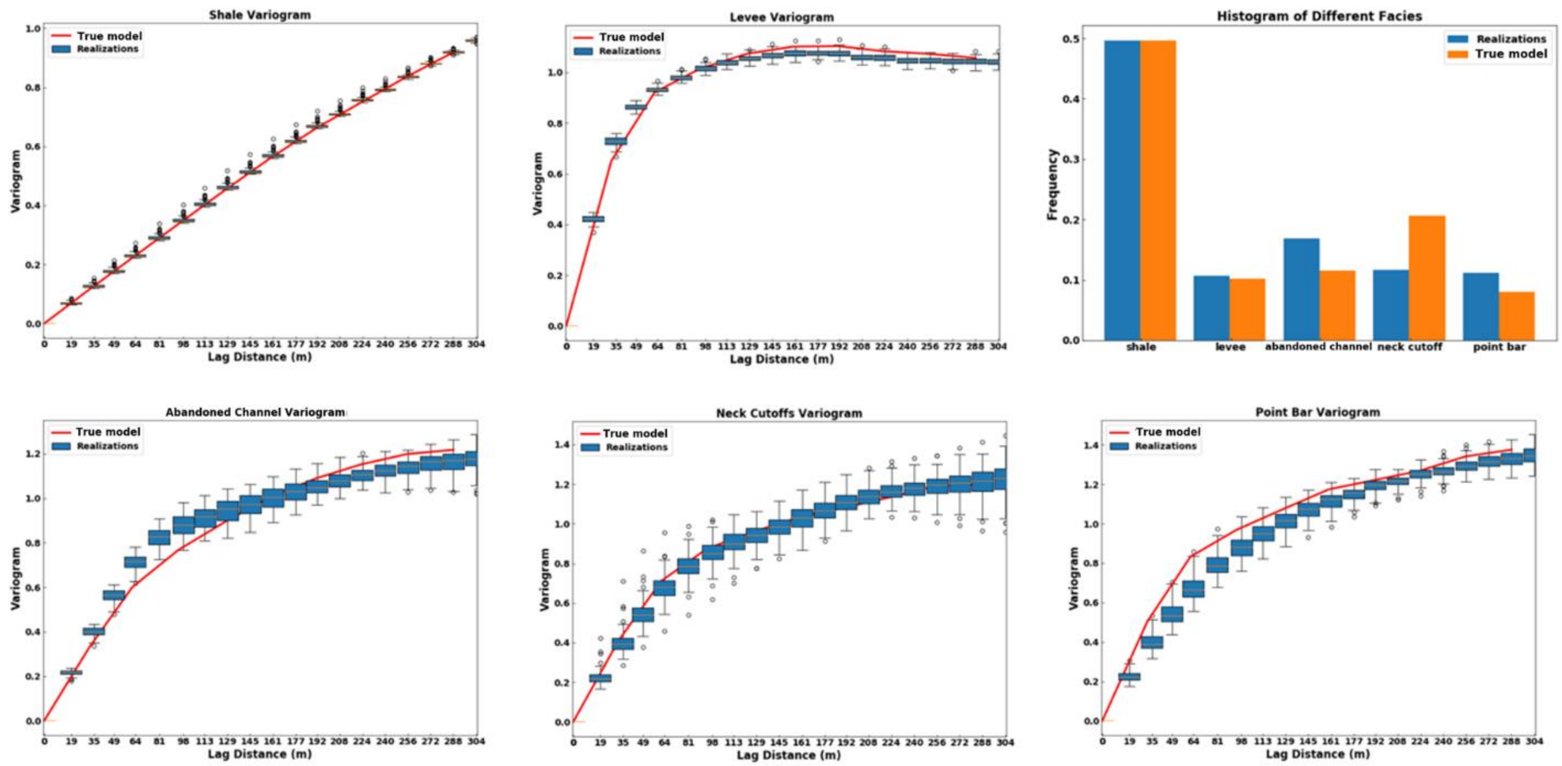

Figure 3.10: Indicator variograms and histograms of different facies. Variograms and histograms of different facies are accurately reproduced in the realizations. The match of variograms is good except for the abandoned channel and point bar, where the lack of information at the center of sandy facies causes underestimation of the continuity of channel facies and overestimation of the continuity of point bars. Differences in the histogram are mainly caused by facies variation away from the sand/shale boundary.

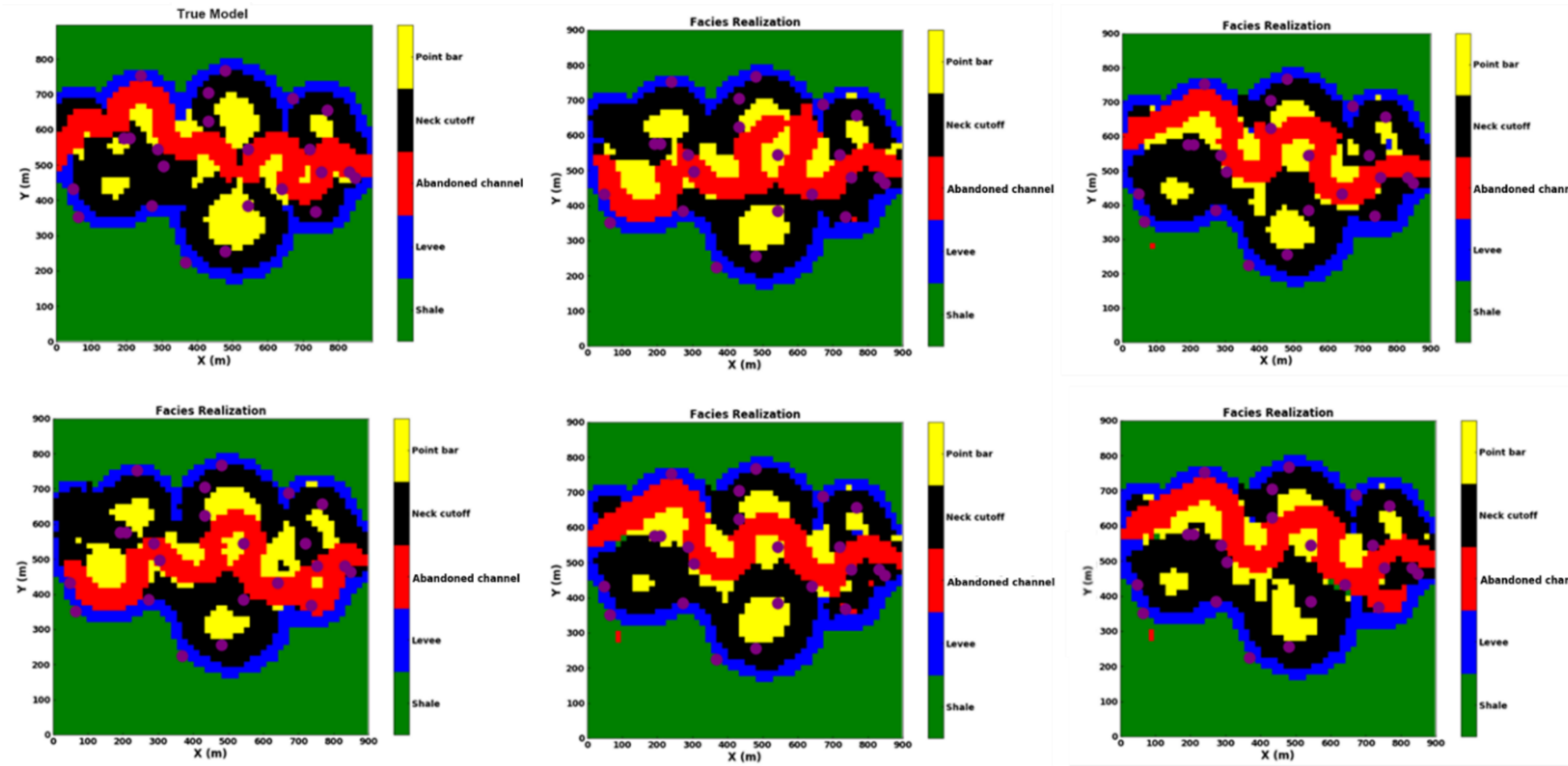

Figure 3.11: Realizations with fixed channel and levee widths and neck cutoff threshold conditioned by both seismic and well-log interpretations. Purple dots identify the location of wells. Realizations match the outline of the true model and geometries of different facies are preserved. Compared to the realizations conditioned to seismic interpretation only, realizations conditioned to both well log and seismic interpretation exhibit less variation in facies distribution. The abandoned channel has large variations only in places where few wells are drilled, e.g., where "near X" equals 100m and 500m.

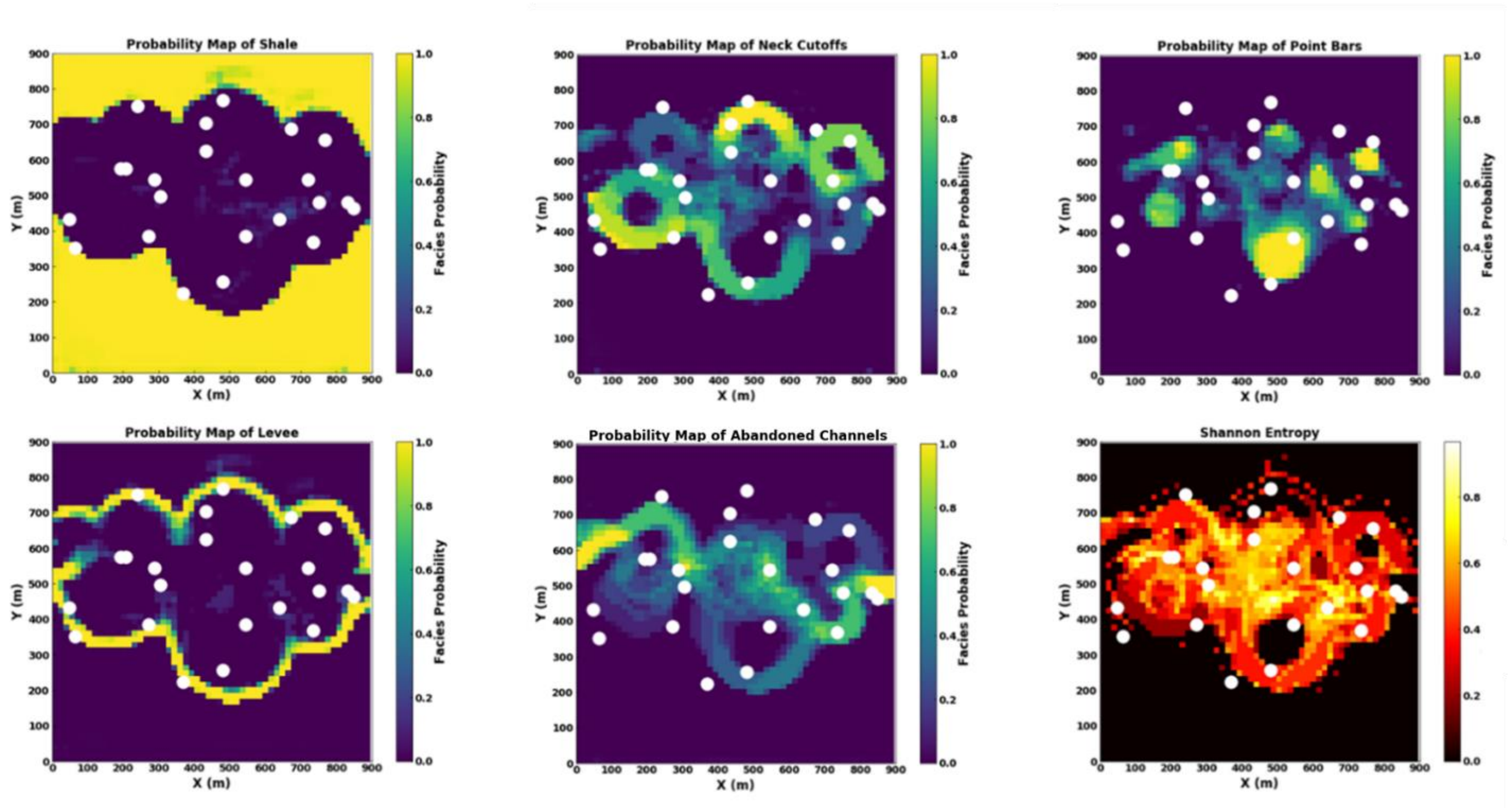

Figure 3.12: Probability map and Shannon entropy map for different facies with fixed channel and levee widths (conditioned to both well-log and seismic interpretations). White dots identify well locations. Similar to probability maps generated from realizations conditioned to seismic interpretation only, small variations are observed in shale and levee distributions. Well-log interpretation provides additional information on facies distribution within sand bodies. The abandoned channel is more likely to be located at the center of the sand body, which is consistent with the true model. Less uncertainty is observed in the Shannon entropy map. Shannon entropy at well locations is small.

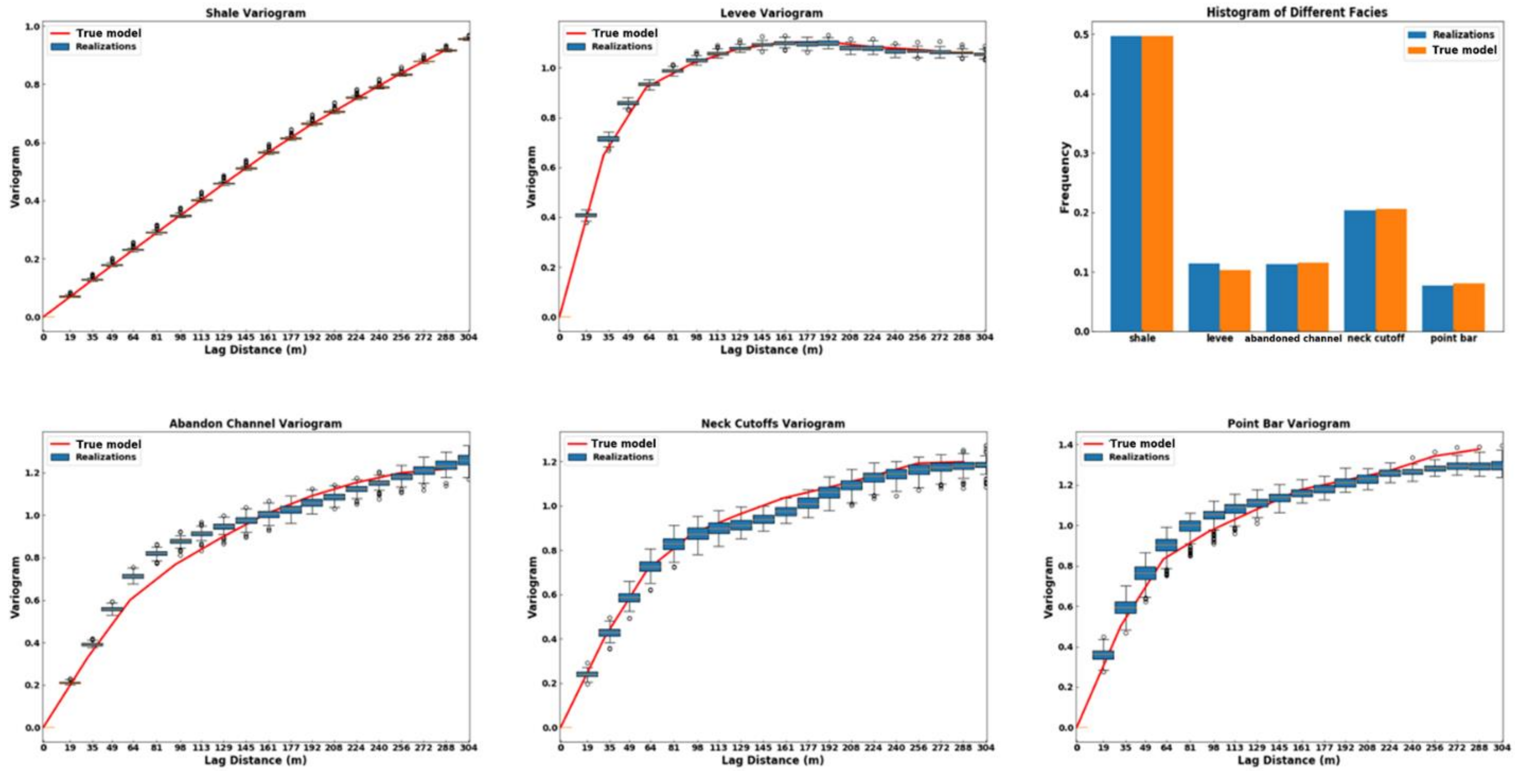

Figure 3.13: Variograms and histograms for different facies (conditioned to both well-log and seismic interpretation). Compared to the variograms of realizations only conditioned to the seismic data, well-log information improves the match of the variogram for different facies. Facies within the sand body also yield a better histogram match with the true model.

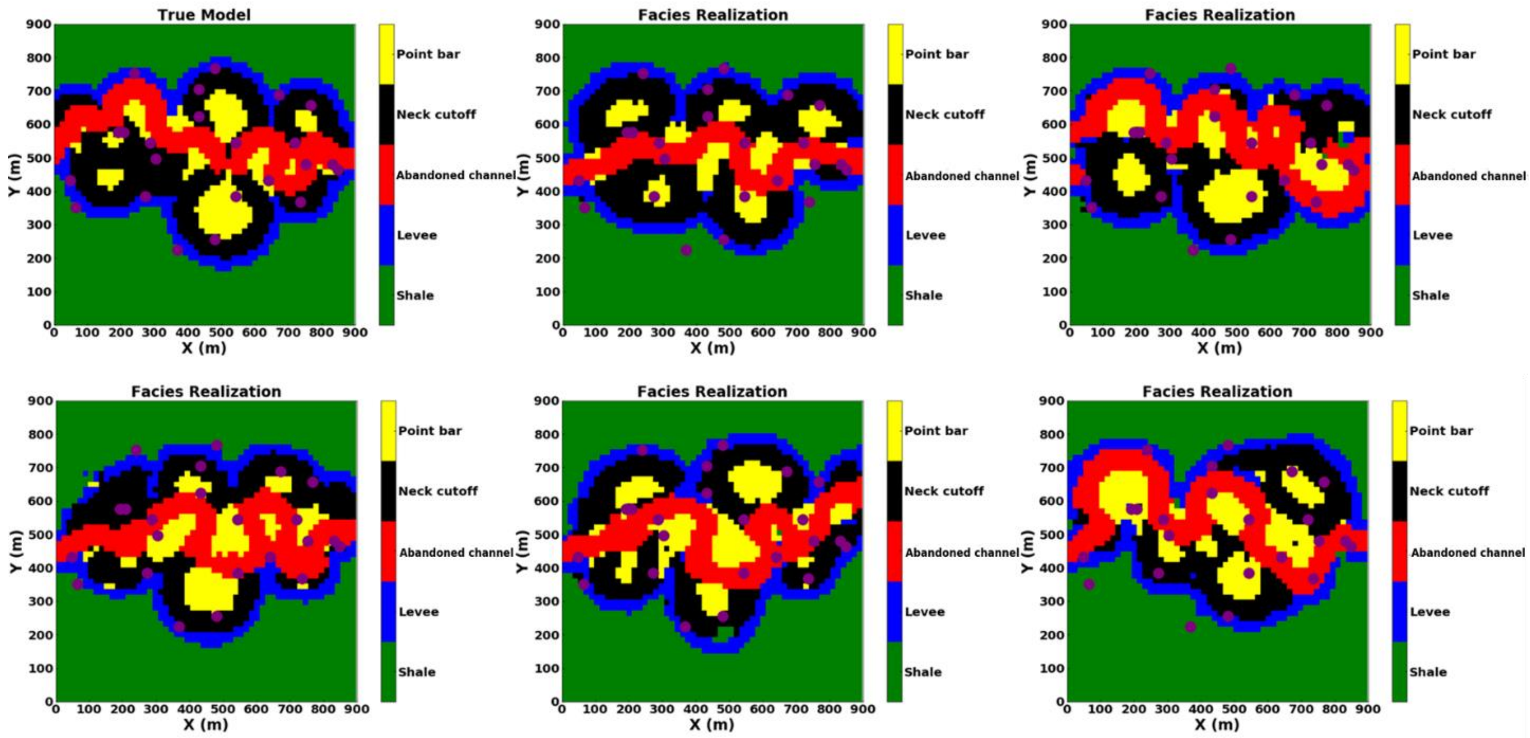

Figure 3.14: Realizations conditioned to upscaled seismic interpretation with large uncertainty. Larger variations are found in the distributions of different facies; however, the patterns for each facies are reproduced.

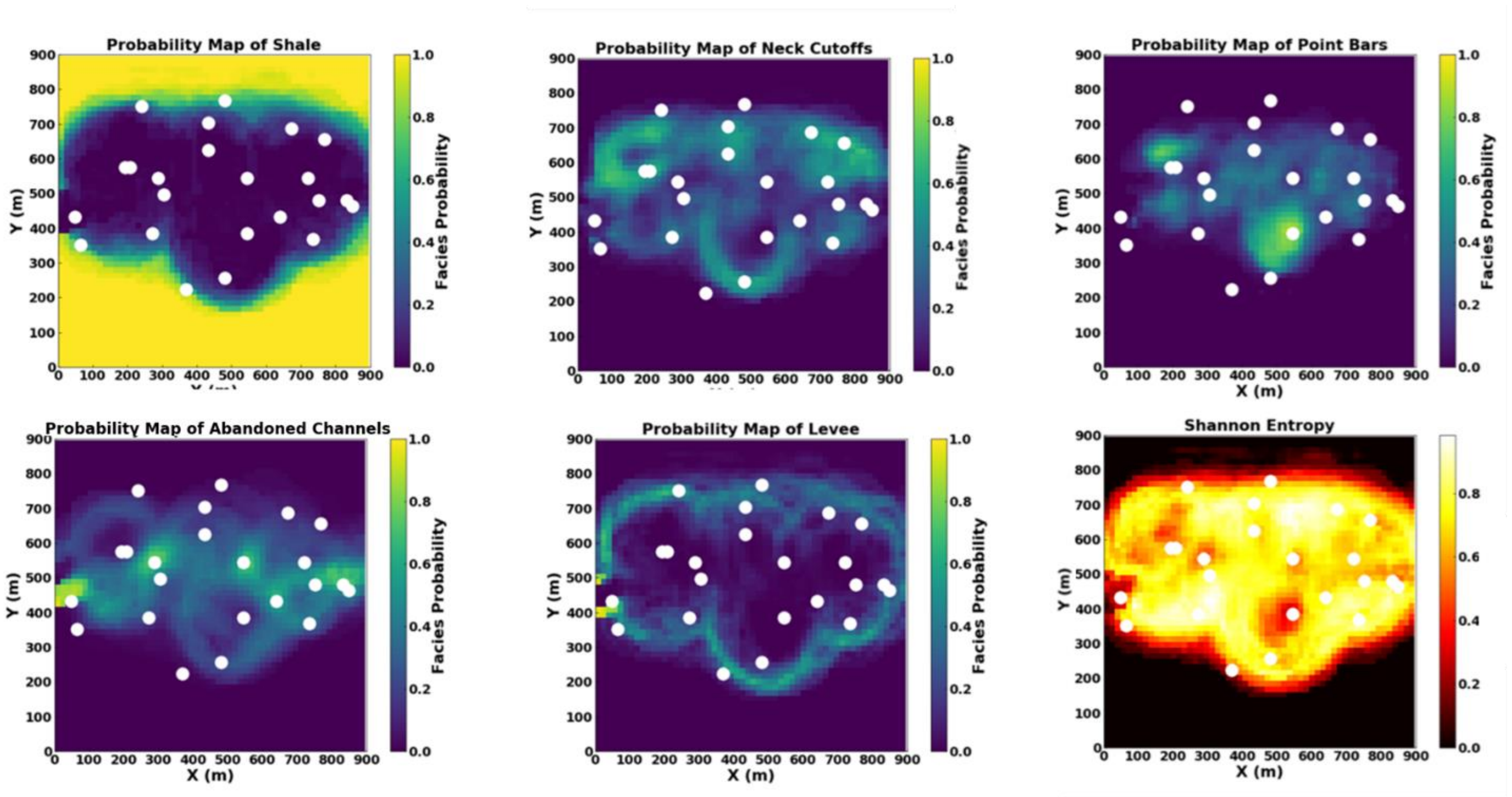

Figure 3.15: Probability maps for different facies and Shannon entropy map. Given the high uncertainty in seismic interpretation and the absence of well-log interpretation, one can no longer distinguish potential facies distributions from the probability maps. However, the general trend can still be observed.

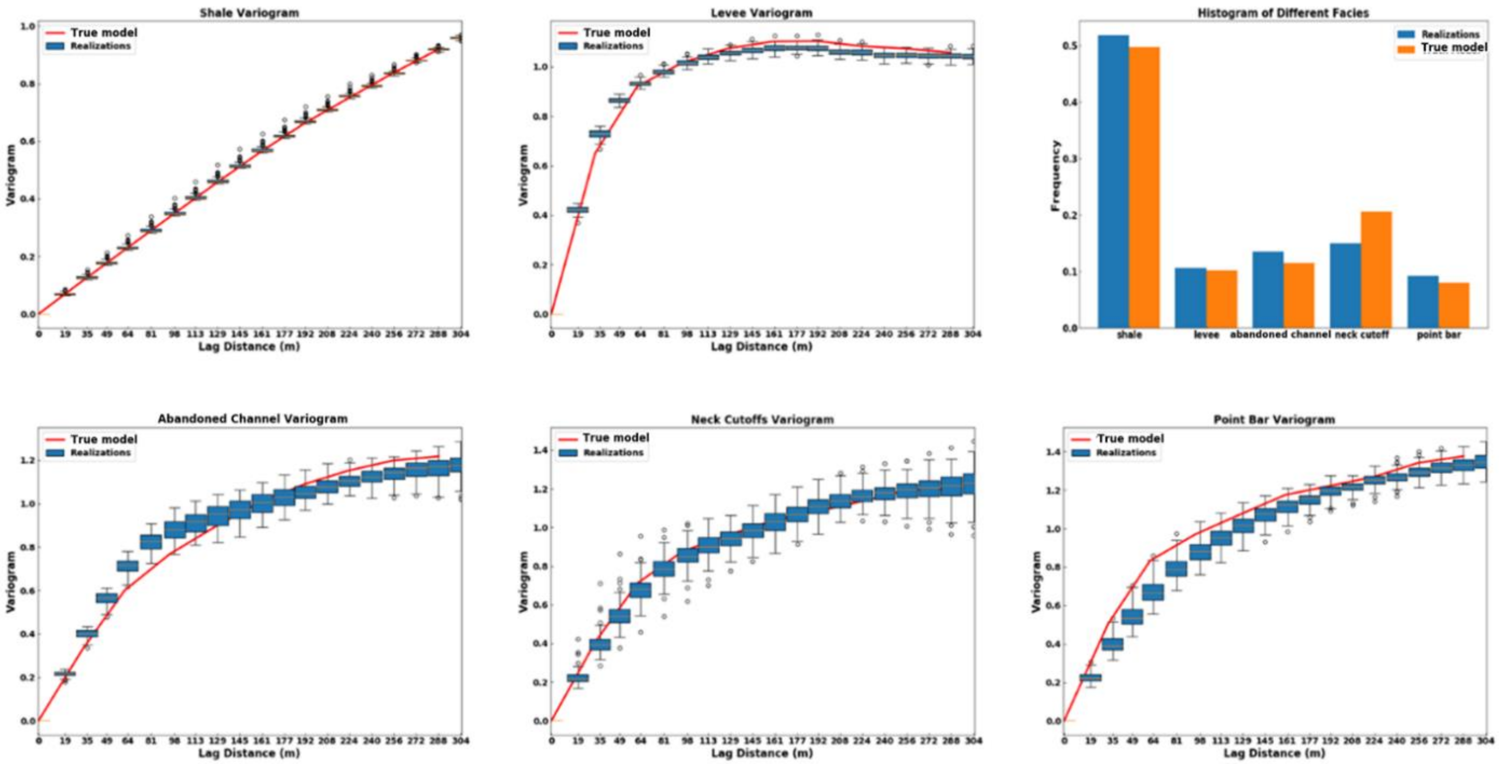

Figure 3.16: Indicator variograms and histograms of different facies in reservoir model realizations conditioned to high-uncertainty data. Histograms show that realizations underestimate the proportion of neck cutoff facies and overestimate the proportion of the other facies; the variograms of the neck cutoffs, shale and levee facies are within 25% quantile of the realizations, and the variograms of point bar and abandoned channels are within 75% quantile. Variograms of realizations show larger variation than realizations conditioned to low-uncertainty data.

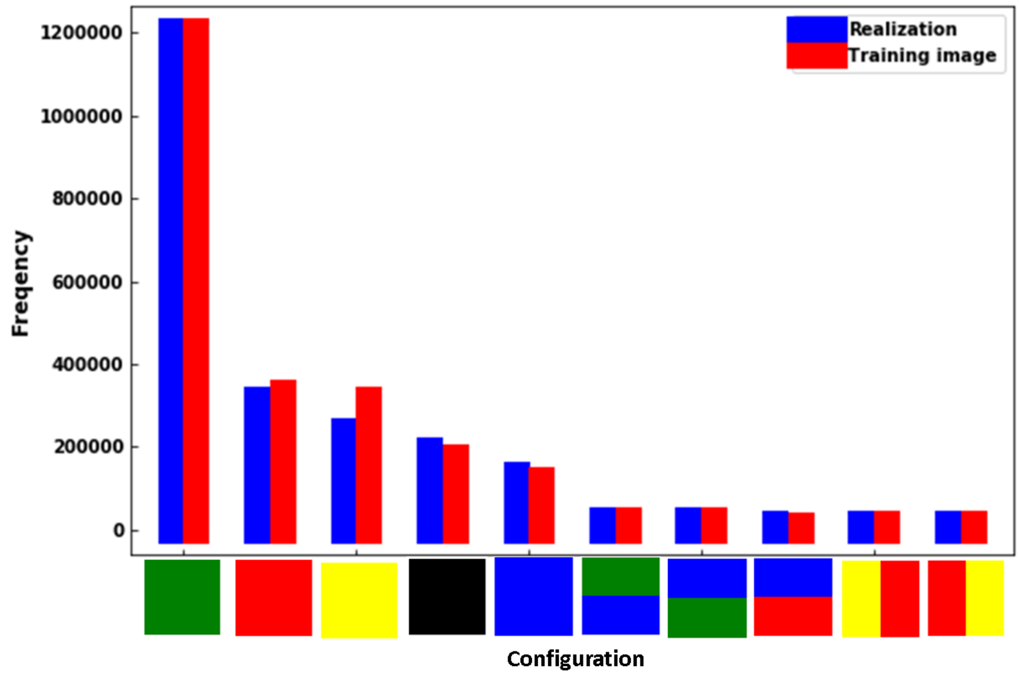

Figure 3.17: Multiple point density function (4-point template) comparison between training image and realizations. Configurations are made of shale (green), active channel (red), point bar (yellow), neck cut-off (black), and levee (blue) facies.

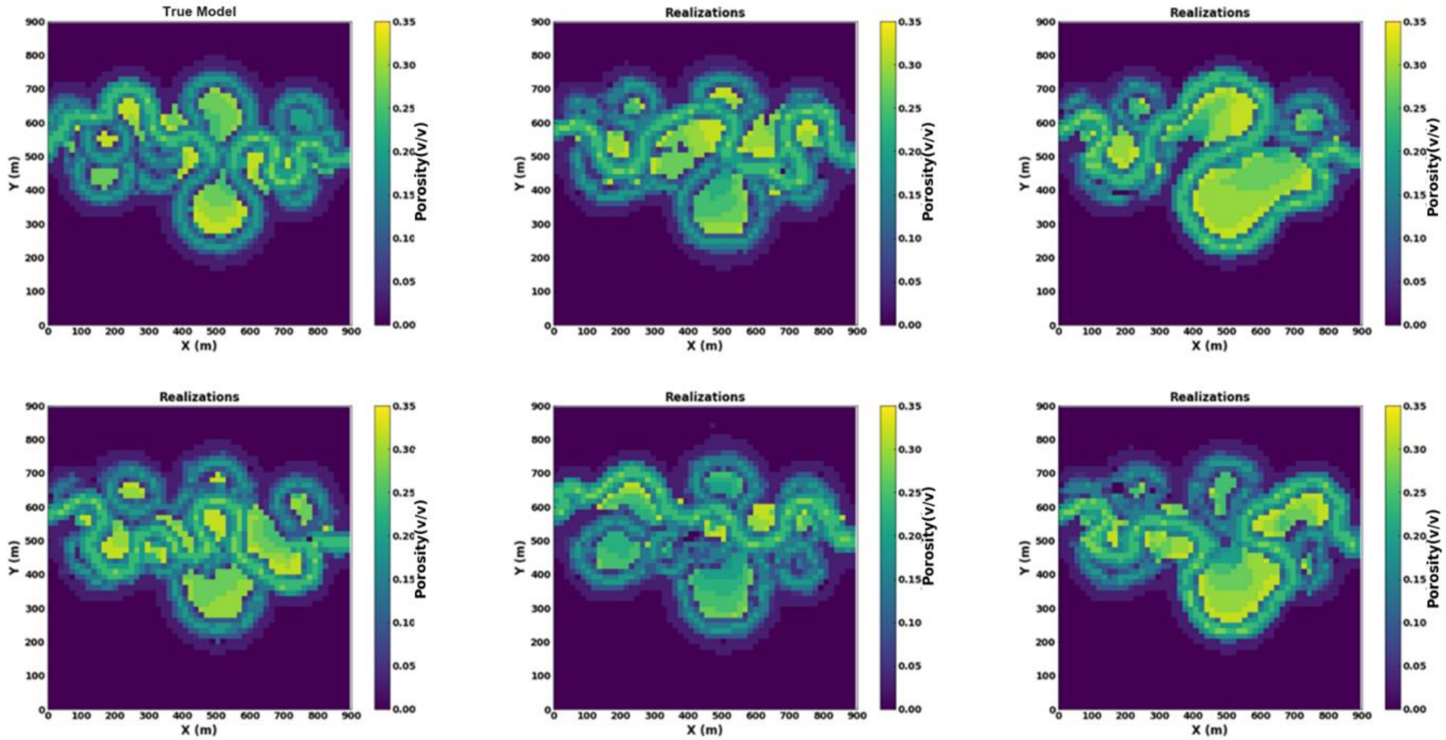

Figure 3.18: Property realizations generated from the facies model. Realizations successfully reproduce the trend of property distributions within each facies.

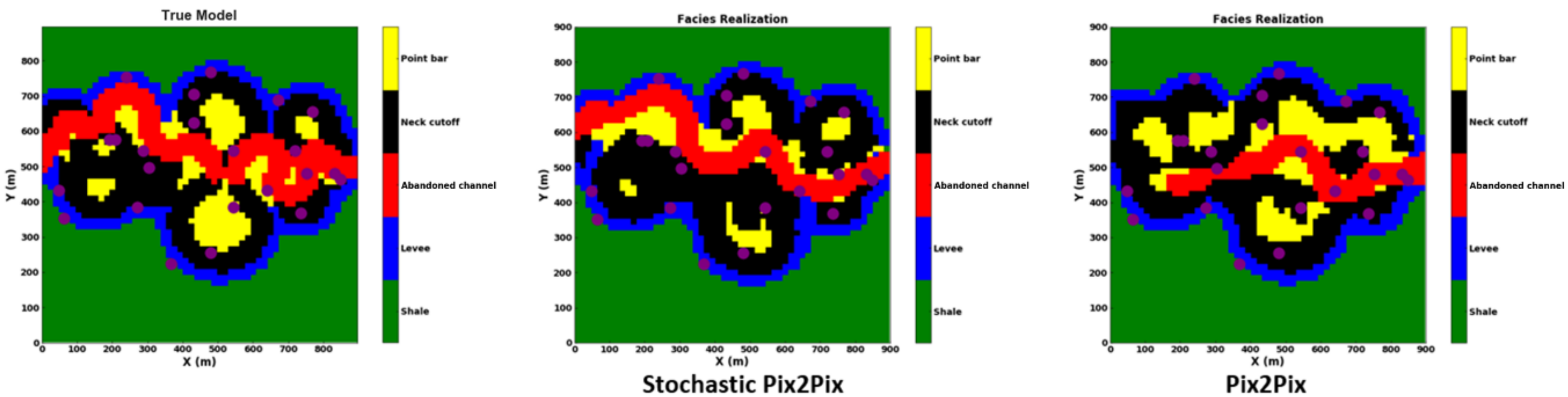

Figure 3.19: Comparison between maximum likelihood estimates obtained from the stochastic pix2pix and pix2pix methods. Realizations generated with the stochastic pix2pix method exhibit a better match with the seismic interpretation; they also reproduce the long-range patterns of different facies better than does pix2pix.

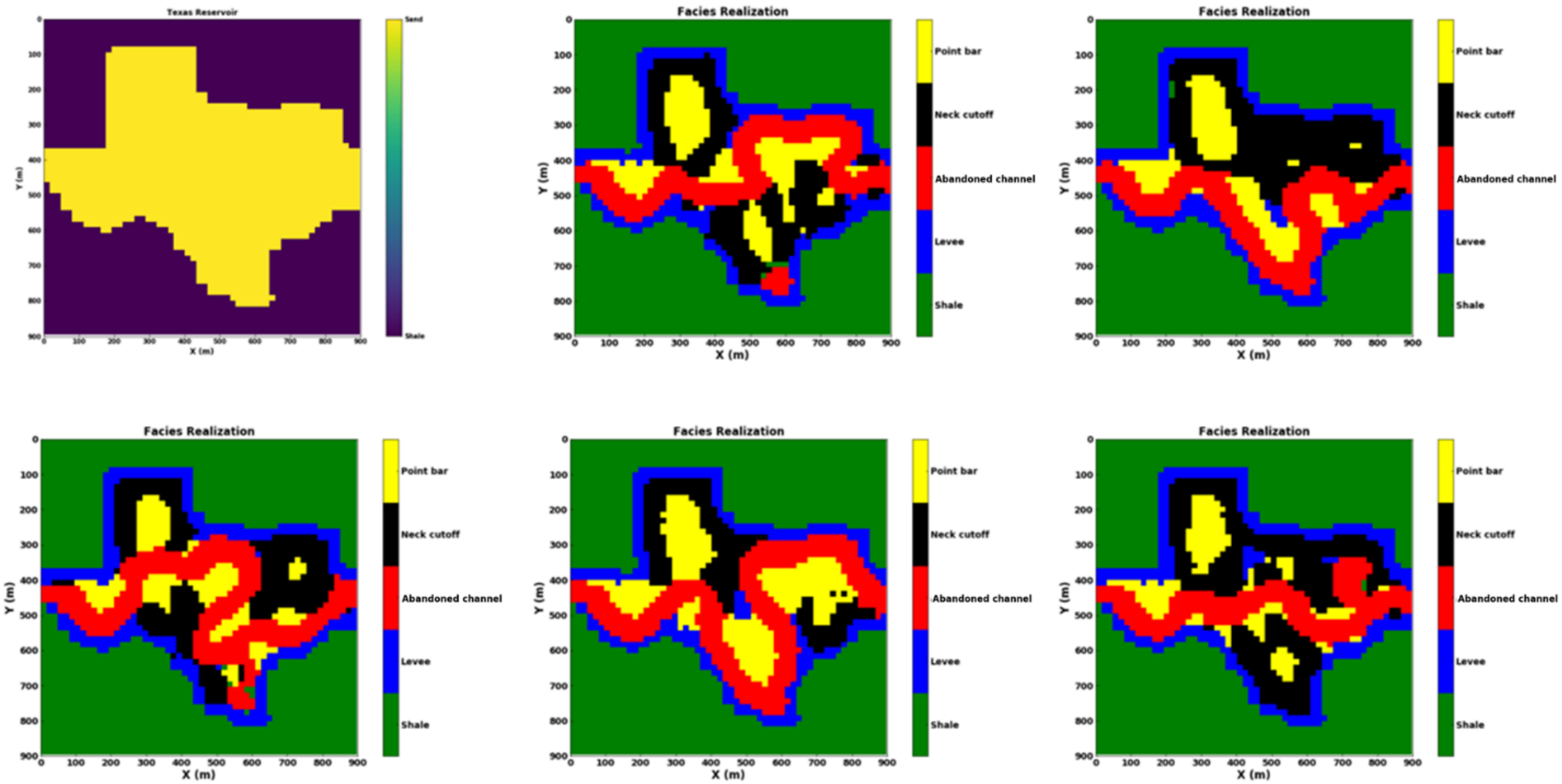

Figure 3.20: Realizations generated from the map of Texas. Although the shapes of the shaly facies and sandy facies are very different from those of training images, my method still reproduces the patterns of each facies observed in the training images.

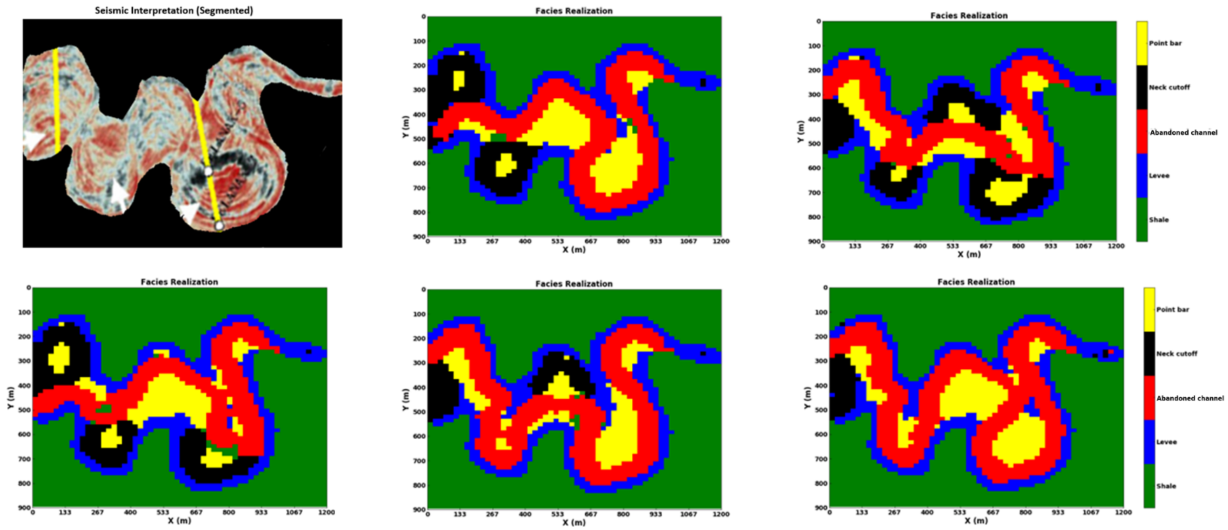

Figure 3.21: Realizations generated from the interpretation of field seismic data (Kolla et al., 2007). It is worth noting, similar to figure 20, only the outline of the seismic interpretation (binary facies map) is used as a constraint for new realization generation. Sandy facies are well reproduced, and the facies distribution also exhibits sufficient variability. Patterns of facies are reproduced; neck cutoffs tend to happen when channels intersect themselves.

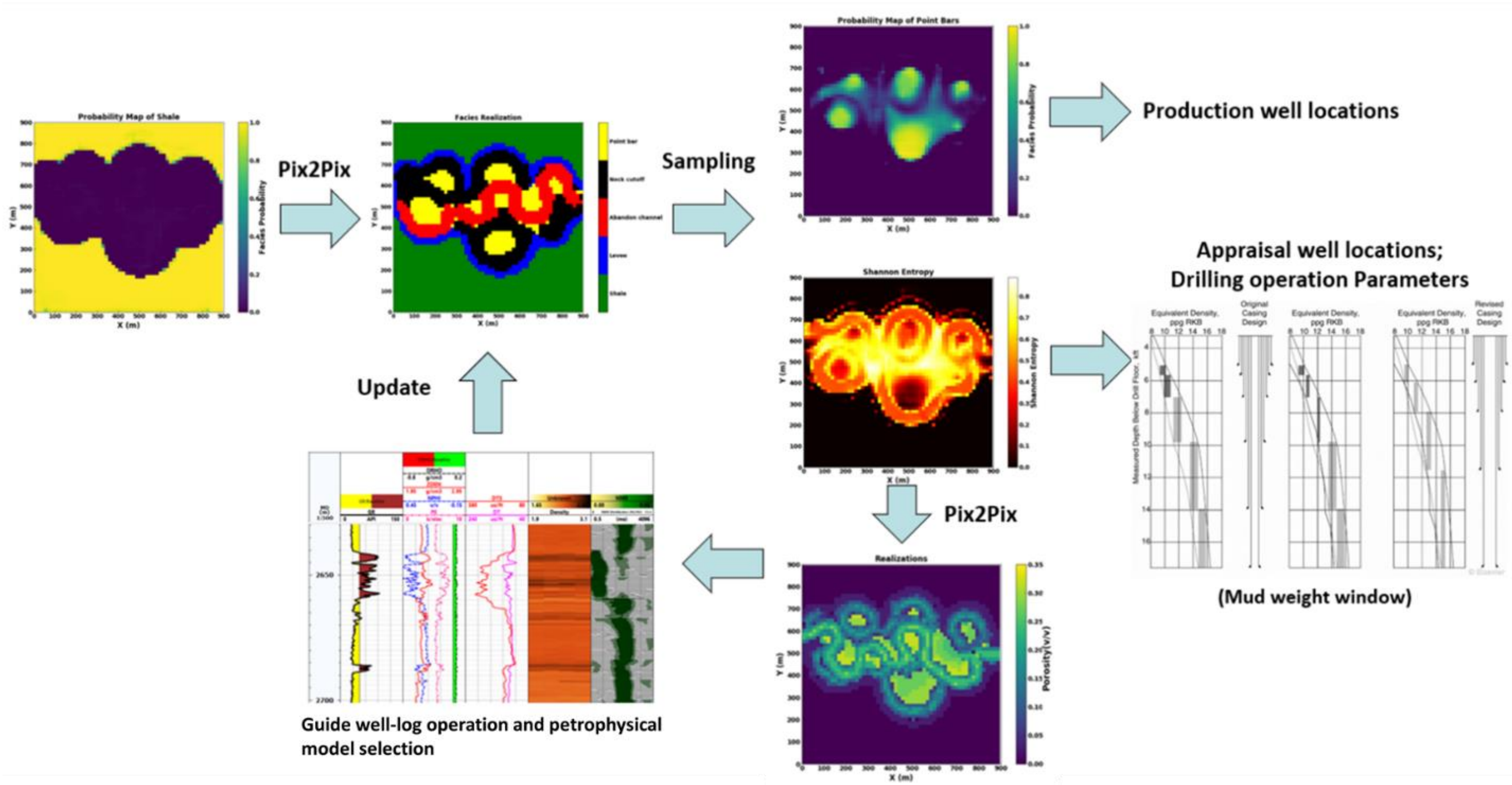

Figure 3.22: The stochastic pix2pix method for real-time reservoir management. Seismic interpretation is used to generate possible reservoir models; these models are then used to generate probability and uncertainty maps. The maps can be employed in well planning and pre-drilling assessment, and they can also help petrophysicists to optimize the parameters used in their models. History matching in reservoir model subspace is also facilitated where all reservoir models have already been conditioned to geophysical/petrophysical interpretations.

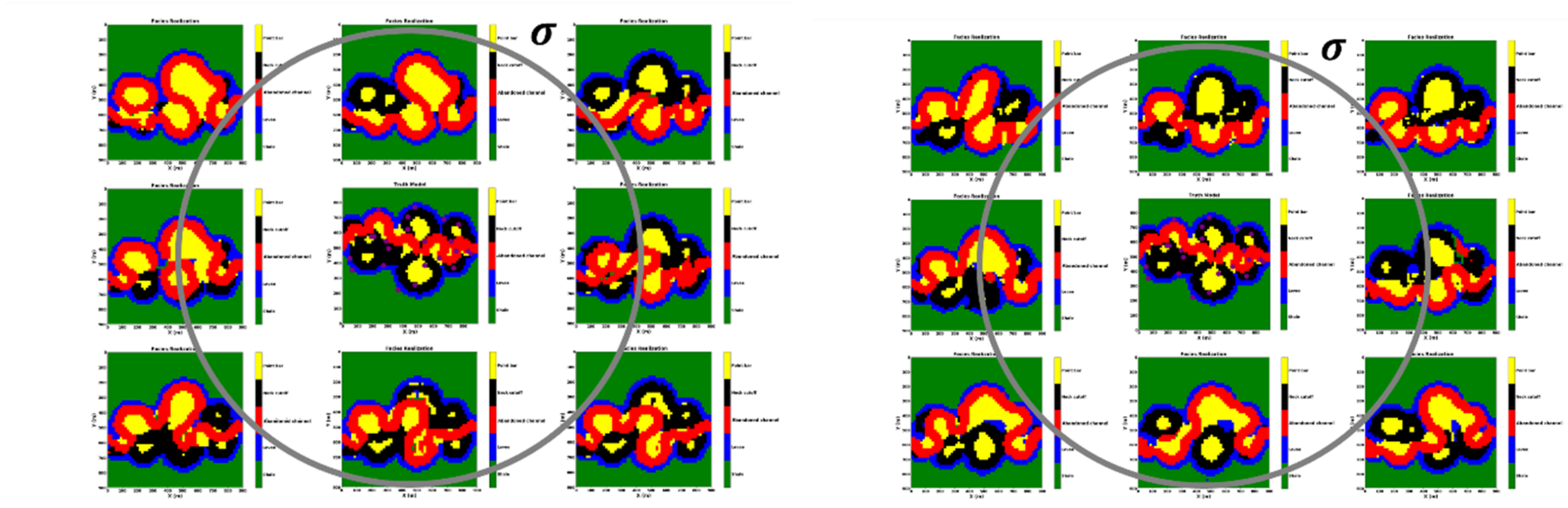

Figure 3.23: Two instances of continuous mapping from Gaussian random variables to realizations. The realizations change continuously as the Gaussian random variables change using the gradual deformation method. The continuous deformation of active (abandoned) channel fill is similar to the migration of a real meandering channel, in that point bars and neck cutoffs tend to be generated whenever the channel intersects itself. One can interpret this as the machine successfully understanding the channel migration process.

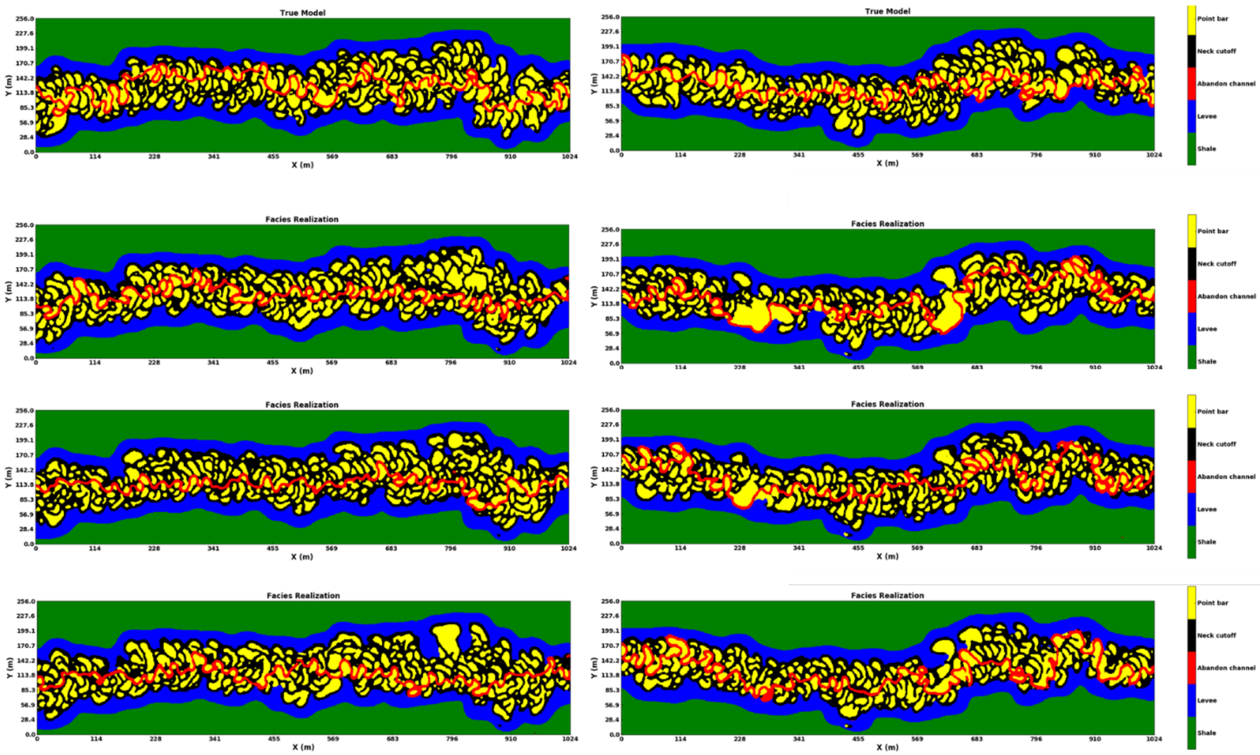

Figure 3.24: Generation of large-scale complex turbidite reservoir models. The realizations reproduce the patterns in the corresponding true models, such as continuous channel fill, neck cutoffs indicating the left-to-right flow direction, and levee filling the rest of the confining canyon. This indicates that the stochastic pix2pix method can be applied for large-scale 2D stochastic reservoir modeling and can be extended to 3D modeling by modeling each zone with different seismic/well data constraints.

Chapter 4: Hierarchical Modeling of Deepwater Lobate Reservoir via Machine Learning Methods

Unconfined deepwater lobe deposits are among the most important targets in deepwater oil field exploration and production. Accurate stochastic simulations of the sedimentary architectures and petrophysical properties of deepwater lobe deposits require robust seismic and well data integration. The reservoir heterogeneity at scales below seismic resolution generally exhibits important and predictable hierarchical architectures that control the vertical and horizontal connectivity of the reservoir, affecting the hydrocarbon recovery rate during development. Current geostatistical simulation algorithms such as variogram- and multiple-point-based methods readily perform property modeling conditioned to well data and trends informed from seismic data at and above seismic resolution. Yet, these common geostatistical models are limited in their ability to reproduce essential, multiscale heterogeneities below seismic resolution between wells, including nested multiscale architectures and trends. Rule-based methods are commonly used for modeling the hierarchical architectures but conditioning the models to well logs and seismic data is still limited, difficult, and time-consuming. Either a prohibitive degree of expert intervention is employed resulting in overly deterministic models or the common 'cookie cutter' approach is applied, resulting in inconsistency over the multiple scales.

To address the well and seismic data conditioning and multiscale modeling limitations of current geostatistical modeling methods, I propose a new workflow based on the hierarchical application of the newly developed stochastic pix2pix machine learning algorithm. The hierarchical stochastic pix2pix workflow calculates a diverse ensemble of conditional, multiscale architectural, and petrophysical property model realizations by learning the stacking and geometrical patterns of architectural elements in rule-based deepwater lobe deposit training models. I demonstrate the hierarchical stochastic pix2pix workflow to calculate an ensemble of multiscale deepwater lobe depositional systems conditioned by: (1) geostatistical rule-based training and testing models, (2) bounding surfaces, and property estimates from seismic and well log interpretations.

With the hierarchical stochastic pix2pix workflow I can efficiently and accurately calculate diverse 3D reservoir models, which are conditional to the well-log and seismic interpretations, and reproduce multiscale heterogeneity. I also use quantitative measures, such as a raster-based compensational index and the dynamic Lorenz coefficient to validate the model accuracy. In addition, the reduced model parametric representation and efficient model calculation available with the hierarchical stochastic pix2pix workflow is critical to the practical solutions to reservoir inverse problems.

4.1 Introduction

Accurate reservoir models are essential for developing subsurface forecasts to support subsurface development decision-making to maximize project value, steward vital energy resources, and minimize environmental and safety risks. An accurate reservoir model complies with three conditions: (1) an exact match of the well-log interpretations at well locations, known as well conditioning, (2) conformity to bounding surfaces and informative attributes from seismic interpretation, known as seismic conditioning, and (3) consistency of geological concepts, such as the spatial and temporal order, geometries of sedimentary elements, and the patterns of petrophysical property distribution of sedimentary elements at different scales. These models must be calculated efficiently to provide an ensemble of realizations that jointly represent subsurface uncertainty.

Current geostatistical methods, such as two-point semivariogram-based or multi-point, integrate spatial statistics inferred from available conditioning data, training images, and analog information sources, such as outcrops and mature fields. These methods are unlimited in their ability to condition to well data, (Pyrcz and Deutsch, 2014) but tend not to reproduce single scale, nor multiscale subsurface heterogeneity, representing salient fluid flow conduits, barriers, and baffles such as curvilinear channels, undulating drapes, and specific facies ordering relationships (Pyrcz et al., 2012).

Stochastic object- and rule-based geostatistical methods reproduce complex multiscale subsurface heterogeneities by filling the reservoir model with nested, parameterized architectural elements of appropriate shapes and dimensions according to a set of user-defined geometric parameters and rules (Pyrcz, 2004; Deveugle et al., 2014). Rule-based methods utilize probabilistic rules that mimic sequential depositional processes to better reproduce patterns resulting from the depositional process, such as stacking patterns and geometries of depositional elements. When I perform rule-based modeling for lobe deposit, I assume stationary depositional patterns and geometry of architectural elements, which may not be valid when the depositional environment changes. Depositional elements are sequentially and stochastically generated and deposited to generate the model. The deposition of the elements follows a set of rules so that depositional elements are more likely to deposit on elevation lows. However, well and seismic conditioning for surface- and object-based models is difficult because the feedbacks and interactions between the placed multiscale architectural elements hinder the forecasting and optimization parameter selection for well and seismic conditioning (Pyrcz, 2004; Michael et al., 2010; Bertoncello et al., 2013; and Wang et al., 2018). Seismic conditioning is the process of calculating reservoir models with architectural elements that are consistent with architectural element surfaces and horizons interpreted from seismic data. Zhang et al. (2009) demonstrate rule-based modeling of deepwater lobes to form a lobe complex. However, the bounding surface of the lobe complex is not used as a constraint for the modeling of lobes.

Due to the limitation of current modeling methods, researchers resort to machine learning-based approaches (Santos, et al., 2021) to calculate more accurate reservoir model realizations with good well, seismic, and multiscale geological concept conditioning. Most of the machine learning-based methods are based on generative adversarial networks (GAN) (Goodfellow et al., 2014). In a GAN, two neural networks, the generator and the discriminator, compete to stochastically calculate reservoir model realizations reproducing patterns in training images. As with current geostatistical methods, these GAN model realizations are calculated by varying the image generation random number seed. The GAN uses convolutional neural networks to extract high-order statistics about the geometric and depositional patterns of architectural elements in training models and stochastically calculate new model realizations by varying random latent variables (Goodfellow et al., 2014). GAN-based methods have been successfully applied to build more accurate reservoir models, for example, Chan and Elsheikh (2017) demonstrate that the GAN-based method yields improved channel reservoir model realizations over the principal-component-analysis-based method; Laloy et al. (2018) calculate GAN-based unconditional (without well conditioning) channel reservoir models and apply the models to solve a hydraulic inverse problem; Dupont et al. (2018) use semantic inpainting method to perform soft well conditioning and Jo et al. (2019) perform well conditioning for GAN-based models by filling void regions near wells with inpainting methods. However, current well conditioning methods may introduce spatial artifacts especially when the conditioning data are dense relative to the scale of spatial continuity, and may underestimate the spatial uncertainty around the well, because of the lack of spatial uncertainty in Convolutional Neural Network (CNN) output. Seismic conditioning and multiscale sedimentary architectures are not considered in previous publications, and the statistics applied to assess the reproduction of multiscale geological concepts in the realizations may not fully capture the geometric and depositional patterns of architectural elements at different scales.

To improve well and seismic conditioning, Pan et al. (2020) propose the stochastic pix2pix method that incorporates the seismic and well conditioning as additional loss terms during the training of the GAN model. With this method, they successfully calculate realizations of fluvial channel models with good well, seismic and single-scale geological concept conditioning. However, a large weight for the well conditioning can potentially cause the mode collapse problem (Zhang, 2018), which refers to the lack of diversity in the realizations, resulting in an unrealistically low level of spatial uncertainty between wells and in the model forecasts. To avoid the mode collapse caused by well conditioning, and exactly reproduce well data, a skip connection is added to the generator (Figures 4.21 and 4.22).

Deepwater reservoirs often exhibit multiscale geological features, including distinct spatial trends, orientations, and geometries of architectural elements at different scales, as well as relationships between each scale, such as architectural confinement (Sullivan et al., 2000; Abreu et al., 2003; Sullivan et al., 2004; Deptuck et al., 2008; Prélat et al., 2009; and Zhang et al., 2016). Many hierarchical schemes have been proposed to characterize the deep-marine sedimentary architecture (Groenenberg, et al., 2010; Cullis et al., 2018), for example, Mutti and Normark (1987,1991) identify five main orders of scale for turbidite deposits based on the timescales reflected by each order; Pickering et al. (1995) classify the sedimentary architecture into seven orders based on the facies, geometries, and bounding surfaces of sedimentary elements at different scales; Prélat et al. (2009) define four hierarchical orders for distributary deposits based on the recognition of bounding surfaces identified by fine-grained deposits between sand-rich bodies. Cullis et al. (2018) compare different sedimentary architecture classification methods and summarize the common nomenclatures and definitions used to define the hierarchical architecture of deep-water deposits. The hierarchical schemes proposed by Cullis et al. (2018) are adopted in this chapter. According to Cullis et al. (2018), in lobe deposits (Figure 4.1), we can often identify four hierarchical divisions: 'bed', 'lobe element', 'lobe', and 'lobe complex'. A 'bed' is the smallest building block of a lobe deposit, which is interpreted as the product of a single depositional event. 'Beds' separated by non-erosional surfaces, are stacked with little lateral offset into a higher hierarchical division termed the 'lobe element'. Genetically related 'lobe elements' bounded by thin (<2 cm thick) siltstone intervals, stacked with small offset (~500 m, Deptucket al., 2008) within topographic lows generate lobate or lenticular geometries, termed 'lobe'. Compensational stacking of genetically related 'Lobes' bounded by muddy intervals 0.2-2m thick forms the 'Lobe complex'. 'Lobe complex' is commonly bounded by basin-wide claystone intervals that are >50 cm thick (Cullis et al., 2018).

Performing accurate uncertainty quantification for architectural elements that are unresolvable by the conventional seismic survey is important for the characterization of the deepwater deposit. However, current reservoir modeling workflows are limited in their ability to capture these features, most workflows rely on a 'cookie-cutter' approach that omits important relationships between scales. In the cookie-cutter approach, I break the model into subsets and then populate reservoir properties in each subset separately and then recombine (e.g., geostatistical facies-based models). This often results in discontinuities are subset boundaries. For example, in Figure 4.2, with the cookie-cutter approach, small-scale lobes identified with upward decreasing porosity trends are calculated over a larger domain independently, and then "cut out" and placed into a lobe complex. Consequently, the lobes are not stacked within a lobe complex consistent with the lobe complex geometry, scale, and bounding surfaces. This inability to build multiscale, hierarchical models may impact the accuracy of flow forecasts near the bounding surfaces. Figures in this chapter are vertically exaggerated (VE) for better visualization.

To further address the problems, I propose a new recursive, multiscale modeling workflow, known as the hierarchical stochastic pix2pix, based on the stochastic pix2pix method (Pan et al., 2020) coupled with an automatic segmentation method for the construction of the consistent, conditional, multiscale deepwater lobe deposit model realizations, including bed, lobe element, lobe and lobe complex models. The stochastic pix2pix method is derived from the pix2pix method (Isola et al., 2017) to perform low-resolution to high-resolution image mapping. While the pix2pix method is deterministic, the stochastic pix2pix method is stochastic by introducing an additional loss function to force model realizations to reproduce low-resolution images (Pan et al., 2020). The model realizations are validated with new spatial statistics to quantify the reproduction of spatial and temporal distribution and the geometries of sedimentary elements at different scales within the lobe complex. I efficiently calculate practical and more accurate subsurface uncertainty models through a suite of model realizations, to support improved development decision-making. The Method section provides more details on how to apply hierarchical stochastic pix2pix for multiscale lobe system modeling and the methods for model validation.

4.2 METHOD

In this section, I describe: (1) the proposed hierarchical stochastic pix2pix workflow for consistent conditional reservoir modeling for a lobe complex, (2) the calculation of training models and different machine learning methods used in the workflow for conditional reservoir modeling, (3) the metrics used to validate the models with respect to well, seismic, multiscale geological concept conditioning and uncertainty representation of the ensemble of model realizations calculated with the hierarchical stochastic pix2pix workflow.

4.2.1 Hierarchical Stochastic Deepwater Lobe Deposit Modeling

As with current hierarchical reservoir modeling workflows, the proposed hierarchical stochastic pix2pix workflow constructs model realizations from the largest to the smallest scale, and stochastic architectural models are first simulated and used to parametrize the reservoir model, and the lithology and petrophysical property model are then calculated conditioned on the simulated architectural model. In this chapter two architectural elements, lobes, and lobe elements are modeled within a lobe complex.

It is difficult to conditionally simulate the bounding surfaces of architectural elements of an uncertain number at different scales with machine learning models. To avoid direct simulation of the surfaces, lobes and lobe elements are identified by ordered beds, with the associated index increasing from the top to the bottom. The term 'bed' used to identify the lobe is not the architectural element 'bed' but a parameterization, it does not have a geological meaning. With this parameterization of lobes and lobe elements, we can simulate the bed index of each voxel in the model instead of bounding surfaces with the stochastic pix2pix method. The bounding surfaces and geometries of lobe and lobe elements are then calculated with a hierarchical segmentation method based on the distribution of the beds. Finally, petrophysical property patterns, e.g., fining upward, thickening upward, and lateral trends, are stochastically simulated for the hierarchical architectural elements with classical geostatistical methods. The architectural elements identified at well locations are transformed to bed index as constraints for modeling. Rock quality of lobe and lobe elements generally decreases from the base to the top; adjacent lobes and lobe elements are separated by shale drapes at the top of lobes and lobe elements; the base of a lobe/lobe element with high rock quality contacts with the top of a lobe/lobe element with low rock quality. Therefore, bed indexes can be used to represent the rock quality trend and assist segmentation of lobe and lobe elements from lobe complex and lobe respectively.

The workflow steps for the specific case of modeling of lobe and lobe elements within a lobe complex are illustrated in Figure 4.3 and enumerated here:

1) Specify the container (lobe complex) identified by the top and base bounding surfaces and the bed-index representation of lobe identified at well locations as the inputs (A) for the stochastic pix2pix model. The bounding surfaces are either horizons identified from well and seismic data, or the outlines of the simulated lobe complex. A maximum number of eight beds are allowed to identify a lobe at a well location.
2) Apply stochastic pix2pix model to simulate bed indexes (B) identifying lobes, conditioning to the well data and top and base bounding surfaces of the lobe complex.
3) Identify lobes (C) based on the distribution of bed index with a segmentation workflow of sequential application of the Density-Based Spatial Clustering of Applications with Noise (DBSCAN) method (Ester, et al., 1996).
4) Using the same methods in steps 1-3 with the lobe bounding surfaces (C) from step 3 and the bed-index representation of lobe elements identified as new constraints to simulate bed index within lobe elements (D) and define lobe

elements (E).

5) Calculate lithology and property model realizations (F). Linear models between the bed index and petrophysical properties in lobes and lobe elements are fit based on well data with the coefficients and residuals of the linear models treated as spatial random functions and stochastically co-simulated across the reservoir with Gaussian geostatistical simulation (Pyrcz and Deutsch, 2014). lithology and property models are simulated from the largest lobe scale to the lobe element scale and finally the grid-scale. At the lobe and lobe element scale, models are parameterized as beds. Simulated lithology and properties at a large scale are used as the prior information for the simulation of fine-scale models. When seismic attributes, such as acoustic impedance or seismic facies are available, they can also be incorporated into the conditional simulation as soft conditioning data (Pyrcz and Deutsch, 2014).

The proposed workflow stochastically models architectural elements and associated petrophysical properties from lobe scale to lobe element scale; however, if high-resolution seismic interpretation with mapped lobes is available, the second half of the proposed workflow can be used to integrate the mapped lobes as deterministic constraints to model the lobe element distribution.

Lobe-element features and associated correlations may be inferred from existing reservoir data and analogs such as high resolution, shallow seismic, outcrop, and mature reservoir studies. When there is significant uncertainty, I recommend the use of ranges of these model parameters (Table 4.1) to integrate these uncertainty sources. A scaling factor is applied to the length parameters of lobes to obtain those of lobe elements. In this case, the size of the reservoir model is scaled such that the length parameters of lobe elements are one-half of those of lobes. In this chapter, the extent of models at different scales is fixed to be 50 km×50 km×50 m, the gridding of the lobe scale model in this chapter is 56×56×56 voxels and the gridding of lobe element scale model is increased to 112×112×112 voxels with the lengths of voxels halved for a better illustration of the added details.

4.2.2 Training Model Set Calculation

A Python, rule-based deepwater lobe model simulator (UTLBPY) based on the algorithm proposed by Jo and Pyrcz (2019), is applied to calculate the training models for training the stochastic pix2pix model. I use the UTLBPY to simulate training models with probabilistic, depositional rules, which mimic the compensational stacking of lobes. The geometrical parameters applied in the training model calculation are shown in Figure 4.4, and the ranges of the geometrical parameters of the lobe are summarized in Table 4.1. Lobes and lobe elements are defined by the height (H), radius (R), aspect ratio (b), orientation (φ), and healing factor (m) parameters as discussed in Jo and Pyrcz (2019). To apply this workflow to calculate reservoir model realizations for actual fields, geometries of the architectural elements at different scales should be based on local interpretation of conditioning data and available analog information, e.g., well log correlation and outcrop analog. The distribution of aspect ratio, orientation, and healing factor are assumed to be within the same range over lobe and lobe element scales. The output of the UTLBPY simulator is a lobe scale architectural model (Figure 4.5) identified with eight beds. The diverse ensemble of rule-based models provides sufficient training for the workflow and represents geological concept uncertainty.

To train and validate the stochastic pix2pix model, I calculate 1100 rule-based lobe scale architectural models (Figure 4.5) with UTLBPY, 1000 of the models are applied as the training set, while the other 100 models are withheld as the test set. 30 to 65 lobes are stacked to form a lobe complex with variable bounding surface geometries. These lobe scale training models are sufficient to train stochastic pix2pix models for modeling multiscale reservoirs recursively because I assume a linear relationship between the length parameters of architectural elements at different scales, and the depositional patterns are similar. A simple linear relationship is assumed for this demonstration but can be updated for any deepwater setting. However, if the geological concepts vary over the multiple scales, different stochastic pix2pix models should be trained on the corresponding single scale, rule-based training models. When multiscale rule-based training models are available, we can calculate conditional multiscale reservoir model realizations without segmentation steps.

While I use rule-based models as the truth models in this chapter for the training to demonstrate the reproduction of depositional patterns and statistics, any other types of geologically realistic training models, such as satellite images, outcrop images can also be used for training.

4.2.3 Stochastic Pix2pix Model Training

Two injection wells (I1, I2) and two production wells (P1, P2) with a well spacing of 15 km are placed into the reservoir models (Figure 4.5). lithologies, porosity, and architectural element boundaries at lobe complex, lobe and lobe element scales are assumed known at the well locations. These well data are used as hard data for the stochastic pix2pix model. The stochastic pix2pix model is trained to calculate realizations of the 3D bed index distributions conditioned on the hard data. The derivation of the stochastic pix2pix method can be found in Pan et al (2020), and the architecture of the generator in the stochastic pix2pix method for exact well conditioning in lobe system modeling is in Figure 4.22.

4.2.4 Lobe Segmentation and Ordering

I propose a practical workflow based on density-based spatial clustering of applications with noise (DBSCAN) method to automatically segment the lobes and lobe elements based on associated bed distribution and then assign depositional sequence based on the elevation of their centers of gravity.

The DBSCAN, a density-based clustering method, is applied for lobe and lobe element segmentation for the following reasons: (1) indices of beds inside a lobe or a lobe element are continuous; the indices become discontinuous between the adjacent lobe and lobe elements, the DBSCAN can make use of this feature and clusters architectural elements based on the closeness of beds of the same index; (2) the number of lobes within a lobe complex or lobe elements within a lobe is unknown, and the DBSCAN does not require prior knowledge of the number of architectural elements.

A large bed index (Figure 4.5) in a lobe or lobe element is in contact with the small bed index of adjacent elements. Given this pattern, the proposed segmentation approach starts with segmenting large-index beds at the bottom of each lobe, which are isolated from each other by continuous, small-index shaly rock. Low-index beds from adjacent lobes are more likely to connect with adjacent low-index beds. Therefore, I gradually include the beds with lower index by performing interpolation, allocating a voxel to its nearest lobe, until every voxel is assigned a label. Other recent instance segmentation methods, such as the region-based convolutional neural network (RCNN), Fast RCNN and Mask RCNN (Girshick, 2015; He, et al., 2017) may also yield accurate lobe segmentation results.

Nevertheless, the proposed segmentation should be more computationally efficient for these applications. The lobes and lobe elements are then ordered in temporal sequence based on the elevation of their center of gravity.

4.2.5 Statistical Assessment of Model Realizations

I use the synthetic models calculated with the rule-based simulator as the truth models, to provide conditioning data and validate modeling results.

To perform the statistical assessment, I use different metrics to evaluate the seismic conditioning biases and uncertainties, the reproductions of depositional rules, depositional surfaces, geometries of lobes, property distribution, and fluid-flow-related dynamic properties of model realizations. For the brevity of the demonstration, and the same depositional rules are applied across multiple scales, only the statistics at the lobe scale are analyzed.

Seismic conditioning bias for a lobe scale model realization is calculated as the relative mean absolute error (RMAE) between the sizes of the lobe complex (a voxel is labeled 1 if it is within the lobe complex, and 0 otherwise) calculated from the model realizations and the associated truth model, same as the $\mathcal{L}_{\mathrm{seis}}$ loss term in stochastic pix2pix (Pan, et al, 2020), divided by the volume of the lobe complex of the truth model.

To calculate the bias in seismic conditioning at the lobe element scale, I calculate one lobe element scale model realization for each of the truth lobe scale models and denote it as the lobe element scale truth model. I then use the well data from that lobe element scale truth model, and the lobe containers from a lobe scale model realization to calculate 1 lobe element scale model for each of the associated 100 lobe scale model realizations, the resulting lobe element scale models are denoted as lobe element scale model realizations. The seismic conditioning bias for lobe element scale model realizations is calculated in the same way as for lobe scale models, with the lobe element scale truth model as the truth model.

Shannon entropy measures the local uncertainty through the local variability of the bed distribution over multiple model realizations of a subsurface model (Babak, et al, 2013). Shannon entropy map is applied to evaluate the effects of well and seismic conditioning data on the uncertainty model represented by the realizations. The Shannon entropy map of bed distribution for each of the truth models is calculated based on the associated 100 model realizations. The Shannon entropy map is calculated as:

$$\mathrm{H}(\mathrm{x},\mathrm{y},\mathrm{z}) = -\sum_{i=1}^{N} p_i(x,y,z)\log_2 p_i(x,y,z) \tag{4.1}$$

where $\mathrm{H}(\mathrm{x},\mathrm{y},\mathrm{z})$ is the Shannon entropy, $p_i(x,y,z)$ is the probability that i_{th} bed exists at a location (x,y,z) in model realizations, and N equals 9, which is the maximum bed index.

To validate the reproduction of the number of lobes in lobe scale model realizations, I calculate the average numbers of lobes in the model realizations for each of the truth model over the associated 100 model realizations and compare them with the number of lobes in the truth model.

To validate that the model realizations reproduce the geometry of lobes in the truth models, I compare the lobe probability map, which is the probability of a voxel, offset from the centroid of a lobe, being part of that lobe, for both truth models and model realizations. The 10,000 model realizations and 100 truth models are segmented to obtain the geometries of all the individual lobes, the center of gravities of these segmented lobes are then placed to the same location, the voxels occupied by a lobe is labeled 1 and 0 otherwise. The lobe probability for both realizations and truth models are calculated by averaging the labels for each voxel.

The compensational index (CI) quantifies the degree of compensational stacking, the tendency for a lobe to deposit in topographic low (Straub et al. 2009); therefore, CI validates the reproduction of the lobe stacking rules, an important part of geologic conditioning. CI is calculated as:

$$\sigma_{SS}(T) = \sqrt{\int_A \left[\frac{r(T;x,y)}{\hat{r}(x,y)} - 1\right]^2 dA} \tag{4.2}$$

$$\kappa = -\frac{\ln\left(\frac{\sigma_{SS}}{a}\right)}{\ln(T)} \tag{4.3}$$

where σ_{SS} is the standard deviation of sedimentation/subsidence (SDS), $r(T;x,y)$ is the local sedimentation rate during one depositional event, which deposited for a time period of T, $\hat{r}(x,y)$ is the sedimentation rate averaged over all depositional events, and A is the lateral area of a model. The leading coefficient a and compensational index κ are coefficients determined through regression. Naturally occurring lobe reservoirs have κ that ranges from 0.5 to 1 (Straub et al. 2009). The depositional order that I obtained through lobe segmentation is based on the center of gravity instead of the actual temporal sequence, thus I indicate this necessary approximation of the compensational index through the term raster-based compensational index (RCI). In RCI calculation, a constant averaged sedimentation rate of $7.115 \times 10^5 m^3$ (1 voxel) per unit, time is assumed, and T is calculated sequentially according to the calculated temporal sequence of lobes. To calculate the RCI from model realizations and truth models, composite surfaces based on the sequence of lobes in a lobe complex are reconstructed and the SDS is calculated with Eq. 4.2 through linear regression in the logarithmic scale. I compare the RCI of the truth models and their realizations to obtain the average RCI difference quantifying the difference in the depositional patterns. The RCI difference is calculated with following steps: (1) the RCI is calculated for each of the truth models and the associated model realizations, (2) the averaged RCI of model realizations are calculated for each of the truth models by averaging the RCI of associated 100 model realizations, (3) the averaged RCI difference is calculated as the mean of the RCI of truth models subtracting the averaged RCI of their associated realizations.

Interfacial width (Barabási and Stanley, 1995) measures the roughness of a surface represented as the composite of lobes at a specific step in the centroid-based assignment of a sequence of lobes. It is the root-mean-squared fluctuation of the heights of a surface. It is defined as follows:

$$\mathrm{W} = \sqrt{\frac{1}{A}\int_{A}\left(h(x,y) - \bar{h}\right)^{2}} \tag{4.4}$$

where W is the interfacial width, $h(x,y)$ is the height of a surface at location (x, y), $\bar{h}$ is the average height of the surface, and A is the area of the surface on the x-y plane. The interfacial width for each surface in the model is calculated, and the histogram of the interfacial widths of training models and model realizations are compared to validate the proposed workflow.

Dynamic Lorentz coefficient (DLC) is a standard dynamic metric for reservoir flow diagnostic assessment to rank reservoir models (Shook & Mitchell, 2009). To calculate DLC, I simulate a single-phase, steady-state flow within the reservoir. The single-phase flow rate (q_j), pore volume (V_{pj}) and the time of flight (TOF) of the N streamlines are calculated to obtain the storage and flow capacity of the reservoir, which can then be used to calculate the DLC. The streamline distribution map, storage and flow capacity cross plot are efficient, visual tools to understand the impact of different subsurface models on the flow heterogeneity (Shook & Mitchell, 2009; Kaplan, et al., 2017; Lie, 2019). In Eqs. 4.5 and 4.6 I show how to calculate the storage capacity (Φ), the flow capacity (F), and DLC (L_C):

$$\Phi = \frac{\sum_{j=1}^{i} V_{pj}}{\sum_{j=1}^{N} V_{pj}} \; and \; F = \frac{\sum_{j=1}^{i} q_j}{\sum_{j=1}^{N} q_j} \tag{4.5}$$

$$L_C = 2\left(\int_0^1 F d\Phi - 0.5\right) \tag{4.6}$$

where i is from 1 to N, V_{pj} and q_j are ordered according to their velocity $\frac{q_j}{V_{pj}}$. To perform dynamic statistical analysis with truth models and associated realizations, the permeability distributions are calculated from porosity distribution with the Kozeny-Carman equation (Carman, 1956). The streamline distributions are calculated by assuming constant injection (2000 psi, red) and production pressures (1000 psi, black) at the four wells. To quantify the reproduction of DLC, the absolute difference of DLC is calculated for each of the truth models as the absolute value of the difference between the DLC of the truth model and the mean DLC of the associated 100 model realizations.

4.3 RESULTS

The multiscale model realizations are calculated and compared with the truth models to validate the reproduction of key features and evaluate the uncertainties.

4.3.1 Conditional Lobe Distribution

The bed distribution of one of the truth models and the associated conditional realizations are shown in Figures 4.6, 4.7, and 4.8. The stacking, geometry, orientational patterns, and the porosity distribution pattern of model realizations honor those of the truth model.

The seismic conditioning bias expectation of the calculated model realizations is $2.5897\times10^{(-5)}$ and the bed indexes are correct at the well locations, because of the skip connection layer in the generator (Figure 4.22).

4.3.2 Lobe Segmentation

An instance segmentation with the hierarchical DBSCAN clustering workflow is performed to calculate the location of each lobe and the associated depositional sequence from the bed model (Figure 4.9). From the comparison of the segmentation result with the associated porosity model, I find that the shape of the extracted lobe is consistent with the sequence of beds within the lobe, adjacent lobes are not amalgamated, and a lobe is not split into multiple small lobes after segmentation. The depositional sequence of lobes increases with the increase of the elevation of the associated underlying surfaces.

4.3.3 Conditional Lobe Element Modeling

I calculate two lobe element scale model realizations conditioned to the truth model (Figure 4.10) and a lobe scale model realization (Figure 4.11) respectively with the proposed workflow. The realizations demonstrate: (1) the lobe elements (E, F) conform to the bounding surfaces identified by the lobes (D). (2) The sequence of beds (B, C) within each lobe element and the shape and orientation of each lobe element (E, F) are consistent with the parameters specified in the rule-based models. (3) The distribution of lobe elements (E, F) is diverse. The averaged seismic conditioning bias for lobe scale realizations is 0.012.

4.3.4 Lithology and Property Modeling

I hierarchically calculate lithology and property distributions based on the parameterization rendered by the simulated depositional architectures at different scales. The lithology and property models at different scales conditioned to the lobe scale truth model and model realization are shown in Figures 4.12 and 4.13, respectively. Small scale lithology and property model realizations are simulated conditioned to the next large-scale realizations, contributing to the preservation of patterns of lithology and property distribution at large scales during the stochastic downscaling..

4.3.5 Statistical Validation of Reservoir Model Realizations

The proposed model-based statistics validate the model realizations for the following aspects: (1) the well and seismic conditioning, (2) the uncertainty in the number of lobes in model realizations, (3) geometry and depositional pattern reproduction, (4) univariate model property distribution, and (5) dynamic property reproduction. For the brevity of the demonstration, and given the stationarity assumption across all scales, this analysis is shown only for the lobe scale model realizations.

4.3.5.1 Well and Surface Conditioning Uncertainty Analysis

The Shannon entropy map is calculated from bed distribution in model realizations to quantify the uncertainties associated with conditioning data in stochastic architectural modeling (Figure 4.14). Shannon entropy ranges between 0 and 1 in this case; it is small at grid cells near the bounding surface of lobe complex (A) and well locations (B, C) and increases at grid cells away from the conditioning data. The Shannon entropy at well location is zero, indicating an exact reproduction of bed sequence at well locations.

4.3.5.2 Uncertainty of the Number of Lobes

In Figure 4.15A I compare the number of lobes in the truth model in Figure 4.6 with the associated model realizations. In Figure 4.15B, the average number of lobes in model realizations matches the actual number of lobes in truth models. The standard deviation of the number of lobes is calculated for each of the truth models over the associated 100 model realizations and demonstrated as the histogram in Figure 4.15C. The number of lobes in realizations shows diversity with an average standard deviation of 2.2.

4.3.5.3 Reproduction of Architectural-Element Geometry and Depositional Pattern

In Figure 4.16, I calculate and compare the 3D distribution (A, B), horizontal (C, D) and vertical (E, F) cross-sections of the lobe probability (E, F) of the truth models (A, C, E) and associated model realizations (B, D, F). The model realizations successfully reproduce the lobe geometries. The difference (G, H) of the lobe probability is below 10%, and the shape and orientation of the lobe probability of both the truth models and model realizations are consistent with the input parameters specified in the rule-based simulator.

To validate the reproduction of depositional rules, I compare the RCIs of the truth models and the associated model realizations. The distribution of time interval (T) and SDS of one of the truth models in the test set and the associated model realizations are shown in Figure 4.17 and used for RCI calculation. The averaged RCI difference across all models is 1.14%. The averaged standard errors of the regressions for the truth models and realizations are 0.0033 and 0.0040, respectively. The result that the RCI at large time interval is approximately equal to 1 (red line in Figure 4.17) are consistent with the lobe depositional experiment results obtained by Wang et al. (2011).

To validate the depositional pattern reproduction in the lobe scale model realizations, I compare histograms of interfacial widths (Figure 4.18A) of the all-model realizations and truth models in the test set in Figure 4.18B. The median value of interfacial widths of truth models and their realizations are 2.88 and 3.04 respectively, the interfacial widths of model realizations are higher by 5.5%, indicating a good reproduction of lobe geometries.

4.3.5.4 Univariate Statistics of Simulated Properties

In Figure 4.19, the histograms of the net to gross and porosity distribution in all truth models and their realizations are compared. The difference in their histograms is within 3%.

4.3.5.5 Analysis of Dynamic Property

The streamline distributions of one of the truth models and one of the associated model realizations are shown in Figure 4.20 (A1, A2, B1, B2). The storage and flow capacity cross plot and histograms of DLC for both realizations and truth models are plotted in Figure 4.20 (C1, C2). In the flow-storage capacity cross plot, the realizations (black) match the truth model (red) closely; in the histogram, the DLC of model realizations also reproduces the variability of those of truth models, and the mean of the DLC of the truth model's 100 model realizations is smaller than the DLC of truth model by 0.23%.

4.4 DISCUSSION

4.4.1 Depositional Patterns and Conditioning Data

In Figures 4.6 to 4.13, I compare the distribution of architectural elements, lithology and porosity of model realizations with those of truth models at different scales. The model realizations successfully reproduce the patterns in the truth models, such as the increase of bed order with associated elevation in lobes and lobe elements, bounding surfaces represented by shaly facies, compensational stacking of architectural elements, and the geometries of the elements. The reproduction of these patterns indicates that the stochastic pix2pix method is an efficient tool to perform stochastic hierarchical architectural element modeling. When combined with classical geostatistical conditional simulation methods, the stochastic pi2pix method can yield lithology and property models that are consistent with the geological concepts at different scales. The depositional patterns of architectural elements represented by the ordered beds are successfully reproduced by the generator in the stochastic pi2xpix model.

As for data conditioning, the distribution of lobe elements and lobes conform with the bounding surfaces of the lobe and lobe complex respectively. Data at well locations are reproduced without artifacts found near the well locations or near bounding surfaces. The stochastic pix2pix model does not have a mode collapse problem often observed in deep learning, i.e., the structures of the realizations show diversity while conditioning to the static data.

4.4.2 Effects of Conditioning Data on Lobate Model Realizations

In the Shannon entropy map of Figure 4.14, the entropy is low in the vicinity of bounding surfaces, and the entropy decreases with the increase of curvature of the bounding surface. This phenomenon can be explained as: the high-curvature surface indicates a single lobe deposited beneath/ above the surface, and the shape of the lobe can be inferred from the curvature; whereas the low curvature surface can either be formed by a large lobe or several small lobes, large uncertainty is associated with the shapes of the lobes. This indicates that the proposed workflow results in a rational uncertainty model for a multiscale fill of small-scale architectural elements within a large-scale architectural element.

For local well data, the entropy of lithology distribution near the well locations is relatively low, and the entropy generally increases with the distance from the nearest well. However, it is found that the well data may cause low uncertainty in the regions not adjacent to the well, this phenomenon can be explained as: (1) if two wells penetrate the same lobe, the area between these two wells can show low uncertainty; (2) due to the stacking rules, if two wells determine the locations of two lobes with high certainties, the lobe distribution between these two wells should also have high certainties.

4.4.3 Checkerboard Artifacts and Geometrical Uncertainty of Depositional Elements

Checkerboard artifact (Odena et al., 2016) is common in the model realizations calculated with GAN methods, it appears as higher noise-to-signal ratio in the model realizations than in the training models. These artifacts are caused by the deconvolutional process in the generator (Figures 4.21 and 4.22). In Figures 4.17, 4.18, and 4.20, the realizations have the bias to overestimate the DLC and interfacial width and underestimate the RCI. This phenomenon can be explained as: the checkerboard artifacts increase the short-range heterogeneity of the reservoir model realizations and cause more random lithology distribution and rougher surfaces. However, the checkerboard artifacts in the realizations are not severe; the DLC is only underestimated by 0.23 %, RCI is underestimated by 1.14%, and interfacial width is overestimated by 5.5%.

The geometry of the lobe probability distribution is consistent with the inputs of the rule-based simulator (Figure 4.16). High uncertainty appears near the edge of the lobe probability distribution because the edge parts of a lobe are more likely to be affected by nearby lobes deposited earlier or the boundaries of the lobe complex. The checkerboard artifacts also cause the difference in the lobe probability distribution between the truth models and the model realizations, the lobe probability distribution of the model realizations tends to overestimate the uncertainty of geometry because of the artificial randomness introduced by the checkerboard artifacts. However, the average error is about 1%, remaining at the acceptable level. This indicates that even though a small bias exists, the lobes in the model realizations effectively reproduce the training models' overall geometry and orientation. The P10 and P90 of the net-to-gross ratio (NTG) and porosity from the truth models are reproduced in model realizations (Figure 4.19).

4.4.4 Advantages and Potential Applications of Hierarchical Stochastic Pix2pix Workflow

The hierarchical stochastic pix2pix workflow can be used for efficient hierarchical subsurface modeling, it can stochastically calculate the lithology and property distributions of small-scale architectural elements conformed with large-scale architectural elements simulated or identified through the interpretation of geophysical data, these realizations can be applied as the prior models to solve a variety of subsurface inverse problems, for example, hierarchical history matching can be performed by gradually increasing the complexity of the models to avoid overfitting. Uncertainties of depositional architectures are better propagated to the production forecast, and P10 and P90 of the production forecast are more accurately calculated (Pan et al., 2020). When depositional architectures of the reservoir are correctly captured in the training models, the reservoir model should yield better production forecasts and assist decision-making in oil field development. Compared to current geostatistical methods, this workflow requires much less computational time and can robustly calculate conditional, multiscale reservoir uncertainty models with realizations.

4.5 CONCLUSIONS

Deepwater lobe deposits are important reservoir targets for oil and gas development. As such, reservoir models with good well, seismic conditioning, and multiscale geological concept conditioning are essential for successful reservoir development and risk analysis. The proposed workflow calculates diverse conditional, multiscale subsurface reservoir model realizations efficiently. New statistics are applied to validate the model realizations, and I find these realizations successfully honor the depositional patterns and geophysical conditioning data, the stochastic pix2pix method and the proposed hierarchical stochastic pix2pix workflow can be applied to efficiently calculate conditional multiscale stochastic lobe reservoir models that capture the geometrical and stacking patterns of the rule-based training models. Conditioning data are honored in the realizations, the incorporation of the conditioning data causes no obvious artifacts while rationally constraining the uncertainty model. Compared to the current reservoir modeling methods, the proposed workflow has improved well, seismic, and geological concept conditioning, and requires less computational time.

Future work could include the use of unconditional multiscale rule-based models as training models to train the stochastic pix2pix to directly calculate multiscale reservoir models, which may be more efficient than hierarchical stochastic pix2pix workflow that requires recursive application of stochastic pix2pix model. It is also possible to apply this workflow for other important depositional environments with distinct sedimentary architectures, such as the fluvial and carbonate deposits.

Table 4.1: Ranges of random model parameters of rule-based lobate reservoir modeling simulator.

Parameters	Low	High
Maximum height of lobe (*H*)	4 m	5 m
Radius (*R*)	18 km	20 km
Aspect ratio (*b*)	1.4	1.6
Orientation (φ)	25°	35°
Healing factor (*m*)	1.2	1.2

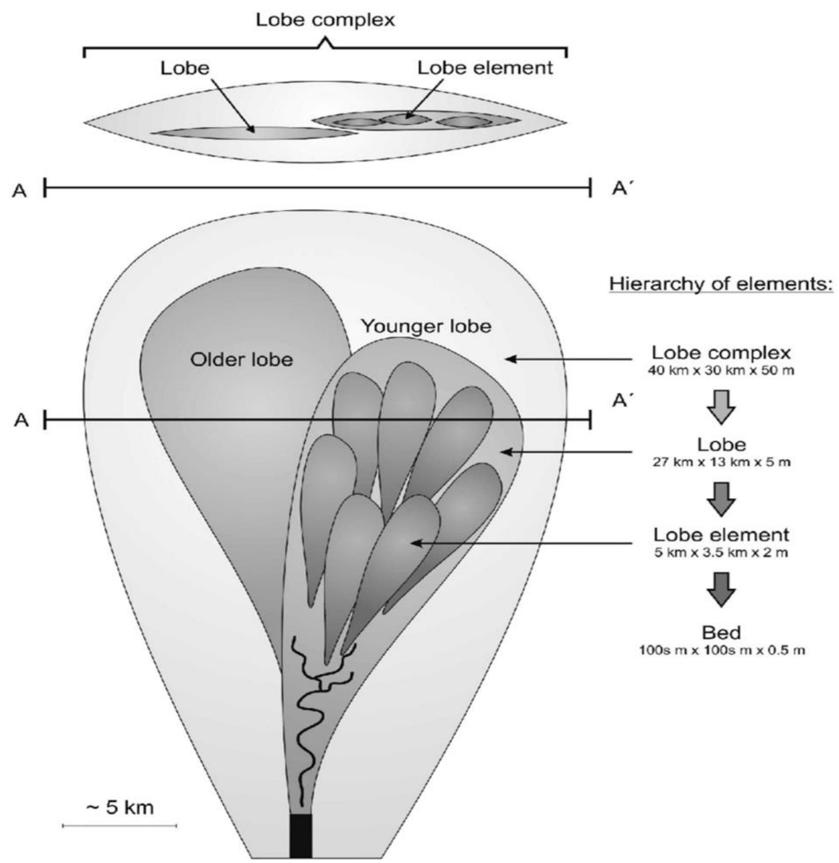

Figure 4.1: Hierarchical structure of a deepwater lobe deposit (Groenenberg, et al., 2010). The lobe element, lobe, and lobe complex show similar geometrical and stacking patterns. The spatial distribution of small-scale architectural elements conforms to the bounding surfaces of large elements.

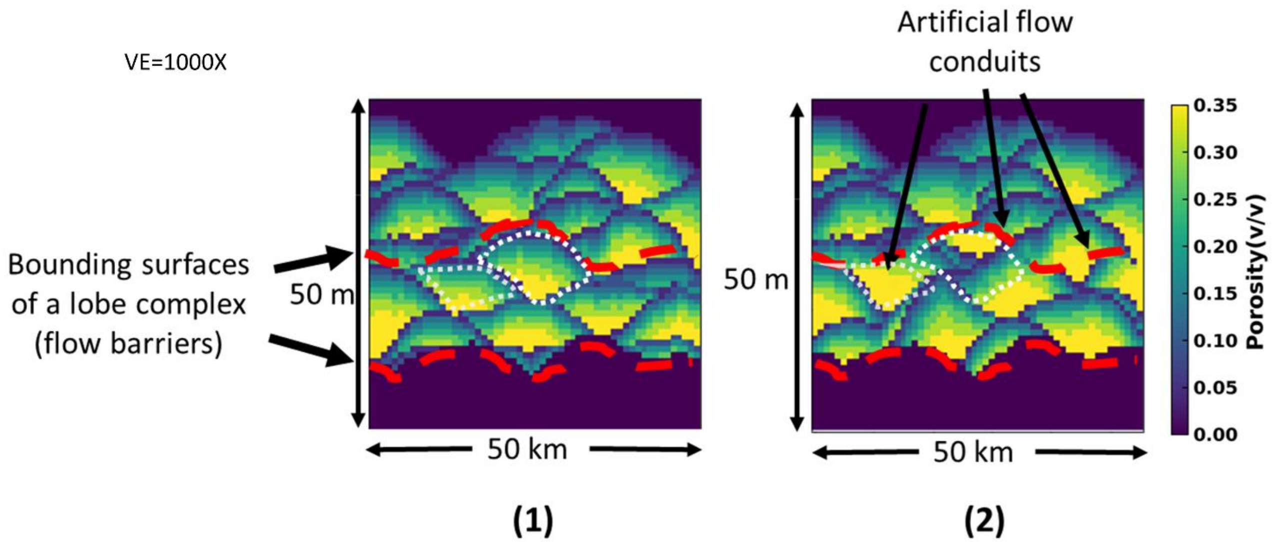

Figure 4.2: Connectivity artifacts caused by the 'cookie-cutter' approach in a vertical cross-section of a lobe deposit, with vertical exaggeration. Light yellow pixels represent sandy facies with high porosity, and dark green pixels represent shaly facies with low porosity. (1) the truth model and (2) one model realization calculated with the 'cookie-cutter' approach are compared. White dash lines outline lobes near the bounding surfaces (red dash lines) of the lobe complex, shaly flow baffles should exist at the bounding surfaces, but in (2), artificial flow conduits across the surface (black arrows) lead to an overestimation of reservoir connectivity. If an impermeable layer is artificially added to the upper surface, the geometries, and petrophysical property pattern of lobes adjacent to the surface are distorted. Images are vertically exaggerated 1000 times (VE=1000X).

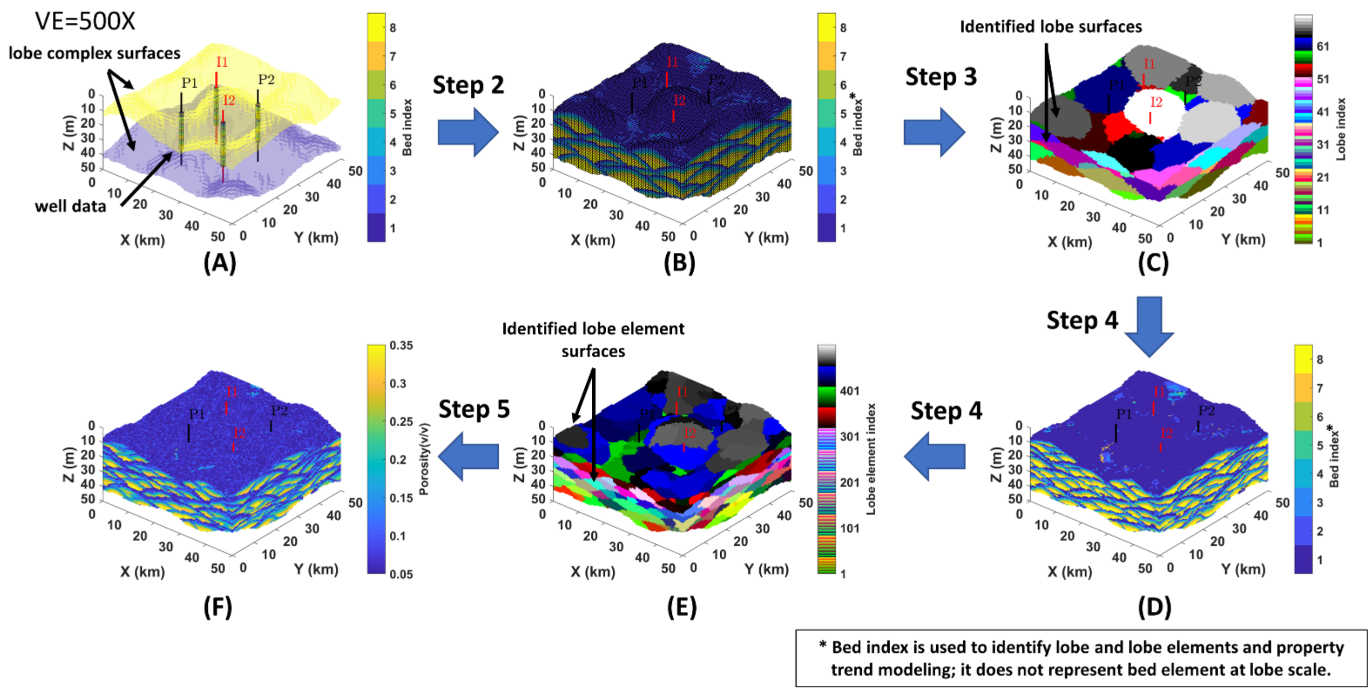

Figure 4.3: Workflow for hierarchical lobe deposit modeling. (A) Bounding surfaces of lobe complex and beds interpretations at well locations are used as input for the Stochastic pix2pix model, (B) bed index representation of lobe scale architectural model, (C)Lobes segmented based on the distribution of beds, (D) bed index representation of lobe element scale architectural model, (E) segmented lobe element scale architectural model, (F) Property model calculated with classical sequential Gaussian simulation conditioned on well, seismic data and architectural model.

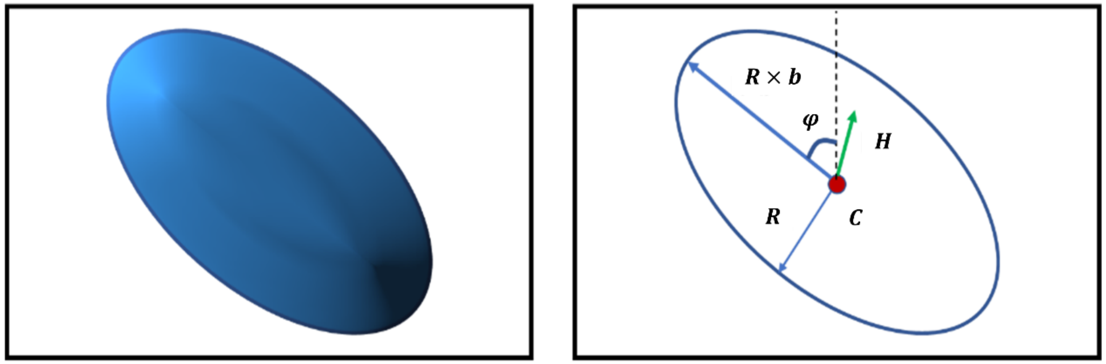

Figure 4.4: The shape of a lobe and the parameters used to define a lobe, length parameters of a lobe element are half of those shown in Table 4.1.

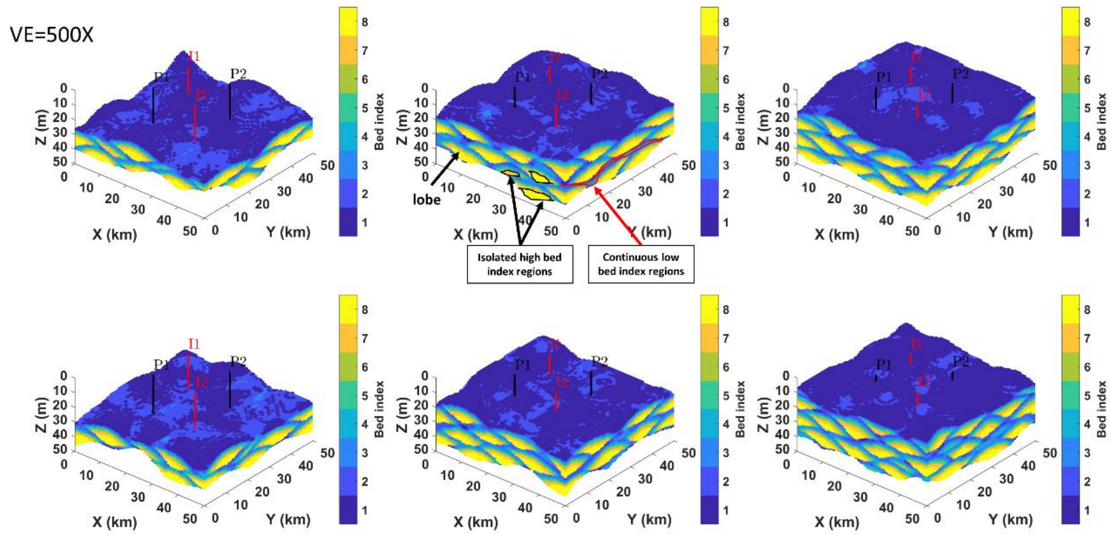

Figure 4.5: Bed distribution in training models calculated with UTLBPY. The 4 wells that condition the stochastic pix2pix models are indicated with black and red lines, but the training images are not conditional on these wells.

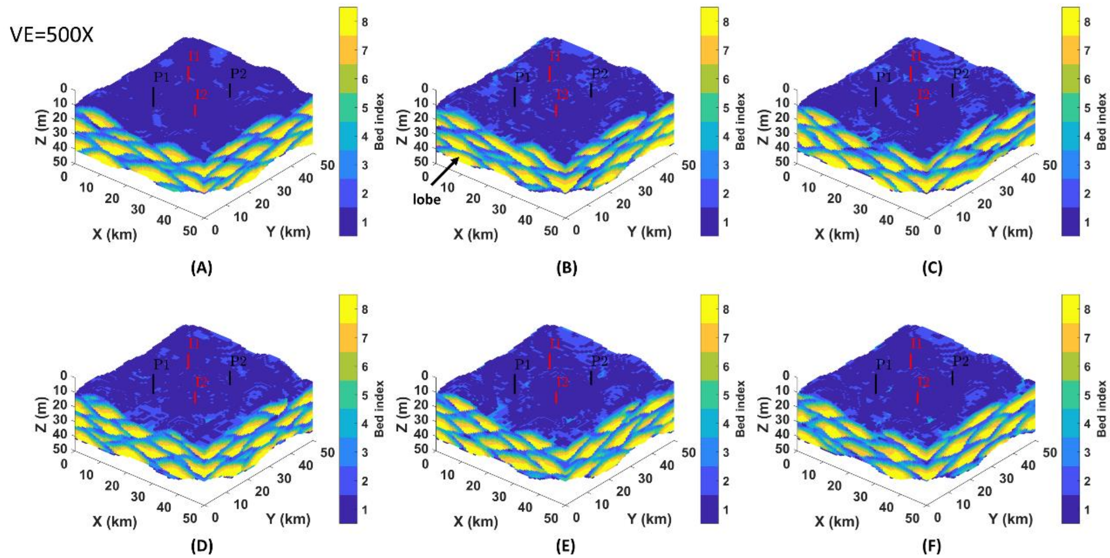

Figure 4.6: 3D bed distribution in lobe scale truth model (A) and the associated conditional model realizations (B, C, D, E, F). Model realizations have different bed distributions, indicating a good model diversity.

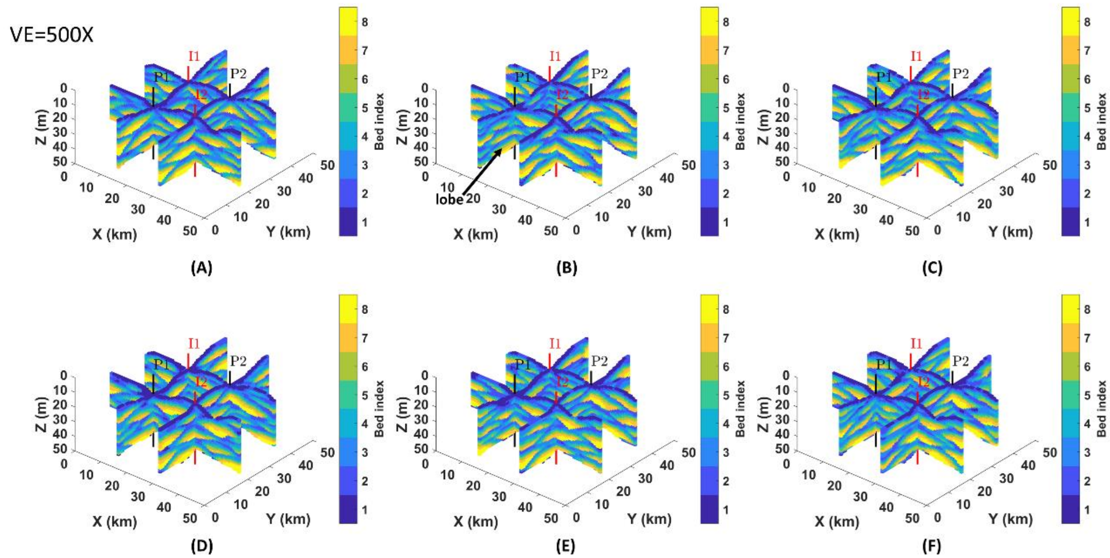

Figure 4.7: Fence diagram of bed distribution of a lobe scale truth model (A) and the associated conditional model realizations (B, C. D, E, F). A good reproduction of bed index at well locations indicates good well conditioning. Well data does not introduce artifacts to the lobes that wells penetrated.

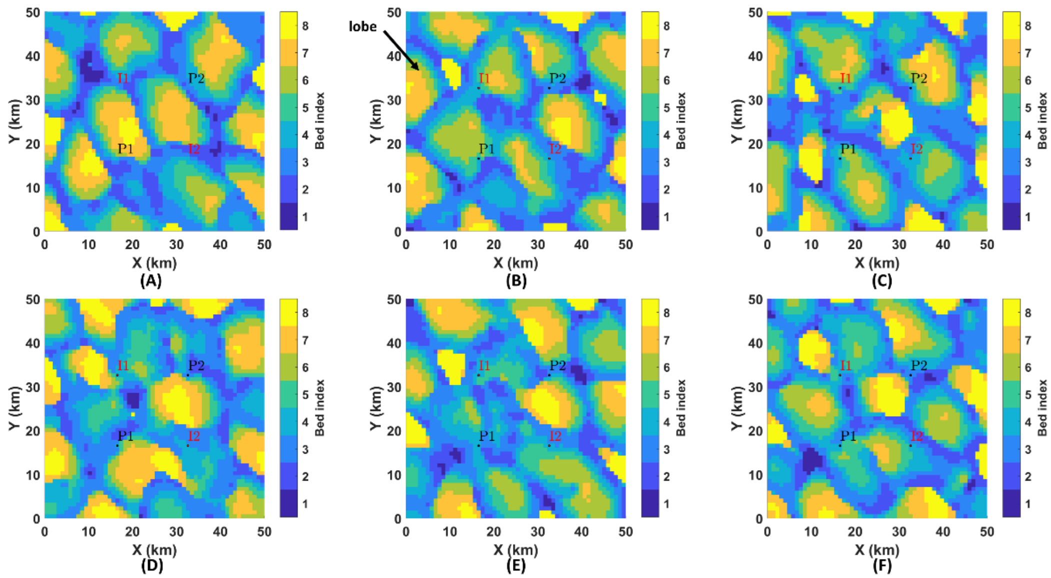

Figure 4.8: Horizontal cross-sections (28th layer) of bed distribution of lobe scale truth model (A) and the associated conditional model realizations (B, C, D, E, F). Adjacent lobes are separated by high bed index (low-quality rocks), and geometries of lobes in model realizations are similar to those in the training model.

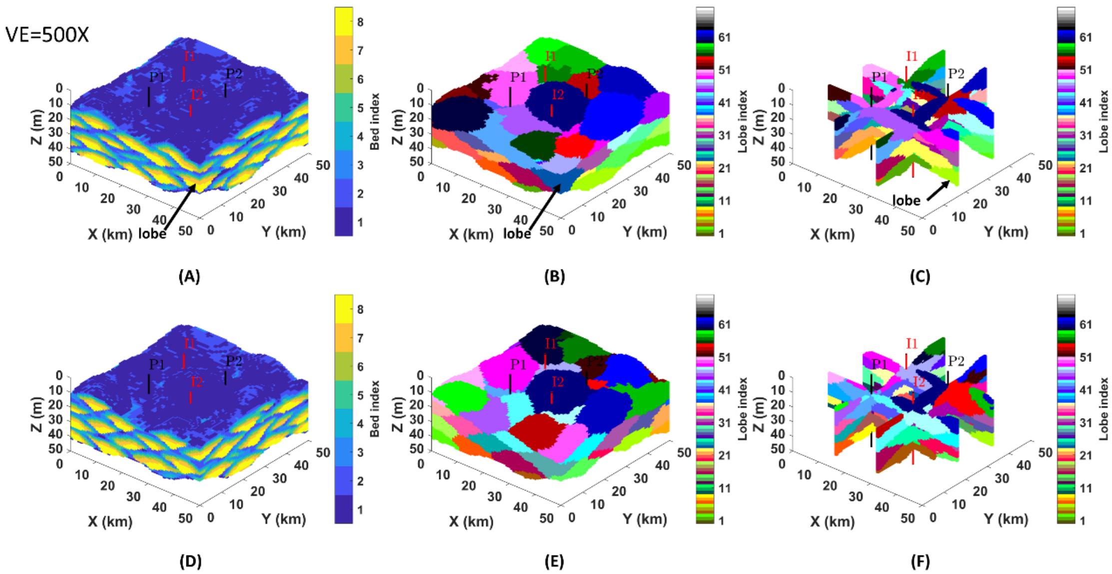

Figure 4.9: Lobes (B, C, E, F) segmented from the lobe scale bed distribution realizations (A, D), lobes are ordered based on the elevation of their center of gravity. Lobes identified are consistent with the bed index model, adjacent lobes are not lumped, and a lobe is not identified as two or more lobes.

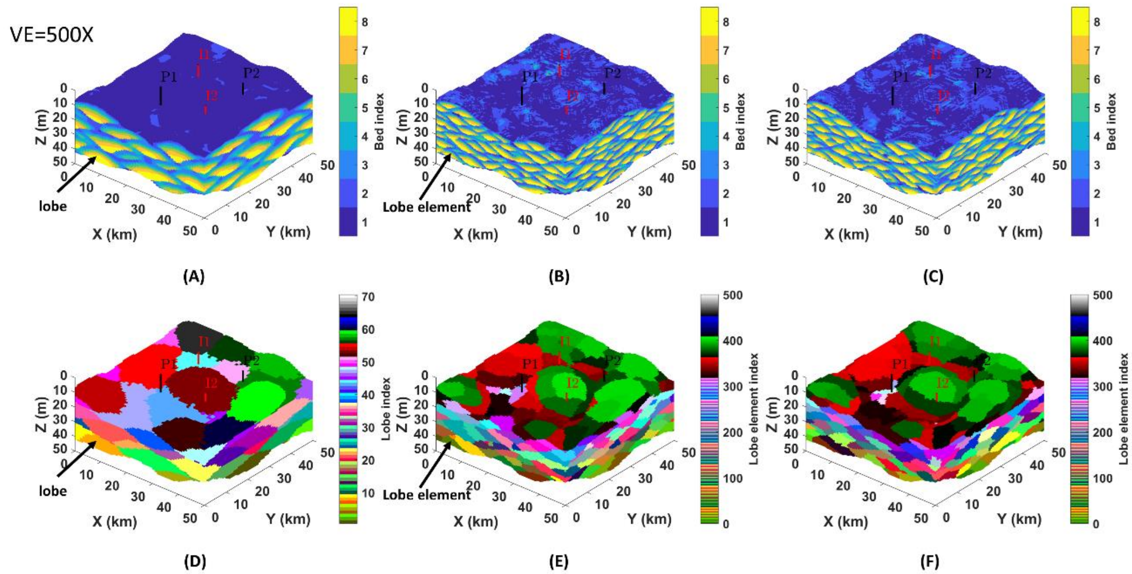

Figure 4.10: Model realizations of lobe element scale and associated lobe scale models. (A) Beds in the lobe scale truth model; (B, C) beds in lobe element scale model realizations; (D) lobes in the truth model; (E, F) lobe elements in lobe element scale model realizations. Lobe elements identified are consistent with the bed index model, adjacent lobe elements are not lumped, and a lobe element is not identified as two or more lobe elements. The stacking of lobe elements is constrained by lobe bounding surfaces.

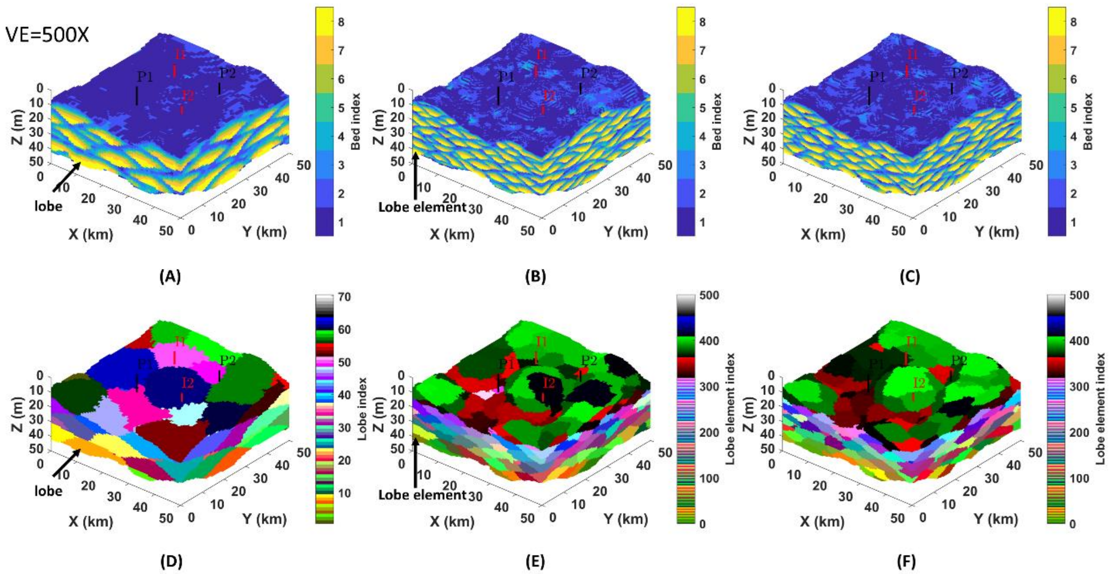

Figure 4.11: Model realizations of lobe element scale and associated lobe scale models. (A) Beds in the lobe scale model realization; (B, C) beds in lobe element scale model realizations; (D) lobes in the truth model; (E, F) lobe elements in lobe element scale model realizations. Lobe elements identified are consistent with the bed index model, adjacent lobe elements are not lumped, and a lobe element is not identified as two or more lobe elements. The stacking of lobe elements is constrained by lobe bounding surfaces.

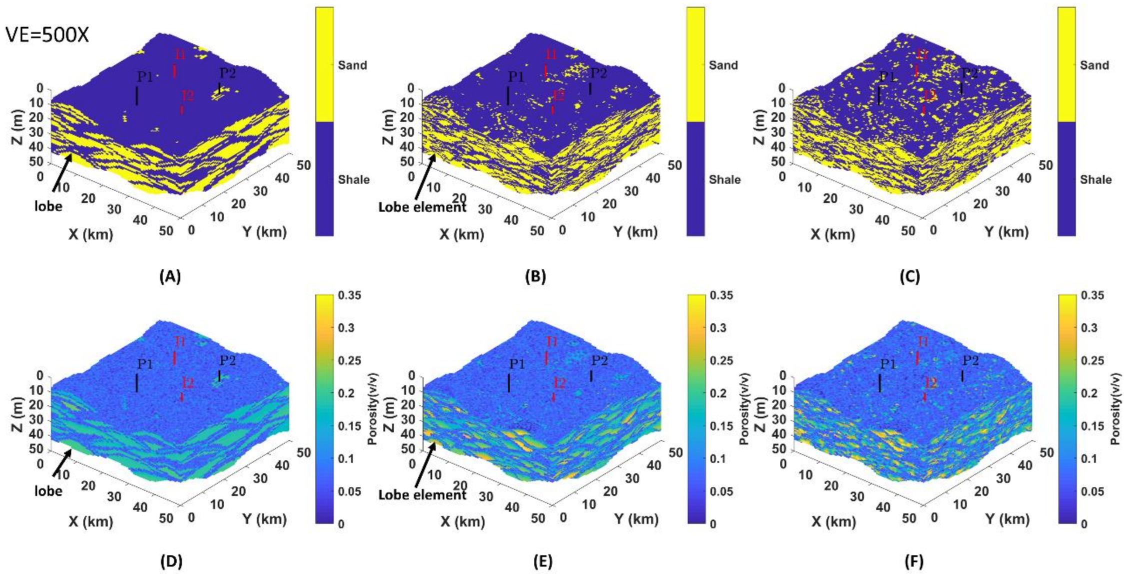

Figure 4.12: Multiscale lithology and porosity models conditioned to the lobe scale truth model. Lithologies (A, B, C) and porosity (D, E, F) models are simulated from the lobe scale (A, D) to the lobe element scale (B, E) and from the lobe element scale to the bed scale (C, F). Models at different scales are parametrized with beds in lobes (A, D), beds in lobe elements (B, E), and voxels (C, F) respectively. The decreasing upward trend of the net to gross and porosity are reproduced in model realizations.

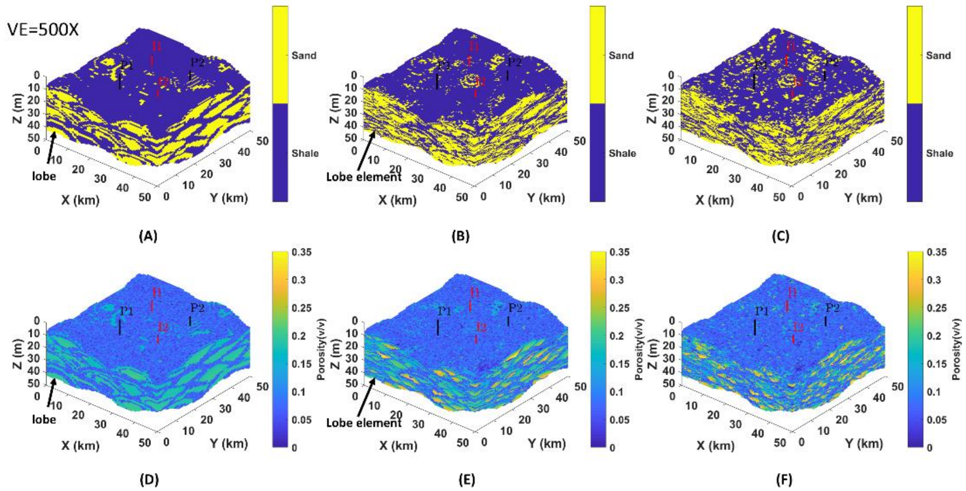

Figure 4.13: Multiscale lithology and porosity models conditioned to a lobe scale model realization. Lithologies (A, B, C) and property (D, E, F) models are simulated from the lobe scale (A, D) to the lobe element scale (B, E) and from the lobe element scale to the bed scale (C, F). Models at different scales are parametrized with beds in lobes (A, D), beds in lobe elements (B, E), and voxels (C, F) respectively. The decreasing upward trend of the net to gross and porosity are reproduced in model r

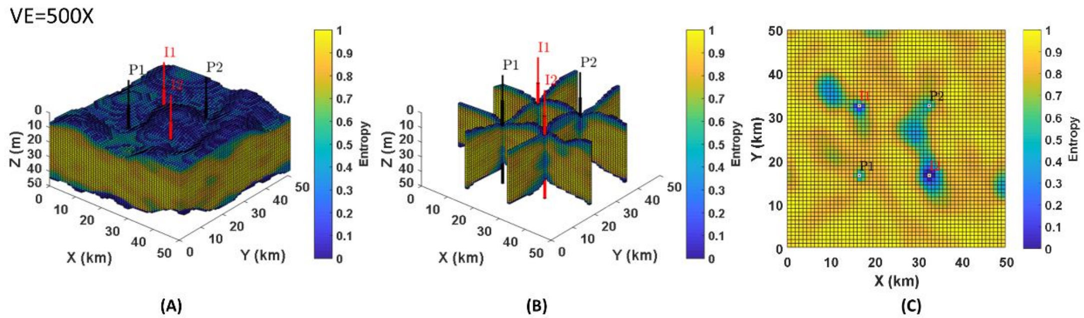

Figure 4.14: Shannon entropy map of bed sequence in lobe scale model realizations. (A) 3D Shannon entropy distribution; (B) fence diagram of Shannon entropy adjacent to wells; (C) the 28th horizontal cross-section of Shannon entropy map.

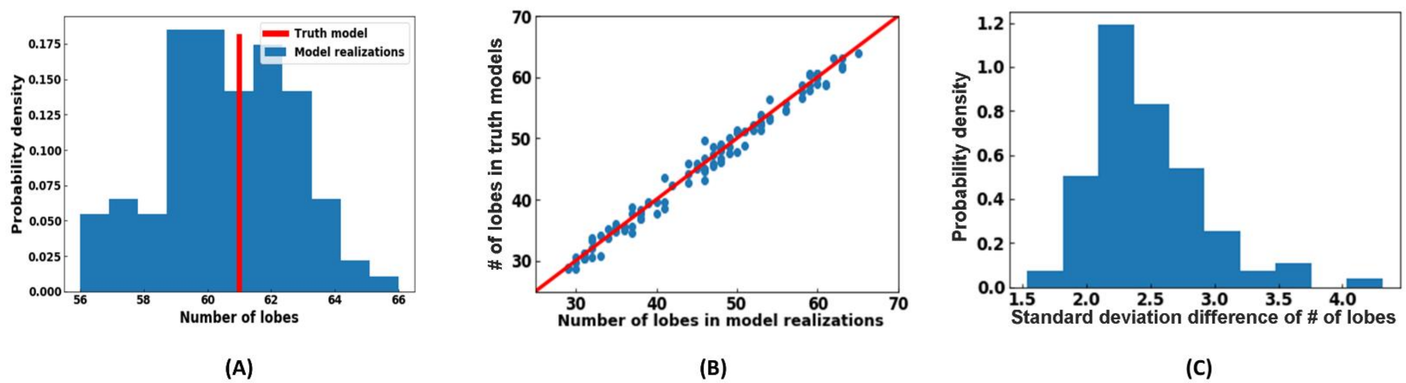

Figure 4.15: Comparison between truth models and model realizations based on the associated number of lobes. (A) Distribution of the numbers of lobes in each of the 100 model realizations of the truth model in Figure 4.6. (B) The number of lobes in truth models vs. the average number of lobes in the associated model realizations. (C) The distribution of standard deviations of the number of lobes in realizations.

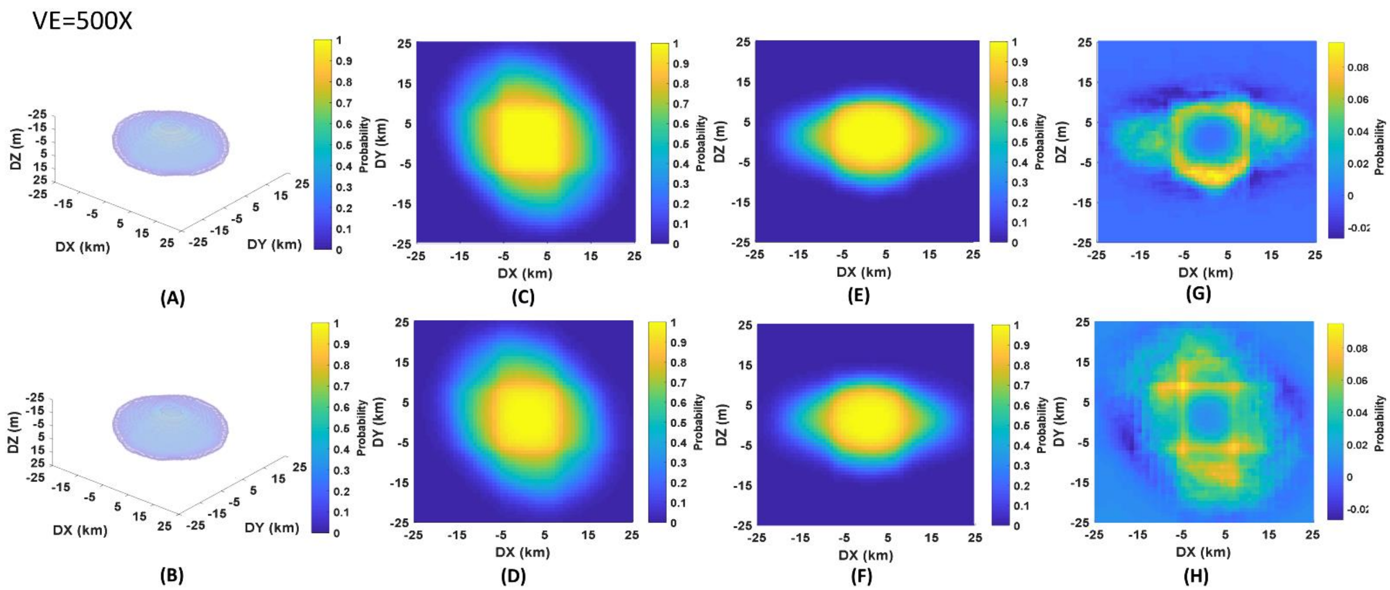

Figure 4.16: Comparison between the lobe probability maps of the training models (A, C, E) and realizations (B, D, F). (A) and (B) shows the probability that a voxel offset (DX, DY, DZ) from lobe centroid is within in the lobe; (C) and (D) are horizontal cross-sections of the lobe probability with zero vertical offsets (DZ); (E) and (F) are center vertical cross-sections of the lobe probability with zeros offset in Y direction (DY); (G) and (H) are the differences in the lobe probability of the two cross-sections (truth models minus model realizations).

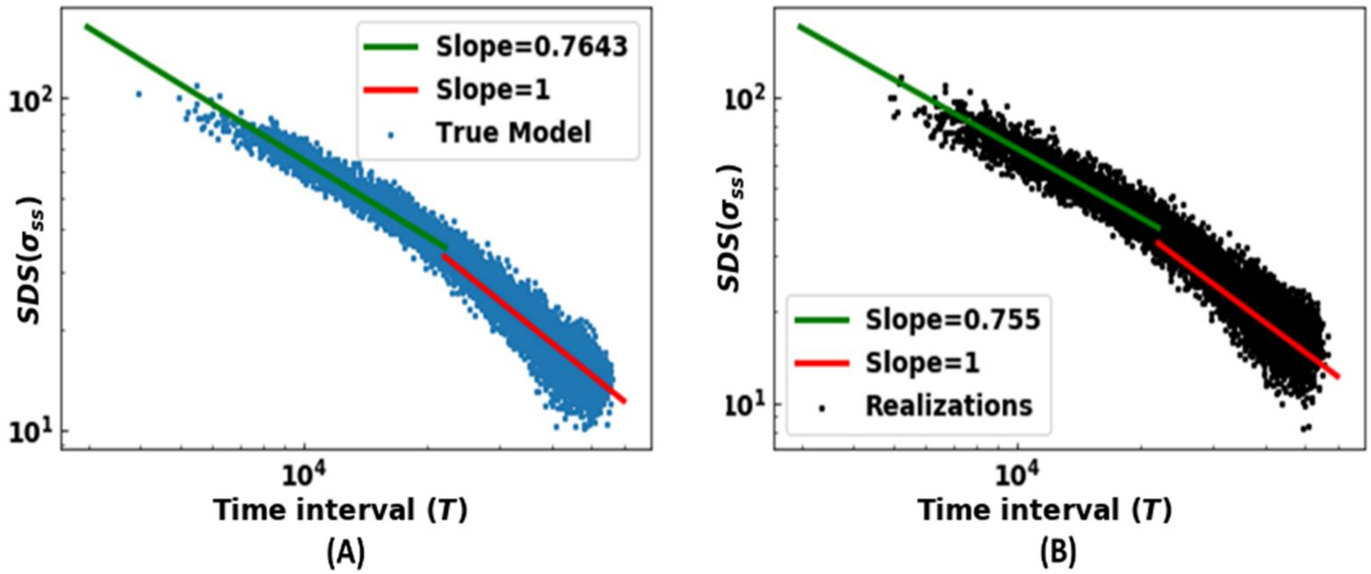

Figure 4.17: Cross plots of the standard deviation of sedimentation/subsidence (SDS) and time interval (T) for truth models (A) and realizations (B), two linear models (green and red lines) are fitted to the data to calculate the raster compensational index (RCI) of short-term deposition and long-term deposition.

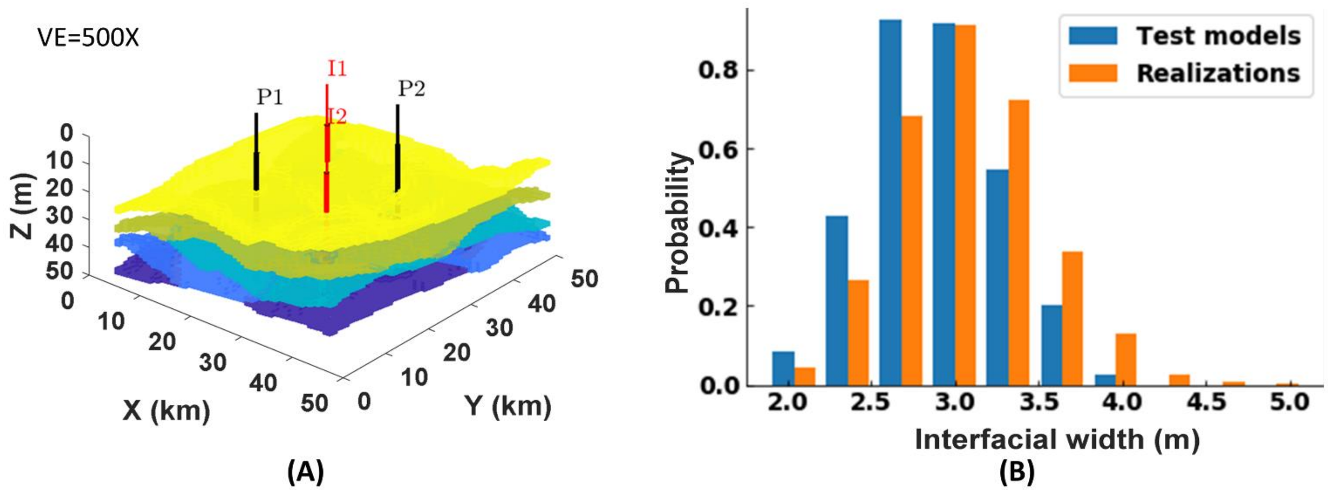

Figure 4.18: (A) Bounding surfaces extracted from one of the segmented lobe model realizations, (B) histograms of interfacial widths of the truth models (blue) and associated model realizations (orange).

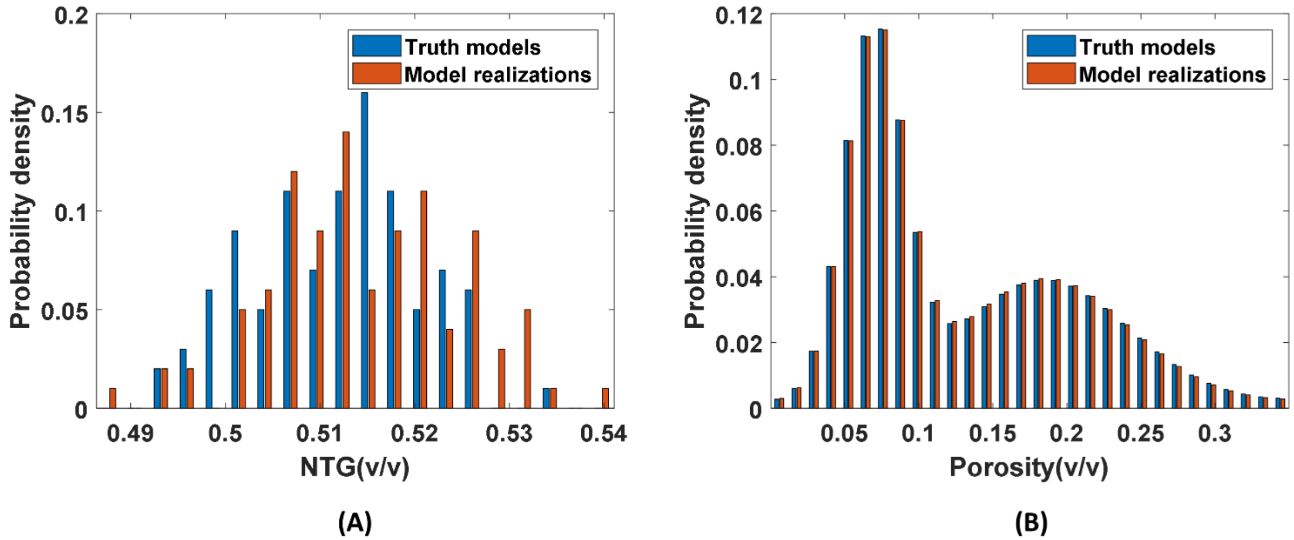

Figure 4.19: (A) Histograms of reservoir net-to-gross ratio (NTG) and (B) porosity for the truth models and model realizations.

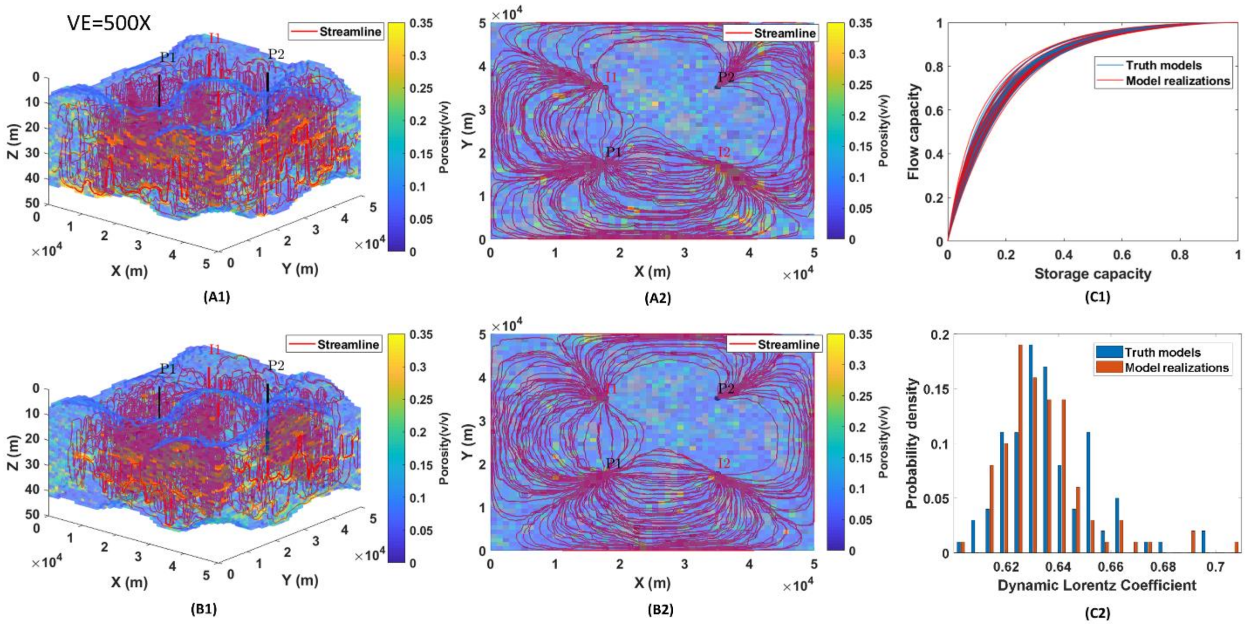

Figure 4.20: Flow diagnostic analysis. 3D (A1, B1) and top (A2, B2) views of Streamline (red) distribution within the truth model (A1, A2) and one of the model realizations (B1, B2). (C1) Storage and flow capacity of model realizations(red) and truth model (blue). (C2) Histograms of the DLC of model realizations (red) and truth model (blue).

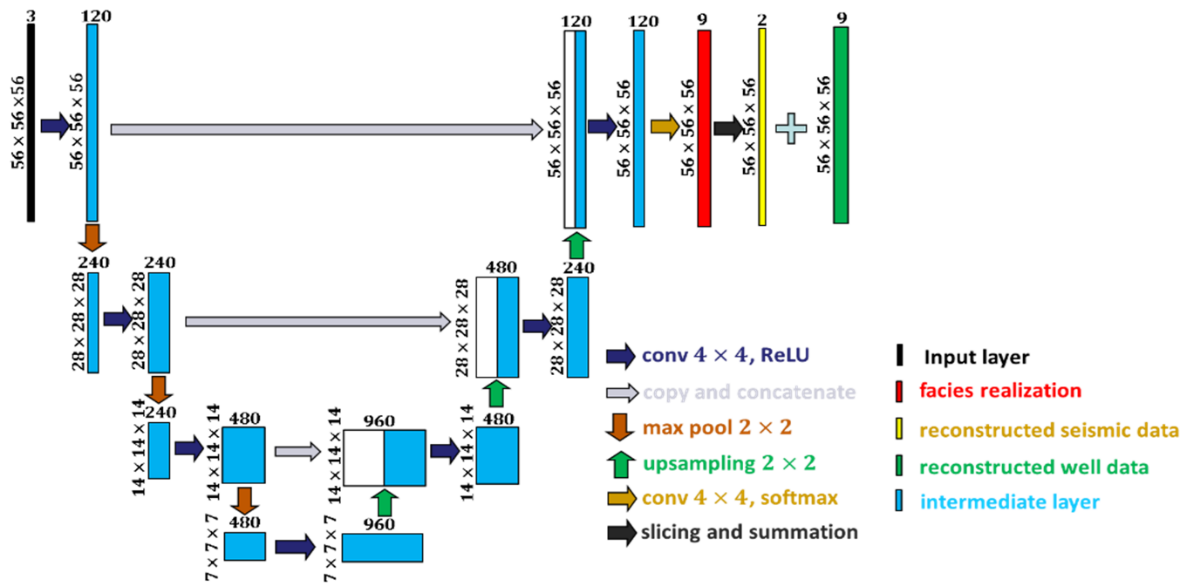

Figure 4.21: Structure of the generator (Pan et al., 2021). A U-net structure (Ronneberger et al., 2015) is used for latent space to reservoir model space mapping.

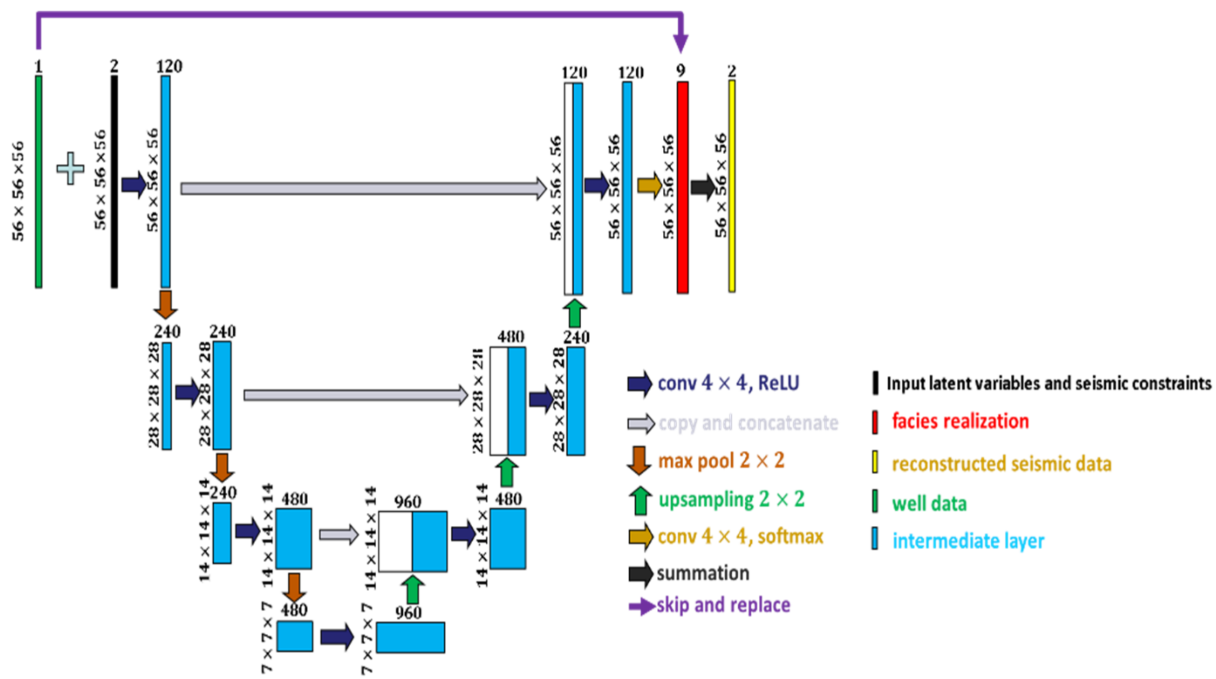

Figure 4.22: Structure of the new generator for better well conditioning. It improves well data conditioning by adding a skip connection (purple arrow) to the generator proposed by Pan et al (2021).

CHAPTER 5: Conclusions and Recommendations

Based on my work from previous chapters, in this final chapter, I summarize important findings, provide guidelines for best practice, and give recommendations for the direction of future work.

5.1 CONCLUSIONS

A comprehensive analysis of conventional petrophysical interpretation workflow under the framework of (geo)statistics reveals that the main source of interpretation error is the nonstationarity of rock property distribution and logging condition. Our findings on the importance of well-log preprocessing and nonuniqueness constraints should encourage more focus on (1) the interpretability of machine learning models and (2) petrophysical data preprocessing informed by domain expertise. This can avoid the situation of garbage in garbage out.

The stochastic pix2pix method and associated hierarchical modeling workflow enable more efficient conditional stochastic subsurface modeling for petrophysical property prediction between wells. The workflow can integrate different types of information. With the increase in our ability to obtain more data from the field, this capability of incorporating large and complex data is becoming increasingly important for reservoir description.

These accurate and efficient petrophysical interpretation methods and stochastic reservoir modeling methods enable agile and sensible decision-making in reservoir development

In this section, a detailed summary of my findings on well-log normalization, permeability prediction, and reservoir modeling is provided

5.1.1 Multivariate Statistics-Informed Well-Log Normalization and Permeability Prediction

i. Compared to physical model-based well-log correction, which assumes the model can simulate the actual physical phenomenon, correction based on normalization assumes the stationarity of formation properties between type and test wells. Well-log normalization methods are suitable for well-log correction when the borehole environment is too complex to be modeled, parameters about logging tools and environment are missing, or enough type wells have been drilled and calibrated.

ii. In complex reservoirs with large well spacing, statistical distance-based type well identification methods are better than the conventional, distance-based type-well identification method in permeability prediction. By directly considering the statistical similarity of well logs in different wells, the statistical distance-based method does not assume the spatial continuity of formation properties between wells, making it a more suitable method for well-log normalization in a reservoir that is regionally stationary.

iii. The DA well-log normalization method successfully decrease the error of permeability prediction from well logs for the SSAU carbonate reservoir. The decrease is more obvious for wells with abnormal well logs compared to wells with normal well logs.

iv. Compared to the permeability prediction model integrated with the conventional, two-point scaling normalization method, the DA model and linearly constrained model yield more accurate permeability prediction by considering the joint distribution of different types of well logs.

v. Permeability predicted with the linear constraint model has a lower variance compared to other models because of the average permeability constraint.

5.1.2 Stochastic Pix2pix for Stochastic Fluvial Channel Modeling

i. Fluvial channel model realizations generated with the stochastic pix2pix modeling method successfully reproduce patterns of facies and property distribution in the training images, while honoring static data.

ii. Compared to conventional, sequential simulation-based reservoir modeling methods, the stochastic pix2pix model is more computationally efficient, generating multiple reservoir model realizations within seconds.

iii. Architectural elements in a fluvial system, such as point bar, abandoned channel, and neck cut-off can be easily identified from facies model realizations generated with the stochastic pix2pix method. This indicates a good reproduction of depositional patterns.

iv. Petrophysical property patterns within architectural elements, such as the decrease of rock quality from the center of a point bar to the edge, are reproduced in the reservoir model realizations generated with the stochastic pix2pix method.

v. Reservoir model realizations generated with the stochastic pi2xpix method reproduce the spatial statistics of the training model, including semi-variogram and MPH.

vi. The stochastic pix2pix method successfully reproduces long-range patterns, such as the continuous channel, in the model realizations it generates. The seismic and well data are also honored in the model realizations.

vii. Model reduction and parameterization rendered by the stochastic pix2pix method make it easy to use the reservoir model realizations as prior models for inverse problems, such as history matching. Continuous changes in the latent variable space result in continuous changes in model space.

5.1.3 Hierarchical Modeling of Deepwater Lobate Reservoir with ML Methods

i. The proposed ML-based, hierarchical modeling method successfully generates diverse, multi-scale lobate, facies, and property model realizations.

ii. Model realizations generated with the hierarchical modeling workflow reproduce both depositional patterns and dynamic property (DLC) of the training model.

iii. The relationship between architectural elements at different scales is believed to be reasonable, where the bounding surface of a large architectural element is formed by the aggregation of bounding surfaces of small architectural elements.

iv. The hierarchical modeling workflow enables the modeling of large, detailed lobate systems with limited computational resources. It is more efficient than classical, sequential simulation-based methods.

v. Despite a mild checker-board effect, statistics, such as porosity histogram and net to gross, are reproduced in reservoir model realizations.

5.2 RECOMMENDATIONS

To be able to use spatial statistics of rock property to constrain well-log interpretation and to perform reservoir modeling that is informed by well-log interpretation, I summarize best practices to apply the DA model for permeability prediction and the stochastic pix2pix method for reservoir modeling.

5.2.1 Best Practices for Well-Log Normalization and Interpretation

i. The DA model assumes stationary formation properties between training and test wells. Zonation is recommended before performing normalization and interpretation because it helps identify formations with similar depositional environments. This improves the stationarity between training and test data, and thus improves the accuracy of well-log normalization and interpretation.

ii. The well-log normalization is performed based on summary statistics of each zone. However, local, abnormal measurements may introduce large errors to the calculation of the statistics. Therefore, proper preprocessing, which removes local, abnormal spikes, is recommended.

iii. Models are trained with both core measurements and well logs. If well logs are not properly aligned with core measurements, the performance of the model is degraded. The misalignment results from adverse borehole conditions, such as the stick and slip of logging tools. To mitigate this problem, depth matching is needed to improve the alignment of well logs and core measurements.

iv. Training the DA model with a large learning rate can be unstable, thus a small learning rate and batch normalization are recommended to improve the stability of the training process.

v. When the size of the training set is small, a simple neural network with a few layers is desired to avoid potential overfitting. Proper feature engineering is also recommended for training shallow neural networks, for example, gradients of well logs are proven to improve the accuracy of well-log interpretation. Similar to the well-log normalization method, the gradient feature assumes that well logs and associated features among wells are stationary, and therefore, it removes potential, low-frequency bias in well logs.

5.2.2 Best Practices for ML-Based Reservoir Modeling

i. The stochastic pix2pix algorithm minimizes the J-S divergence between the training models and generated reservoir model realizations on the feature space identified by the discriminator. However, it is difficult to tell when to stop the training from the loss function. Therefore, I recommend using the divergence of the multiple-point histogram (MPH) between the training models and the model realizations as the criteria for stopping training. The training stops once the divergence stops decreasing significantly.

ii. The training models used in this dissertation are calculated with rule-based reservoir modeling programs. Other training models, such as satellite images and outcrop of analogs, can also be used to generate more realistic reservoir model realizations.

iii. The step size during model training should be small to ensure stable training. A large step size may cause the discriminator to converge to a local minimum and introduce mode collapse problems.

iv. The ML-based reservoir modeling methods are a type of global optimization method. During the training, the divergence between the training and generated models of the whole reservoir model is minimized, whereas, for the sequential simulation method, only local statistics are reproduced. Therefore, the ML-based method is more suitable for simulating reservoir models with large-scale patterns.

v. Because the convergence of the GAN-based, stochastic pix2pix model is difficult to detect, diagnostic statistical plots, such as the MPH, facies histogram, property histograms, and semivariograms, have to be calculated for both the training and simulated models and compared to ensure the reproduction of spatial statistics in model realizations.

vi. Because of the potential mode collapse problem, the diagnostic statistical plots should be calculated for the same region in each model realization to ensure the diversity in model realizations.

5.3 FUTURE WORK

Potential future work to further advance the integration of geostatistics and petrophysical interpretation is provided in this section.

5.3.1 Future Work for Well-Log Normalization and Interpretation

i. Well-log correction via well-log normalization is based on the assumption of stationary petrophysical property. To ensure formation properties between training and test wells are stationary, we have to perform zonation for each well. However, 1) zones may not be identified based on the stationarity of the formation properties, and 2) it can be time-consuming to identify zones in each well manually. Therefore, it is important to develop an automatic zonation method and a well-correlation method to accurately identify zones for well-log normalization.

ii. Because the number of wells is small, I explicitly calculate the statistical distance between wells to identify type wells for a test well. However, it is also important to check if we can directly add summary statistics of well logs as additional features to help machine learning models improve permeability prediction accuracy.

iii. Data-driven well-log interpretation methods are susceptible to local, abnormal measurements, and automatic abnormal detection algorithms to help identify local anomalies may improve the accuracy of the interpretation.

iv. Uncertainty quantification for petrophysical interpretation is important for understanding the reliability of data-driven interpretation results. Therefore, ensemble- or variational-inference-based uncertainty quantification methods should be developed to perform uncertainty estimation.

v. The new methods developed in this dissertation for well-log interpretation are only validated with field data from the SSAU for permeability prediction. Further study to investigate the applicability of this method to the prediction of other formation properties from other types of reservoirs should be helpful to understand the applicability of the methods.

5.3.2 Future Work for ML-Based Reservoir Modeling

i. Because ML-based reservoir modeling methods require large computer memory to model large reservoirs, I propose to use a hierarchical workflow. However, in the industry, sequential simulation is a more common solution for building large reservoir models. Therefore, it is also important to check how the ML-based, sequential simulation method may work compared to the hierarchical work.

ii. I successfully applied machine learning-based reservoir modeling methods for the modeling of the fluvial channel, turbidite channel, and lobate systems. However, it is important to test if the methods also work for other more complex depositional systems.

iii. The ML-based reservoir modeling methods use variational inference to map simple latent random variables to depositional patterns in a reservoir. It is important to know what types of patterns cannot be reproduced with the variational inference.

The amount of computational time required for training the stochastic pix2pix model for stochastic reservoir modeling is large compared to conventional geostatistical methods. Optimization of the neural network structure to accelerate the training process should be conducted to make the ML-based reservoir modeling workflow more efficient.

Nomenclature

LIST OF SYMBOLS

Chapter 2

$\|\quad\|_2$: L2 norm, mean squared error

$\mathcal{L}_{adv_D}$: Discriminator adversarial loss
$\mathcal{L}_{adv_G}$: Generator adversarial loss

$\mathcal{L}_{adv_{GC}}$: Generator adversarial loss when the well log uncertainty is known

$\mathcal{L}_{lc}$: Linear constraint

$\mathcal{L}_{linear}$: Loss function of the linear predictive model

$\mathcal{L}_{pred}$: Prediction error of a training set

C_d: Covariance matrix of petrophysical property prediction

$\tilde{X}$: Preprocessed predictor features (normalized well logs)

$\tilde{Y}$: Response feature prediction (petrophysical property, permeability prediction)

$\bar{Y}$: Averaged value of the petrophysical property along an interval (zone) of a well

X: Predictor features (well logs)

Y: Response features (petrophysical property, permeability)

A, B: Slope (A) and Intercept (B) of a linear model

Cov: Covariance calculation operator

D: Discriminator in a discriminative adversarial model

E: Differences between permeability predictions calculated with different models

G: Generator in a discriminative adversarial model

M: Mapping layers that predict permeability from (normalized) well logs

m_i: Weight for the adjacent ith permeability measurement, which is calculated with the Kriging method

P: Preprocessing layers for well-log normalization

$P_i(X), P_j(X)$: Probability distributions of well logs from well i and j

$x, y, \tilde{x}, \tilde{y}$: Samples drawn from data set X and Y respectively

$\mathbb{E}$: Expectation

min: Minimum value

max: Maximum value

$Div(i,j)$: JS divergence between well logs from well i and well j

$KL(P_i||P_j),\ KL(P_j||P_i)$: KL divergence from well logs i to well logs j and from well logs j to well logs i.

$Dist(i,j)$: Spatial distance between well i and well j

loc_{x_i,y_i}: X and Y coordinates of well i

Subscripts of Chapter 2

l: Parameters and coefficients of a linear model

s: Features/Layers from the training set

t: Features/Layers from the test set

u: Unbiased measurements

Chapter 3

D: Discriminator in a discriminative adversarial model

G: Generator in a discriminative adversarial model

G^{-1}: Reverse the calculation performed by the generator and obtain conditioning data from reservoir model realizations

x: Conditioning data

x_train: Conditioning data (well and seismic data) in training reservoir models

x_t: Inputs of the generator at iteration t, which include latent variables and parameters for rule-based reservoir modeling

$f(x)$: *a priori* distribution of inputs of the generator

$f_2(x_t)$: Probability distribution of the conditioning data, which is used to calculate the evidence probability

$T_{threshold}$: maximum number of iterations during the MCMC optimization

y: Reservoir model realizations calculated with the generator in a GAN model

y_{train}: Training reservoir models calculated with rule-based modeling method

z: Random variables in the latent space

l_t: loss function at iteration t during the MCMC optimization

$\mathcal{L}_{L1}$: L1 norm loss function

$\mathcal{L}_{CGAN}$: Loss function of a conditional generative adversarial model

$\mathcal{L}_{pix2pix}$: Loss function of a pix2pix model

$\| \quad \|_1$, $\| \quad \|_2$: Operations to calculate L1, L2 norms

$\mathbb{E}$: Expectation

λ, λ_{log}, λ_{seis}: Certainty coefficients for data conditioning (well log: λ_{log}, seismic data: λ_{seis})

Y: Gaussian random variables

arg: Find model parameters via stochastic gradient descent method

$(\max_{D})$: Maximize the probability that the discriminator can successfully distinguish the generated reservoir models from training images

$(\min_{G})$: Minimize the probability that the discriminator successfully distinguishes the generated reservoir models from training images

$\mathcal{L}_{L2_{sto}}$: Loss function of the L2-norm of conditioning data mismatch

$\mathcal{L}_{\ sto}(x, z)$: Loss function of a stochastic pix2pix model

$\mathcal{L}_{\text{seismic}}$: Loss function for seismic conditioning

$\mathcal{L}_{\text{well\_log}}$: Loss function for well-log conditioning

$\mathcal{L}_{\text{sto}}^{*}$: Loss function of a stochastic pix2pix model conditioned to seismic and well data

L_{cat}: Mean categorical error of data conditioning

m_{ik}: A point in the binary correctness map, which equals 0 if the facies at k_{th} pixel are the same in both the i_{th} true model and i_{th} reservoir model realization

t_{ik} The probability that in the i_{th}realization, the facies at $\mathrm{k_{th}}$ pixel is sandy facies

t_{ik}^{*}: The probability that in the i_{th}training image, the facies at $\mathrm{k_{th}}$ pixel is sandy facies

t: Angle used in gradual deformation method

w_{il}: The probability of each facies existing at the lth well location in the ith reservoir model realizations

w_{il}^{*}: The one-hot encoding of the facies existing at the lth well location in the ith training image

N: Batch size

K: Number of pixels in the reservoir model

L: Number of well-log interpretations

k: Wavelength for rule-based channel system modeling

h: Dampening factor for rule-based channel system modeling

s: disturbance variance for rule-based channel system modeling

Chapter 4

$\mathrm{H(x, y, z)}$: Shannon entropy of reservoir model realizations at (x, y, z)

$p_i(\mathrm{x, y, z})$: Probability that the i_{th} bed exists at a location (x, y, z) in model realizations

σ_{SS}: Standard deviation of sedimentation/subsidence

T: Stratigraphic time required for one depositional event

$r(T; x, y)$: Rate of sedimentation at location (x, y) during one depositional event

$\hat{r}(x, y)$: Sedimentation rate averaged over all depositional events

A: Lateral area of a model

a: Leading coefficient

κ: Compensational index

W: Interfacial width

$h(x, y)$: Height of a surface at location (x, y)

$\bar{h}$: Averaged height of a surface

q_j: Single-phase flow rate of streamline j

V_{pj}: Pore volume along streamline j

N: Total number of streamlines

Φ: Storage capacity

F: Flow capacity

L_C: Dynamic Lorentz coefficient

H: Maximum height of a lobe

R: Radius of a lobe

b: Aspect ratio of a lobe

φ: Orientation of a lobe

M: Healing factor of a lobe

LIST OF ACRONYMS

ANN: Artificial neural networks

AR: autoregressive random (process)

CALD: Caliper log (in)

CGAN: Conditional generative adversarial networks

CI: Compensational index

CKMAX: Maximum core permeability measurement (mD)

CNN: Convolutional neural network

CycleGAN: Cycle-consistent adversarial networks

CPOR: Core porosity measurement (v/v)

CPU: Central processing unit

DA: Discriminative adversarial model

DBSCAN: Density-based spatial clustering of applications with noise

DLC: Dynamic Lorentz coefficient

DT: Sonic slowness log (us/ft)

GAN: Generative adversarial neural network

GRD: Gamma ray log (api)

JS: Jason-Shannon (divergence)

K: Permeability

KL, K-L: Kullback–Leibler (divergence)

LLD: Lateral deep resistivity log

LLS: Lateral shallow resistivity log

MCMC: Markov Chain Monte Carlo sampling methods

MDS: Multi-dimensional scaling

M-H: Metropolis-Hastings sampling method

ML: Machine learning

MMD: Maximum mean discrepancy

MMDDT: Maximum mean discrepancy domain transfer (learning)

MPH: Multiple-point histogram

MPS: Multiple-point simulation

MSE: Mean squared error

NPHI: Neutron porosity log (v/v)

NTG: Net-to-gross ratio

NN: Neural network

RCI: Raster-based compensational index

RCNN: Region-based convolutional neural network

ReLU: Rectified linear unit

RF: Random forest model

RHOB: Density log (gm/cm3)

RMAE: Relative mean absolute error

SDS: Standard deviation of sedimentation/subsidence

SGS: Sequential Gaussian simulation

SSAU: Seminole San Andres Unit

TI: Training images

TOF: time of flight

UTFLUVPY: A rule-based, channel system modeling program

UTLBPY: A rule-based, lobate system modeling program

VE: Vertically exaggerated (X times)

Suffix

_DA: Normalized well logs and permeability prediction calculated with the DA model

_linear: Normalized well logs and permeability prediction calculated with the linearly constrained model

_origin: Original well logs and permeability prediction calculated with the model without any constraints

_scaling: Normalized well logs and permeability prediction calculated with two-point scaling method

References

Abreu, V., M. Sullivan, C. Pirmez., and D. Mohrig, 2003, Lateral accretion packages (LAPs): an important reservoir element in deep water sinuous channels: Marine and Petroleum Geology, **20**, 631-648.

Aguirre, O., and R. Antelo, 2001. Log normalization, a very important task in the petrophysical evaluation for La Peña and Tundy fields: Presented at the SPE Latin American and Caribbean Petroleum Engineering Conference.

Al-Mudhafar, W. J., 2017, Integrating well log interpretations for lithofacies classification and permeability modeling through advanced machine learning algorithms: Journal of Petroleum Exploration and Production Technology, **7**(4), 1023-1033.

Alpak, F. O., J. W. Jennings, P. Gelderblom, C. Chen, G. Gao, and K. Du, 2017, A direct overparameterize and optimize method for stratigraphically consistent assisted history matching of object-based geomodels: algorithm and field application: SPE Journal, **22**(04), 1-280. https://doi.org/10.2118/181269-PA

Aly, A. M., E. R. Hunt, D. A. Pursell, and W. D. McCain, 1997, Application of multi-well normalization of open hole logs in integrated reservoir studies: Presented at the SPE Western Regional Meeting.

Aminian, K., S. Ameri, A. Oyerokun, and B. Thomas, 2003, Prediction of flow units and permeability using artificial neural networks: Presented at the SPE Western Regional/AAPG Pacific Section Joint Meeting.

Arjovsky, M., S. Chintala, and L. Bottou, 2017, Wasserstein generative adversarial networks: ICML'17 Proceedings of the 34th International conference on machine learning, **70**, 214-223.

Asher, M. J., B. F. Croke, A. J. Jakeman, and L. J. Peeters, 2015, A review of surrogate models and their application to groundwater modeling: Water Resources Research, **51**(8), 5957-5973. https://doi.org/10.1002/2015WR016967

Babak, O., J. G. Manchuk, and C. V. Deutscz, 2013, Accounting for non-exclusivity in sequential indicator simulation of categorical variables: Computers and Geosciences, **51**, 118-128.

Barabási, A. L., and H. E. Stanley, 1995, Fractal concepts in surface growth: New York, Cambridge University Press, 29.

Bennis, M., and C. Torres-Verdín, 2019, Estimation of dynamic formation properties from multiple well logs using machine learning and unsupervised rock classification: Presented at the SPWLA 60th Annual Logging Symposium, Society of Petrophysicists and Well Log Analysts.

Berg, R.R., 1970, Method for determining permeability from reservoir rock properties: Gulf Coast Association of Geological Societies Transactions, **20**, 303-335.

Bertoncello, A., T. Sun, H. Li, G. Mariethoz, and J. Caers, 2013, Conditioning surface-based geological models to well and thickness data: Mathematical Geosciences, **45**, 873-893. doi:10.1007/s11004-013-9455-4

Bestagini, P., V. Lipari, and S. Tubaro, 2017, A machine learning approach to facies classification using well logs: Technical Program, Society of Exploration Geophysicists, Expanded Abstracts, 2137-2142.

Bhattacharya, S., and S. Mishra, 2018, Applications of machine learning for facies and fracture prediction using Bayesian network theory and random forest: case studies from the Appalachian Basin, USA: Journal of Petroleum Science and Engineering, **170**, 1005-1017.

Boisvert, J. B., and M. J. Pyrcz, 2014, Conditioning 3D object based models to a large number of wells: a channel example: Mathematics of Planet Earth, 575-579. https://doi.org/10.1007/978-3-642-32408-6_126

Boisvert, J. B., M. J. Pyrcz, and C. V. Deutsch, 2006, Choosing training models and checking realizations with multiple point statistics: Centre for Computational Geostatistics, **8**.

Boisvert, J. B., M. J. Pyrcz, and C. V. Deutsch, 2007, Multiple-point statistics for training model selection: Natural Resources Research, **16**(4), 313-321. https://doi.org/10.1007/s11053-008-9058-9

Boisvert, J. B., M. J. Pyrcz, and C. V. Deutsch, 2010, Multiple point metrics to assess categorical variable models: Natural resources research, **19**(3), 165-175. https://doi.org/10.1007/s11053-010-9120-2

Borg, I., and P. J. Groenen, 2005, Modern multidimensional scaling: theory and applications: Springer Science and Business Media.

Bornemann, E., and J. H. Doveton, 1981, Log normalization by trend surface analysis: The log analyst, **22**(04).

Brazell, S., A. Bayeh, M. Ashby, and D. Burton, 2019, A machine-learning-based approach to assistive well-log correlation: Petrophysics, **60**, 469-479.

Caers, J., 2003, History matching under training-image-based geological model constraints: SPE journal, **8**(03), 218-226. https://doi.org/10.2118/74716-PA

Carman, P.C., 1956, Flow of gases through porous media: New York, Academic Press, 62.

Chan, S., and A. H. Elsheikh, 2017, Parametrization and generation of geological models with generative adversarial networks: https://arxiv.org/pdf/1708.01810.pdf (accessed January 10, 2020).

Chang, J., J. Li, Y. Kang, W. Lv, T. Xu, Z. Li, W. X. Zheng, H. Han, and H. Liu, 2021, Unsupervised domain adaptation using maximum mean discrepancy optimization for lithology identification: Geophysics, 86, ID19-ID30.

Collobert, R., and J. Weston, 2008, A unified architecture for natural language processing: deep neural networks with multitask learning: 25th International Conference on Machine Learning, International Conference on Machine Learning, proceedings, 160–167. doi:10.1145/1390156.1390177.

Cressie, N., 1985, Fitting variogram models by weighted least squares: Journal of the International Association for Mathematical Geology, **17**(5), 563-586. https://doi.org/10.1007/BF01032109

Cressie, N., and Hawkins, D. M., 1980, Robust estimation of the variogram: Journal of the International Association for Mathematical Geology, **12**(2), 115-125.

Cullis, S., L. Colombera, M. Patacci, and W. D. McCaffrey, 2018, Hierarchical classifications of the sedimentary architecture of deep-marine depositional systems: Earth-Science Reviews, **179**, 38-71.

Deng, T., C. Xu, D. Jobe, and R. Xu, 2019, A comparative study of three supervised machine-learning algorithms for classifying carbonate vuggy facies in the Kansas arbuckle formation: Petrophysics, **60** (06), 838-853.

Deng, T., C. Xu, X. Lang, and J. Doveton, 2021, Diagenetic Facies Classification in the Arbuckle Formation Using Deep Neural Networks. Mathematical Geosciences, **53**(7), 1491-1512.

Deng, T., J., Ambía, and C. Torres-Verdín, 2020, Bayesian method for rapid multi-well interpretation of well logs and core data in unconventional formations: Presented at the SPWLA 61st Annual Logging Symposium.

Deptuck, M. E., D. J. Piper, B. Savoye, and A. Gervais, 2008, Dimensions and architecture of late Pleistocene submarine lobes off the northern margin of East Corsica: Sedimentology, **55**, 869-898.

Deutsch, C. V., and A.G. Journel, 1992, Geostatistical software library and user's guide: New York: Oxford University Press.

Deutsch, C. V., and L. Wang, 1996, Hierarchical object-based stochastic modeling of fluvial reservoirs: Mathematical Geology, **28**(7), 857-880. https://doi.org/10.1007/BF02066005

Deveugle, P. E. K., M. D. Jackson, G. J. Hampson, J. Steart, M. D. Clough, T. Ehighebolo, M. E. Farrell, C. S. Calvert, and J. K. Miller, 2014, A Comparative study of reservoir modeling techniques and their impact on predicted performance of fluvial-dominated deltaic reservoirs: AAPG Bulletin, **98**, 729–763, doi:10.1306/08281313035.

Doetsch, J. A., I. Coscia, S. Greenhalgh, N. Linde, A. Green, and T. Günther, 2010, The borehole-fluid effect in electrical resistivity imaging: Geophysics, **75**(4), 107-114.

Dupont, E., T. Zhang, P. Tilke, L. Liang, and W. Bailey, 2018, Generating realistic geology conditioned on physical measurements with generative adversarial networks: https://arxiv.org/pdf/1802.03065.pdf (accessed January 10, 2020).

Ester, M., H. P. Kriegel, J. Sander, and X. Xu, 1996, Density-based spatial clustering of applications with noise: Proceedings of the Second International Conference on Knowledge Discovery and Data Mining, 226–231, doi:10.1.1.121.9220.

Ferguson, R. I., 1976, Disturbed periodic model for river meanders: Earth Surface Processes, **1**(4), 337-347. https://doi.org/10.1002/esp.3290010403

Ferguson, R. I., M. Church, and H. Weatherly, 2001, Fluvial aggradation in Vedder River: Testing a one-dimensional sedimentation model: Water Resources Research, **37**(12), 3331-3347. https://doi.org/10.1029/2001WR000225

Finol, J. and D. Jing, 2002, Permeability prediction in shaly formations: The Fuzzy Modeling Approach: Geophysics, **67** (3), 817-829. http://dx.doi.org/ 10.1190/1.1484526

Fuglede, B. and Topsoe, F., 2004, Jensen-Shannon divergence and Hilbert space embedding: Proceedings of the International Symposium on Information Theory, 30. doi:10.1109/ISIT.2004.1365067. ISBN 978-0-7803-8280-0. S2CID 7891037.

Gaillot, P., J. Lewandowski, and R. Nursaidova, 2019, Uncertainty analysis in formation evaluation: rationale, methods and examples: Presented at SPWLA 60th Annual Logging Symposium, Society of Petrophysicists and Well Log Analysts.

Gashler, M., 2008, Decision tree ensemble: small heterogeneous is better than large homogeneous: Seventh International Conference on Machine Learning and Applications, International Conference on Machine Learning, proceedings, 900–905. doi:10.1109/ICMLA.2008.154

Girshick, R., 2015, Fast R-CNN: Proceedings of the IEEE international conference on computer vision, 1440-1448.

Goodfellow, I., J, Pouget-Abadie, M, Mirza, B, Xu, D. Warde-Farley, S. Ozair, A. Courville, and Y. Bengio, 2014, Generative Adversarial Nets: Advances in neural information processing systems, **27**, 2672-2680.

Greder, H. N., P. Y. Diver, S. Danquigny, and F. M. Pellerin, 1996, Determination of permeability distribution at log scale in vuggy carbonates: Presented at the SPWLA 37th Annual Logging Symposium, Society of Petrophysicists and Well Log Analysts.

Gringarten, E. and C. V. Deutsch, 2001, Teacher's aide variogram interpretation and modeling: Mathematical Geology, **33**(4), 507-534. https://doi.org/10.1023/A:1011093014141

Groenenberg, R. M., D. M. Hodgson, A. Prelat, S. M. Luthi, and S. S. Flint, 2010, Flow–deposit interaction in submarine lobes: Insights from outcrop observations and realizations of a process-based numerical model: Journal of Sedimentary Research, **80**, 252-267. doi:10.2110/jsr.2010.028.

Grove, G. P. and Minerbo, G. N., 1991, An adaptive borehole correction scheme for array induction tools: Presented at the SPWLA 32nd Annual Logging Symposium.

Guin, A., R. Ramanathan, R. W. Ritzi, D. F. Dominic, I. A. Lunt, T. D. Scheibe, and V. L. Freedman, 2010, Simulating the heterogeneity in braided channel belt deposits: Examples of results and comparison to natural deposits: Water Resources Research, **46**(4). https://doi.org/10.1029/2009WR008112

Haldorsen, H. H., and L. W. Lake, 1984, A new approach to shale management in field-scale models: Society of Petroleum Engineers Journal, **24**(04), 447-457. https://doi.org/10.2118/10976-PA

Hansen, L. K. and P. Salamon, 1990, Neural network ensembles: IEEE Transactions on Pattern Analysis and Machine Intelligence, **12**(10), 993-1001. https://doi.org/10.1109/34.58871

Hassanpour, M. M., M. J. Pyrcz, and C. V. Deutsch, 2013, Improved geostatistical models of inclined heterolithic strata for McMurray Formation, Alberta, Canada: AAPG bulletin, **97**(7), 1209-1224.

He, K., G. Gkioxari, P. Dollár, and R. Girshick, 2017, Mask R-CNN: Proceedings of the IEEE international conference on computer vision, 2961-2969.

Holden, L., R. Hauge, Ø. Skare, and A. Skorstad, 1998, Modeling of fluvial reservoirs with object models: Mathematical Geology, **30**(5), 473-496. https://doi.org/10.1023/A:1021769526425

Hu, L. Y., 2000, Gradual deformation and iterative calibration of Gaussian-related stochastic models: Mathematical Geology, **32**(1), 87-108. https://doi.org/10.1023/A:1007506918588

Hu, L. Y. and T. Chugunova, 2008, Multiple-point geostatistics for modeling subsurface heterogeneity: A comprehensive review: Water Resources Research, **44**(11). https://doi.org/10.1029/2008WR006993

Hu, L. Y. and S. Jenni, 2005, History matching of object-based stochastic reservoir models: SPE Journal, **10**(03), 312-323. https://doi.org/10.2118/81503-PA

Isola, P., J. Y. Zhu, T. Zhou, and A. A. Efros, 2017, Image-to-image translation with conditional adversarial networks: Proceedings of the IEEE conference on computer vision and pattern recognition, 1125-1134.

Isola, P., J. Y. Zhu, T. Zhou, and A. A. Efros, 2017, Image-to-image translation with conditional adversarial networks: IEEE conference on computer vision and pattern recognition, 1125-1134. https://doi.org/10.1109/CVPR.2017.632

Jachmann, R., J. Yang, and Y. Wang, 2020, Motion artifact free data delivery in real time from a low gradient NMR tool: Presented at the SPWLA 61st Annual Logging Symposium.

Jin, Z. L., Y. Liu, and L. J. Durlofsky, 2019, Deep-learning-based reduced-order modeling for subsurface flow simulation: arXiv preprint arXiv:1906.03729.

Jo, H., and M. J. Pyrcz, 2019, Robust rule-based aggradational lobe reservoir models: Natural Resources Research, **29**, 1193–1213, doi:10.1007/s11053-019-09482-9.

Jo, H., J. E, Santos, and M. J. Pyrcz, 2020, Conditioning well data to rule-based lobe model by machine learning with a generative adversarial network: Energy Exploration and Exploitation, **38**(6), 2558-2578.

Jo, H., S. Santos, and M. J. Pyrcz, 2019, Conditioning stratigraphic, rule-based models with generative adversarial networks: a deepwater lobe example, 2019: Presented at the AAPG Annual Convention and Exhibition, San Antonio, Texas, 2019, doi:10.1306/42402Jo2019.

Jo, H., W. Pan, J. E. Santos, H. Jung, and M. J. Pyrcz, 2021, Machine learning assisted history matching for a deepwater lobe system: Journal of Petroleum Science and Engineering, **207**, 109086.

Kaplan, R., M. J. Pyrcz, and S. Strebelle, 2017, Deepwater reservoir connectivity reproduction from MPS and process-mimicking geostatistical methods: Geostatistics, Valencia, 601-611.

Kingma, D. P., and J. Ba, 2014, Adam: a method for stochastic optimization: arXiv preprint arXiv:1412.6980.

Kolla, V., H. W. Posamentier, and L. J. Wood, 2007, Deep-water and fluvial sinuous channels—Characteristics, similarities and dissimilarities, and modes of formation: Marine and Petroleum Geology, **24**(6-9), 388-405. https://doi.org/10.1016/j.marpetgeo.2007.01.007

Krumbein, W.C. and G.D. Monk, 1943, Permeability as a function of size parameters of unconsolidated sand: Trans., AIME **151** (1), 151. http://dx.doi.org/ 10.2118/943153-G

Kullback, S., and R. A. Leibler, 1951, On information and sufficiency: Annals of Mathematical Statistics, **22** (1), 79–86. doi:10.1214/aoms/1177729694.

Laloy, E., R. Herault, D. Jacques, and N. Linde, 2018, Training-image based geostatistical inversion using a spatial generative adversarial neural network, Water Resources Research, **54**(1), 381-406. https://doi.org/10.1002/2017WR022148

Laloy, E., R. Herault, J. Lee, D. Jacques, and N. Linde, 2017, Inversion using a new low-dimensional representation of complex binary geological media based on a deep neural network: Advances in Water Resources, **110**, 387–405. https://doi.org/10.1016/j.advwatres.2017.09. 029

Laloy, E., N. Linde, D. Jacques, and J. A. Vrugt, 2015, Probabilistic inference of multi-Gaussian fields from indirect hydrological data using circulant embedding and dimensionality reduction: Water Resources Research, **51**(6), 4224-4243. https://doi.org/10.1002/2014WR016395

Lang, X., M. Sengupta, C. Xu, T. Deng, and D. Grana, 2019, Log-facies classification using expectation-maximization: SEG Technical Program Expanded Abstracts 2019, 3161-3165.

LeCun, Y., L. Bottou, Y.Bengio, and P. Haffner, 1998, Gradient-based learning applied to document recognition: Proceedings of the IEEE, **86**(11), 2278-2324. https://doi.org/10.1109/5.726791

Leverett, M., 1941, Capillary behavior in porous solids: Transactions of the AIME, **142**(01), 152-169. https://doi.org/10.2118/941152-G

Li, X., G. Mariethoz, D. T. Lu, and N. Linde, 2016, Patch-based iterative conditional geostatistical simulation using graph cuts, Water Resources Research, **52**(8), 6297–6320. https://doi.org/10.1002/2015WR018378

Liang, L., T. Le, T. Zimmermann, S. Zeroug, and D. Heliot, 2019, A machine learning framework for automating well log depth matching: Presented at the SPWLA 60th Annual Logging Symposium, Society of Petrophysicists and Well Log Analysts.

Lie, K., 2019, An introduction to reservoir simulation using MATLAB/GNU Octave: user guide for the MATLAB reservoir simulation toolbox (MRST): Cambridge, Cambridge University Press, doi:10.1017/9781108591416.

Liu, F., K. Ting, and Z. Zhou, 2008, Isolation forest: Presented at the Eighth IEEE International Conference on Data Mining.

Liu, J., A. Eghbali, and C. Torres-Verdín, 2019, Resolution enhancement of sonic logs supported by ultrasonic data: Presented at the SPWLA 60th Annual Logging Symposium.

Maalouf, E., C. Torres-Verdín, and J. Liu, 2020, Application of Backus average to simulate acoustic logs in thinly bedded formations Backus average to model acoustic logs: Geophysics, **85**(3), 93-104.

Male, F., and I. J. Duncan, 2020, Lessons for machine learning from the analysis of porosity-permeability transforms for carbonate reservoirs: Journal of Petroleum Science and Engineering, **187**, 106825. https://doi.org/10.1016/j.petrol.2019.106825

Mallan, R. K., J. Thorne, P. Rice, E. Toumelin, J. B. Clavaud, and B. Bilodeau, 2018, Petrophysical uncertainty analysis using spatial bootstrapping: Presented at the

SPWLA 59th Annual Logging Symposium, Society of Petrophysicists and Well Log Analysts.

Manning, C. D., and H. Schutze, 1999, Foundations of statistical natural language processing: MIT Press.

Mariethoz, G. and Caers, J., 2014, Multiple-point geostatistics: stochastic modeling with training models: John Wiley and Sons.

Mariethoz, G., P. Renard, and J. Straubhaar, 2010, The direct sampling method to perform multiple-point geostatistical simulations, Water Resources Research, **46**(11). https://doi.org/10.1029/2008WR007621

Medellin, D., A. Eghbali, Y. Wang, and C. Torres-Verdín, 2019, Pore-size-dependent fluid substitution method for improved estimation of NMR porosity, permeability, and relaxation times: Presented at the SPWLA 60th Annual Logging Symposium.

Michael, H. A., H. Li, A. Boucher, T. Sun, J. Caers, S. M. Gorelick, 2010, Combining geologic-process models and geostatistics for conditional simulation of 3-D subsurface heterogeneity: Water Resources Research, **46**, 1–20. doi:10.1029/2009WR008414.

Mirza, M. and S. Osindero, 2014, Conditional generative adversarial nets: arXiv:1411.1784.

Mo, S., Y. Zhu, N. Zabaras, X. Shi, and J. Wu, 2019, Deep convolutional encoder-decoder networks for uncertainty quantification of dynamic multiphase flow in heterogeneous media: Water Resources Research, **55**(1), 703-728. https://doi.org/10.1029/2018WR023528

Mohaghegh, S., R. Arefi, I. Bilgesu, S. Ameri, and D. Rose, 1995, Design and development of an artificial neural network for estimation of formation permeability: SPE Computer Applications, **7**(06), 151-154.

Mohaghegh, S., B. Balan, and S. Ameri, 1997, Permeability determination from well log data: SPE Formation Evaluation, **12**(03), 170-174. https://doi.org/10.2118/30978-PA

Mutti, E., W.R. Normark, 1987, Comparing examples of modern and ancient turbidite systems: problems and concepts: Marine Clastic Sedimentology, 1-38.

Mutti, E., W.R. Normark, 1991, An integrated approach to the study of turbidite systems: Frontiers in Sedimentary Geology, 75-106.

Myerson, R. B. (1978). Refinements of the Nash equilibrium concept. International journal of game theory, 7(2), 73-80. https://doi.org/10.1007/BF01753236

Nguyen, A., J. Yosinski, and J. Clune, 2015, Deep neural networks are easily fooled: High confidence predictions for unrecognizable images: Proceedings of the IEEE conference on computer vision and pattern recognition, 427-436.

Nicolaysen, R. and T. Svendsen, 1991, Estimating the permeability for the Troll field using statistical methods querying a fieldwide database: Trans., Society of Professional Well Log Analysts.

Odena, A., V. Dumoulin, and C. Olah, 2016, Deconvolution and checkerboard artifacts: https://distill.pub/2016/deconv-checkerboard (accessed January 10, 2020).

Oliver, D. S., A. C. Reynolds, and N. Liu, 2008, Inverse theory for petroleum reservoir characterization and history matching: Cambridge University Press.

Oliver, M. A. and R. Webster, 1990, Kriging: a method of interpolation for geographical information systems: International Journal of Geographical Information System, **4**(3), 313-332.

Onesti, L. J. and T. K. Miller, 1974, Patterns of variation in a fluvial system: Water Resources Research, **10**(6), 1178-1186. https://doi.org/10.1029/WR010i006p01178

Øren, P. E., and S. Bakke, 2002, Process based reconstruction of sandstones and prediction of transport properties: Transport in porous media, **46**(2-3), 311-343. https://doi.org/10.1023/A:1015031122338

O'Shea, K. and R. Nash, 2015, An introduction to convolutional neural networks: arXiv preprint arXiv:1511.08458 (accessed January 10, 2020).

Otchere, D. A., T. O. A. Ganat, R. Gholami, and M. Lawal, 2021, A novel custom ensemble learning model for an improved reservoir permeability and water saturation prediction: Journal of Natural Gas Science and Engineering, **91**, 103962.

P.C. Carman, 1956, Flow of gases through porous media: Butterworths, London.

Pan, W., C. Torres-Verdín, and M. J. Pyrcz, 2020, Stochastic pix2pix: a new machine learning method for geophysical and well conditioning of rule-based channel reservoir models: Natural Resources Research, **30**, 1319–1345, doi: 10.1007/s11053-020-09778-1.

Pan, W., C. Torres-Verdin, M. J. Pyrcz, 2020, New machine learning method for integrated subsurface modeling: Presented at the American Geophysical Union 2020 Fall Meeting, online, 1-17 Dec.

Pérez-Cruz, F., 2008, Kullback-Leibler divergence estimation of continuous distributions: 2008 IEEE International Symposium on Information Theory, Institute of Electrical and Electronics Engineers, Proceedings, 1666-1670.

Pickering, K.T., J. D. Clark, R. D. A. Smith, R. N. Hiscott, F. Ricci Lucchi, N. H. Kenyon, 1995, Architectural element analysis of turbidite systems, and selected topical problems for sand-prone deep-water systems: Atlas of Deep Water Environments: Springer, Dordrecht, 1–10. https://doi.org/10.1007/978-94-011-1234-5_1

Pittman, E.D., 1992, Relationship of porosity and permeability to various parameters derived from mercury injection—capillary pressure curves for sandstone: American Association of Petroleum Geologists Bull, **76** (2), 191-198.

Potdar, K., T. S. Pardawala, and C. D. Pai, 2017, A comparative study of categorical variable encoding techniques for neural network classifiers: International Journal of Computer Applications, **175**(4), 7-9. https://doi.org/10.5120/ijca2017915495

Prasad, M., C. Olsen, and I. Fabricius, 2004, Rock physics and statistical well log analyses in carbonates: Presented at Annual Meeting, Society of Exploration Geophysicists.

Prélat, A., D. M. Hodgson, and S. S. Flint, 2009, Evolution, architecture and hierarchy of distributary deep-water deposits: a high-resolution outcrop investigation from the Permian Karoo Basin, South Africa: Sedimentology, v. 56, p. 2132-2154.

Pyrcz M.J., T. McHargue, J. Clark, M. Sullivan, S. Strebelle, 2012, Event-based geostatistical modeling: description and applications: Quantitative Geology and Geostatistics, 17, doi:10.1007/978-94-007-4153-9_3.

Pyrcz, M. J., and C. V. Deutsch, 2005, Conditioning event-based fluvial models: Quantitative Geology and Geostatistics, **14**, 135-144. https://doi.org/10.1007/978-1-4020-3610-1_14

Pyrcz, M. J., and C. V., Deutsch, 2014, Geostatistical reservoir modeling: Oxford university press, 30-350.

Pyrcz, M. J., J. B. Boisvert, and C. V. Deutsch, 2008, A library of training models for fluvial and deepwater reservoirs and associated code: Computers and Geosciences, **34**(5), 542-560. https://doi.org/10.1016/j.cageo.2007.05.015

Pyrcz, M. J., T. McHargue, J. Clark, M. Sullivan, and S. Strebelle, 2012, Event-based geostatistical modeling: description and applications: Quantitative Geology and Geostatistics, **17**, 27-38. https://doi.org/10.1007/978-94-007-4153-9_3

Pyrcz, M. J., O. Catuneanu, and C. V. Deutsch, 2005, Stochastic surface-based modeling of turbidite lobes: AAPG bulletin, **89**, 177-191, doi:10.1306/09220403112.

Pyrcz, M. J., R. I. Sech, J. A. Covault, T. Sun, B. R. Willis, Z, O. Sylvester, 2014, Process-mimicking modeling considerations: Closing the gap II: advances in applied geomodelling for hydrocarbon reservoirs, 1-16.

Pyrcz, M. J., R. P. Sech, J. A. Covault, B. J. Willis, Z. Sylvester, and T. Sun, 2015, Stratigraphic rule-based reservoir modeling: Bulletin of Canadian Petroleum Geology, **63**(4), 287-303. https://doi.org/10.2113/gscpgbull.63.4.287

Pyrcz, M.J., 2004, Integration of geologic information into geostatistical models: Ph.D. Dissertation, University of Alberta, Edmonton, Canada.

Quartero, E. M., D. Bechtel, A. L. Leier, and L. R. Bentley, 2014, Gamma-ray normalization of shallow well-log data with applications to the Paleocene Paskapoo Formation, Alberta: Canadian Journal of Earth Sciences, **51**(5), 452-465.

Ramanathan, R., A. Guin, R. W. Ritzi, D. F. Dominic, V. L. Freedman, T. D. Scheibe, and I. A. Lunt, 2010, Simulating the heterogeneity in braided channel belt deposits: a geometric-based methodology and code: Water Resources Research, **46**(4). https://doi.org/10.1029/2009WR008111

Ronneberger, O., P. Fischer, and T. Brox, 2015, U-net: convolutional networks for biomedical image segmentation: International conference on medical image computing and computer-assisted intervention, 234-241. doi: 10.1007/978-3-319-24574-4_28.

Santos, J.E., Y. Yin, H. Jo, W. Pan, Q. Kang, H. S. Viswanathan, M. Prodanović, M. J. Pyrcz, N. Lubbers, 2021, Computationally efficient multiscale neural networks applied to fluid flow in complex 3D porous media: Transport in Porous Media, **140**, 241–272. https://doi.org/10.1007/s11242-021-01617-y

Sasaki, H., Y. K. Noh, and M. Sugiyama, 2015, Direct density-derivative estimation and its application in KL-divergence approximation: International Conference on Artificial Intelligence and Statistics, Machine Learning Research, Proceedings, 809-818.

Shao, W., S. Chen, M. Eid, and G. Hursan, 2019, Carbonate log interpretation models based on machine learning techniques: Presented at the 60th Annual Logging Symposium, Society of Petrophysicists and Well Log Analysts.

Shashank, S., and M. P. Mahapatra, 2018, Boosting rock facies prediction: weighted ensemble of machine learning classifiers: Presented at the Abu Dhabi International Petroleum Exhibition and Conference, SPE. https://doi.org/10.2118/192930-MS

Shier, D. E., 2004, Well log normalization: methods and guidelines, Petrophysics, **45**(03), 268-280.

Shook, G. M., and K. M. Mitchell, 2009, A robust measure of heterogeneity for ranking earth models: the F PHI curve and dynamic Lorenz coefficient: Presented at the Society of Petroleum Engineers Annual Technical Conference and Exhibition, New Orleans, Louisiana, October 2009, doi:10.2118/124625-MS.

Sidahmed, M., A. Roy, and A. Sayed, 2017, Streamline rock facies classification with deep learning cognitive process: presented at the SPE Annual Technical Conference and Exhibition. doi:10.2118/187436-MS

Specht, D. F., 1991, A general regression neural network: IEEE transactions on neural networks, **2**(6), 568-576. https://doi.org /10.1109/72.97934

Straub, K. M., C. Paola, D. Mohrig, M. A. Wolinsky, and T. George, 2009, Compensational stacking of channelized sedimentary deposits: Journal of Sedimentary Research, **79**, 673-688.

Strebelle, S. B., and A. G. Journel, 2001, Reservoir modeling using multiple-point statistics: Presented at the SPE Annual Technical Conference and Exhibition, 30 September-3 October, New Orleans, Louisiana. https://doi.org/10.2118/71324-MS

Strebelle, S. Conditional simulation of complex geological structures using multiple-point statistics: Mathematical Geology, **34**(1):1–21, 2002.

Sullivan, M. D., J. L. Foreman, D. C. Jennette, D. Stern, G. N. Jensen, and F. J. Goulding, 2004, An integrated approach to characterization and modeling of deep-water reservoirs, Diana field, western Gulf of Mexico, in Integration of outcrop and modern analogs in reservoir modeling: AAPG Memoir 80, 215–234.

Sullivan, M., G. Jensen, F. Goulding, D. Jennette, L. Foreman, and D. Stern, 2000, Architectural analysis of deep-water outcrops: implications for exploration and development of the Diana sub-basin, western Gulf of Mexico: Deep-water reservoirs of the world: Gulf Coast Section SEPM Foundation 20th Annual Research Conference, 1010-1032. doi: 10.5724/gcs.00.15.1010.

Sun, T., P. Meakin, T. Jøssang, and K. Schwarz, 1996, A simulation model for meandering rivers: Water resources research, **32**(9), 2937-2954. https://doi.org/10.1029/96WR00998

Swanson, B.F., 1981, A simple correlation between permeabilities and mercury capillary pressures, Journal of Petroleum Technology, **33**(12), 2498-2504. http://dx.doi.org/10.2118/8234-PA

Swanson, D. C., 1993, The importance of fluvial processes and related reservoir deposits, Journal of Petroleum Technology, 45(04), 368-377. https://doi.org/10.2118/23722-PA

Thomas, R. G., D. G. Smith, J. M. Wood, J. Visser, E. A. Calverley-Range, and E. H. Koster, 1987, Inclined heterolithic stratification-terminology, description, interpretation and significance: Sedimentary geology, **53**(1-2), 123-179. https://doi.org/10.1016/S0037-0738(87)80006-4

Timur, A., 1968, An investigation of permeability, porosity, and residual water saturation relationships for sandstone reservoirs: The Log Analyst, **9**(4), 8.

Tzeng, E., J. Hoffman, K. Saenko, and T. Darrell, 2017, Adversarial discriminative domain adaptation: IEEE Conference on Computer Vision and Pattern Recognition, Institute of Electrical and Electronics Engineers, Proceedings, 7167-7176.

Van Baaren, J.P., 1979, Quick-look permeability estimates using sidewall samples and porosity logs: Presented at the 6th Annual European Logging Symposium, Society of Professional Well Log Analysts.

Vitoria, P., J. Sintes, and C. Ballester, 2018, Semantic image inpainting through improved wasserstein generative adversarial networks: https://arxiv.org/pdf/1812.01071.pdf (accessed in July 2020).

Wang, F. P., F. J. Lucia, and C. Kerans, 1998, Integrated reservoir characterization study of a carbonate ramp reservoir: Seminole San Andres Unit, Gaines County, Texas: SPE Reservoir Evaluation and Engineering, 105–113. doi:10.2118/36515-PA

Wang, Q., S. R. Kulkarni, and S. Verdú, 2009, Divergence estimation for multidimensional densities via k-nearest-neighbor distances: IEEE Transactions on Information Theory, **55**(5), 2392-2405.

Wang, Y. C., M. J. Pyrcz, O. Catuneanu, and J. B. Boisvert, 2018, Conditioning 3D object-based models to dense well data: Computers and Geosciences, **115**, 1-11. doi:10.1016/j.cageo.2018.02.006

Wang, Y., D. Medellin, and C. Torres-Verdín, 2019, Estimating capillary pressure from NMR measurements using a pore-size-dependent fluid substitution method: Presented at the SPWLA 60th Annual Logging Symposium.

Wang, Y., K. M. Straub, and E. A. Hajek, 2011, Scale-dependent compensational stacking: an estimate of autogenic time scales in channelized sedimentary deposits: Geology, **39**, 811–814, doi:10.1130/G32068.1.

Warrick, A. W. and D. E. Myers, 1987, Optimization of sampling locations for variogram calculations: Water Resources Research, **23**(3), 496-500. https://doi.org/10.1029/WR023i003p00496

Williams, C. K. I., 1998, Prediction with Gaussian processes: from linear regression to linear prediction and beyond: Learning in Graphical Models, **89**, 599–621. https://doi.org/10.1007/978-94-011-5014-9_23

Wood, D. A., 2020, Predicting porosity, permeability and water saturation applying an optimized nearest-neighbour, machine-learning and data-mining network of well-log data: Journal of Petroleum Science and Engineering, **184**, 106587.

Xu, R., T. Deng, J. Jiang, D. Jobe, and C. Xu, 2020, Integration of NMR and conventional logs for vuggy facies classification in the arbuckle formation: a machine learning approach: SPE Reservoir Evaluation and Engineering, **23**(03), 917-929.

Xu, W., T.T. Tran, R.M. Srivastava, 1992, Integrating seismic data in reservoir modeling: the collocated Cokriging alternative: Presented at the SPE Annual Technical Conference and Exhibition. http://dx.doi.org/10.2118/24742-MS

Yosinski, J., J. Clune, Y. Bengio, and H. Lipson, 2014, How transferable are features in deep neural networks?: Proceedings of the 27th International Conference on Neural Information Processing Systems, **2**, 3320-3328.

Yu, Y., C. Xu, S. Misra, W. Li, M. Ashby, W. Pan, T. Deng, H. Jo, J. E. Santos, 2021, Synthetic sonic log generation with machine learning: a contest summary from five methods: Petrophysics, **62**, 393–406. doi: https://doi.org/10.30632/PJV62N4-2021a4

Zhang, J. J., S. H. Wu, T. E. Fan, H. J. Fan, L. Jiang, C. Chen, Q. Wu, and P. Lin, 2016, Research on the architecture of submarine-fan lobes in the Niger Delta Basin, offshore West Africa: Journal of Palaeogeography, **5**, 185-204. doi:10.1016/j.jop.2016.05.005.

Zhang, T. F., P. Tilke, E. Dupont, L. C. Zhu, L. Liang, and W. Bailey, 2019, Generating geologically realistic 3D reservoir facies models using deep learning of sedimentary architecture with generative adversarial networks: Petroleum Science, **16**, 541-549. https://doi.org/10.1007/s12182-019-0328-4

Zhang, T., Z. Yang, and D. Li, 2022, Stochastic simulation of deltas based on a concurrent multi-stage VAE-GAN model: Journal of Hydrology, 127493.

Zhang, X., M. J. Pyrcz, and C. V. Deutsch, 2009, Stochastic surface modeling of deepwater depositional systems for improved reservoir models: Journal of Petroleum Science and Engineering, **68**, 118-134. doi:10.1016/j.petrol.2009.06.019.

Zhang, Y., M. Person, C. Paola, C. W. Gable, X. H. Wen, and J. M. Davis, 2005, Geostatistical analysis of an experimental stratigraphy: Water resources research, **41**(11). https://doi.org/10.1029/2004WR003756

Zhang, Z. Y., M. Y. Li, and J. Yu, 2018, On the convergence and mode collapse of GAN: SIGGRAPH Asia 2018 Technical Briefs, 1-4, doi:10.1145/3283254.3283282.

Zhong, Z., T. R. Carr, X. Wu, and G. Wang, 2019, Application of a convolutional neural network in permeability prediction: a case study in the Jacksonburg-Stringtown oil field, West Virginia, USA: Geophysics, **84**(6), 363-373. https://doi.org/10.1190/geo2018-0588.1

Zhu, J. Y., T. Park, P. Isola, and A. A. Efros, 2017, Unpaired image-to-image translation using cycle-consistent adversarial networks: Proceedings of the 2017 IEEE international conference on computer vision, 2242-2251. https://doi.org/10.1109/ICCV.2017.244

Zhu, L., H. Li, Z. Yang, C. Li, and Y. Ao, 2018, Intelligent logging lithological interpretation with convolution neural networks: Petrophysics, **59**, 799–810. doi: https://doi.org/10.30632/PJV59N6-2018a5.

Vita

Wen Pan received his B.Sc. (2016) in petroleum engineering from the China University of Petroleum (Beijing). After that, he joined the Bureau of Economic Geology, Formation Evaluation Research Consortium, and Digital Reservoir Characterization Technology Consortium in the Hildebrand Department of Petroleum and Geosystems Engineering at the University of Texas at Austin. He worked as a graduate student assistant and the instructor of the Inventor's Program during his study at the University. He was an architect of the UT 2022 Hackathon. In the summer of 2020, he worked as an intern at British Petroleum, Houston, Texas, developing machine-learning and optimization algorithms for uncertainty quantification of production data. In the summer of 2021, he returned to BP as an intern to develop machine learning and geological modeling algorithms. Wen is a guest editor of the AI/ML Special Issue for "*Petrophysics* Journal", and a member of the AGU, SEG, SPE, and SPWLA.

Permanent e-mail address: wenpan@utexas.edu

This dissertation was typed by Wen Pan.